UNIVERSITY OF CALIFORNIA SAN DIEGO

An Engineering Approach to Biological Materials and Chemistry: Leveraging Nature's Ability to Optimize Toughness, Mass Transfer, and Specific Binding Chemistry

A dissertation submitted in partial satisfaction of the

requirements for the degree of Doctor of Philosophy

in

Materials Science and Engineering

by

Sean Nolan Garner

Committee in charge:

Professor Andrea Tao, Chair
Professor Shengqiang Cai
Professor Vlado Lubarda
Professor Mike Tolley

2022

The Dissertation of Sean Nolan Garner is approved and is acceptable in quality and form for publication on microfilm and electronically.

University of California San Diego

2022

DEDICATION

This thesis is dedicated to my first Ph.D. advisor, Professor Joanna McKittrick, who was one of the first women to join the engineering faculty at UC San Diego. She taught me I can continue to hold my appreciation and child-like awe of the natural world while taking seriously the rigor of respectable engineering. Further, thank you to my second advisor and committee chair, Professor Andrea Tao, for taking a chance on bringing me into her research group and mentoring me in the rich discipline of Nanoengineering.

To my beloved friend, Kenneth Yun (1994-2017). Thank you for teaching me the significance of light-heartedness and comradery. Your contagious passion and giving nature have left me inspired to do good, whether big or small. You shocked everyone around you with your ability to bring people together.

Lastly, thank you to my family and my partner, Raquelle, who has been with me every step of the way.

EPIGRAPH

The task is, not so much to see what no one has seen yet; but to think what nobody has thought yet, about what everybody sees.

Erwin Schrödinger

TABLE OF CONTENTS

LIST OF FIGURES

LIST OF TABLES

ACKNOWLEDGEMENTS

I would also like to thank all my mentors who guided me as well as all the undergraduate researchers that graced me with an opportunity to pass on what I have received. Thank you to all my fellow co-authors, collaborators, and lab-mates for their thoughtful discussions and unfettered support.

Chapter 1, in part, is published as "The role of collagen in the dermal armor of the Boxfish" Journal of Materials Research and Technology" Journal of Materials Research and Technology, 9(6), 13825–13841, November 2020. This work was coauthored by Garner, S. N.; Naleway, Steven E.; Hosseini, Maryam S.; Acevedo, Claire; Gludovatz, Bernd; Schaible, Eric; Jung, Jae-Young; Ritchie, Robert O.; Zavattieri, Pablo; & McKittrick, Joanna. The dissertation author is the first and corresponding author of this work. This work is supported by a Multi-University Research Initiative through the Air Force Office of Scientific Research (AFOSR-FA9550-15-1-0009). We thank the A.Z. Weber group for providing their tensile stage, which was supported by DOE EERE Fuel-Cell Performance and Durability Consortium (FC-PAD). This work was performed in part at the San Diego Nanotechnology Infrastructure (SDNI) of UCSD, a member of the National Nanotechnology Coordinated Infrastructure, which is supported by the National Science Foundation (Grant ECCS-1542148). This work used the Extreme Science and Engineering Discovery Environment (XSEDE), which is supported by National Science Foundation grant number ACI-1548562 [49]. We also acknowledge the use of beamline 7.3.3 at the Advanced Light Source, which is supported by the U.S. Department of Energy, Office of Science, Office of Basic Energy Sciences, Division of Materials Sciences and

Engineering, under contract no. DE-AC02-05CH11231 to the Lawrence Berkeley National Laboratory. Special thanks are due to Prof. Phil Hastings of the Scripps Institute of Oceanography, UC San Diego, for providing the boxfish specimens and Dr. James Tyler of the Smithsonian for helpful discussions.

Chapter 2, in part, is published as "Mechanical Optimization of Diatomite Monoliths from Freeze Casting for High-Throughput Applications" ACS Applied Bio Materials 2020 3 (7), 4444-4453. This work was coauthored by Li, Zhixiong; Lee, Doheon; Graeve, Olivia A.; Deheyn, Dimitri D.; and McKittrick, Joanna M. The dissertation author is the first author of this work. This work was performed in part at the San Diego Nanotechnology Infrastructure (SDNI) of UCSD, a member of the National Nanotechnology Coordinated Infrastructure, which is supported by the National Science Foundation (Grant ECCS-1542148). We acknowledge Jessica Moreton, Dr. Brian Pimentel and Prof. Seth M. Cohen (Dept. of Chemistry & Biochemistry, UCSD) for assistance with gas sorption experiments. We acknowledge Dr. Ekaterina Novitskaya and Prof. Olivia Graeve (Dept. of Mechanical Aerospace Engineering, UCSD) for assistance with X-ray diffractions experiments.

Chapter 3, in part is currently being prepared for submission for publications of the material. This work was coauthored by Garner, Sean N.; Bradshaw, Nathan; and Tao, Andrea. The dissertation author was the primary investigator and author of this material. The work presented in this chapter was supported by a National Science Foundation Grant (RAPID CBET-2032196).

VITA

2022 Ph.D. Materials Science and Engineering

University of California San Diego

Dissertation: "An Engineering Approach to Biological Materials and Chemistry: Leveraging Nature's Ability to Optimize Toughness, Mass Transfer, and Specific Binding Chemistry"

Advisor: Professor Andrea Tao

2018 M.S. Materials Science and Engineering

University of California San Diego

Dissertation: "Collagen's Role in the Dermal Armor of the Boxfish"

Advisor: Professor Joanna McKittrick

2016 B.S. Chemical Engineering

University of California, Santa Barbara

PUBLICATIONS

Sean N. Garner, Nathan Bradshaw, Andrea R. Tao, "Surface-enhanced Raman Spectroscopy Platform for High-Sensitivity Point-of-Care Biosensing" In-preparation.

Frances Y. Su, Fereshteh A. Sabet, Katherine Tang, Sean Garner, Siyuan Pang, Michael T. Tolley, Iwona Jasiuk, Joanna McKittrick, "Scale and size effects on the mechanical properties of bioinspired 3D printed two-phase composites" Journal of Materials Research and Technology, 9(6), 14944–14960, November 2020.

Sean N. Garner, Steven E. Naleway, Maryam S. Hosseini, Claire Acevedo, Bernd Gludovatz, Eric Schaible, Jae-Young Jung, Robert O. Ritchie, Pablo Zavattieri, Joanna McKittrick, "The role of collagen in the dermal armor of the Boxfish" Journal of Materials Research and Technology, 9(6), 13825–13841, November 2020.

Sean N. Garner, Zhixiong Li, Doheon Lee, Olivia A. Graeve, Dimitri D. Deheyn, and Joanna M. McKittrick, “Mechanical Optimization of Diatomite Monoliths from Freeze Casting for High-Throughput Applications” ACS Applied Bio Materials, 3(7), 4444-4453, June 2020.

ABSTRACT OF THE DISSERTATION

An Engineering Approach to Biological Materials and Chemistry: Leveraging Nature's Ability to Optimize Toughness, Mass Transfer, and Specific Binding Chemistry

by

Sean Nolan Garner

Doctor of Philosophy in Materials Science and Engineering

University of California San Diego, 2022

Professor Andrea Tao, Chair

The complex structure of the collagen in the dermal armor of the boxfish provides a rich source of bioinspired engineering for fiber-reinforced composite materials. Advanced imaging and material characterization of this complex collagen structure revealed a Bouligand-type structure common in impact resistance biological materials. These Bouligand-type structures were shown to have several additional characteristics that included helical interfibrillar gaps, unidirectional collagen reinforcement of specific loading axes, and were uniquely organized into higher order structures referred to as a

nested-box structure. *In situ* mechanical tests coupled with finite element simulations were performed to further demonstrate structure and failure mechanics of the dermal armor.

The silica cell wall of a diatom, abundant microalgae 1 – 100 μm in size, contains highly ordered hierarchical porosity and is widely available through its fossilized form, diatomite. The research uses diatomite to fabricate a monolith with unidirectional lamellar walls (~15 μm) via freeze casting that allows for efficient mass transport of fluids (i.e., low pressure-drop) while maintaining sufficient mechanical properties. In this study, control over the monoliths was explored by varying the mass ratio of diatomite and sodium carbonate and the solids ratio in the initial slurry before freeze casting.

A point-of-care biosensor based on a surface-enhance Raman spectroscopy (SERS) sandwich assay platform is developed using silver nanocubes (AgNCs) on a gold capture substrate. The biosensor leverages the specific binding chemistry of the streptavidin-biotin system, one of the strongest non-covalent interactions in nature, by functionalizing both the AgNCs and the capture substrate with a heterobifunctional ligand, biotin-polyethylene glycol-thiol. The model analyte, streptavidin, is then used to bind the exposed biotin head groups on the AgNCs and the capture substrate to form the sandwich assay. The SERS of a Raman reporter, 2-naphthalenethiol, which is also bound to the AgNC surface is then obtained for a highly sensitive quantification of the streptavidin present. Further functionalization and surface treatment of the capture substrates were performed to reduce the non-specific binding of AgNC.

CHAPTER 1: The Role of Collagen in the Dermal Armor of the Boxfish

1.1 Abstract

This research aims to further the understanding of the structure and mechanical properties of the dermal armor of the boxfish (*Lactoria cornuta*). Structural differences between collagen regions underlying the hexagonal scutes were observed with confocal microscopy and microcomputed tomography (μ-CT). μ-CT revealed a tapering of the mineral plate from the center of the scute to the interface between scutes, suggesting the structure allows for more flexibility at the interface. High-resolution μ-CT revealed, for the first time, a 3D image of the dermal armor's complex collagen structure. Helical interfibrillar gaps in the collagen base were found that are similar to the Bouligand-type structure of the lobster, Homarus americanus, thereby suggesting that the collagen in the boxfish is also of a Bouligand-type structure. *In situ* scanning electron microscopy tests were performed in shear and tension between two connected scutes and suggest that the interfacial collagen is structurally designed to preferentially absorb energy during deformation to protect the internal collagen. Similarly, *in situ* small-angle x-ray scattering was performed in shear and tension and further corroborated the complex collagen structure. Lastly, these experimental results are coupled with finite element simulations that characterize the interfacial collagen and corroborate the non-linear deformation response seen during in situ testing. Overall, these findings further the understanding of the structure and mechanics of the dermal armor of the boxfish which may help provide a

basis to synthesize bioinspired composites for impact-resistant materials, specifically with bioinspired Bouligand-type structures to create novel fiber-reinforced composites.

1.2 Introduction

Overlapping scale patterns are common amongst marine and freshwater fish species. These overlapping structures have developed as full coverage of the fish's body which simultaneously provide protection from predators while maintaining flexibility for swimming and other body motions [1]. There are, however, a small number of fish species that employ more rigid armor. Many of the species in the *Ostraciidae* family use rigid armor in their defense [2, 3]. Recent work by Yang *et al*. [4] provided insight into the armor of the boxfish, but also provided for a number of additional questions into this alternative armor style.

The scales and scutes of fish species are capable of providing effective protection from predation through a layered, composite structure [5-8]. This structure tends to consist of a highly mineralized surface plate (often made of bony or enamel-like materials) and a less-mineralized, collagen base [6, 7, 9-12]. The less mineralized collagen base is most often formed in a twisted plywood, or Bouligand structure [13-15], which consists of planes of aligned collagen fibrils stacked on top of each other with each layer slightly rotated [1]. The Bouligand structure also appears in several other impact resistant biological materials including the exoskeletons of arthropods and the dactyl club of the mantis shrimp [16-18]. The reason for its universality within biopolymer composites in the natural world is due to its optimization of several parameters including (1) creating quasi-isotropic fiber reinforced materials to avoid weakness in a given axis; (2) allowing for the fibers to reorient

along the loading axis to provide more resistance [13]; (3) improving energy dissipation and stress relaxation by influencing cracks to follow the helical fiber orientations thereby maximizing crack surface area per unit volume [19].

When attacked by a predator, the layered structure of fish scales and scutes provides both protection from the sharp piercing action of a tooth (through the hardened surface plate) and the powerful compressive and crushing force of the jaws (through the tough collagen base) [7]. Beyond the functions of an individual scale, the overlapping structure of scales can provide protection. Vernerey and Barthelat [20-22] analytically studied these structures in fish and showed that, by balancing the scale length and spacing between scales with the total body length, many species are capable of large overall body flexibility, while minimizing the rotation of individual scales, thus resisting puncture when attacked. While this overall body flexibility is important for motion, it also plays a significant role in defense. In addition, the flexibility of the body itself provides some energy absorbance as the piercing tooth of a predator will cause the body to deform and the overlapping scales to lock together before stress is directly applied to the scale [22]. Due to this success, overlapping scale structures are found in a variety of animals including most teleost fish [7, 9, 11, 12, 23], pangolin [24], and chiton [25], and has led to a number of bioinspired armor designs [8, 26]. Given these benefits of overlapping structures, a fish species that employs rigid armor would be unwise to forsake all flexibility.

In this study, the dermal armor of the longhorn cowfish (*Lactoria cornuta*, Figure 1.1), a type of boxfish, is structurally and mechanically characterized. Figure 1.2 shows a diagram of the features of the boxfish's armor, similar to those previously reported [3, 4].

The rigid armor consists of non-overlapping, primarily hexagonal scutes (Figure 1.2a) [4]. Similar to many other fish scales, the scutes themselves are made of hydroxyapatite mineral and type I collagen and are structured as a highly mineralized surface plate (1:0.33 mineral-to-collagen ratio) sitting on a collagen base (1:12 mineral-to-collagen ratio) [4]. The mineralized surface plate features raised ridges that extend from the center of the scute to the edges. The interface between scutes is made of interlocking mineralized triangular sutures, which are unlike many similar structures in nature as they are devoid of any bridging Sharpey's fibers or compliant phase (Figure 1.2b) [4]. Geometric analysis of triangular sutured structures by Li *et al*. [27-29] demonstrated that the teeth angles of the boxfish's sutures ($2\theta = 50.6°$) were considerably different from what would be expected to maximize the strength of the interface ($2\theta = 23.6°$). This contrast between the theoretical optimized angle for strength in sutured interfaces and actual angle of suture teeth in the boxfish is likely due to the former being calculated while including a compliant phase junction between sutured interfaces that is not found in the boxfish sutures. Additionally, these results may also suggest that boxfish suture's geometry are not solely optimized for strength [4].

Figure 1.1: Lateral view of the boxfish (Lactoria Cornuta), commonly referred to as the longhorn cowfish. Image taken from [33].

The collagen base itself, imaged with scanning electron microscopy (SEM), revealed two important features illustrated in Figure 1.2c [4]. First, the interior of the scute consists of periodic patterns in the collagen structure, similar to the Bouligand structure found in the scales of most fish species, but different in terms of the orientation of the periodic axis with respect to the thickness of the dermis. Typically, Bouligand structures found in nature align the periodic axis with the primary loading directions, as seen in the collagen phase underneath the mineral plates in teleost fish scales [13, 18]. However, as shown in Figure 1.2c the direction of the periodic axis changes from being orthogonal to the mineral plate near the distal and lateral regions (where 'distal' refers to the anatomically outer regions of boxfish dermis where the mineral plate is, and 'lateral' refers to the peripheral edges of the hexagonal scute) to being parallel, like its teleost counterparts, near the proximal and central regions. This unique structure has prompted us to further

investigate the local structure of the collagen fibrils in this underlying network and determine if it is a ladder-like structure, as previously claimed [4].

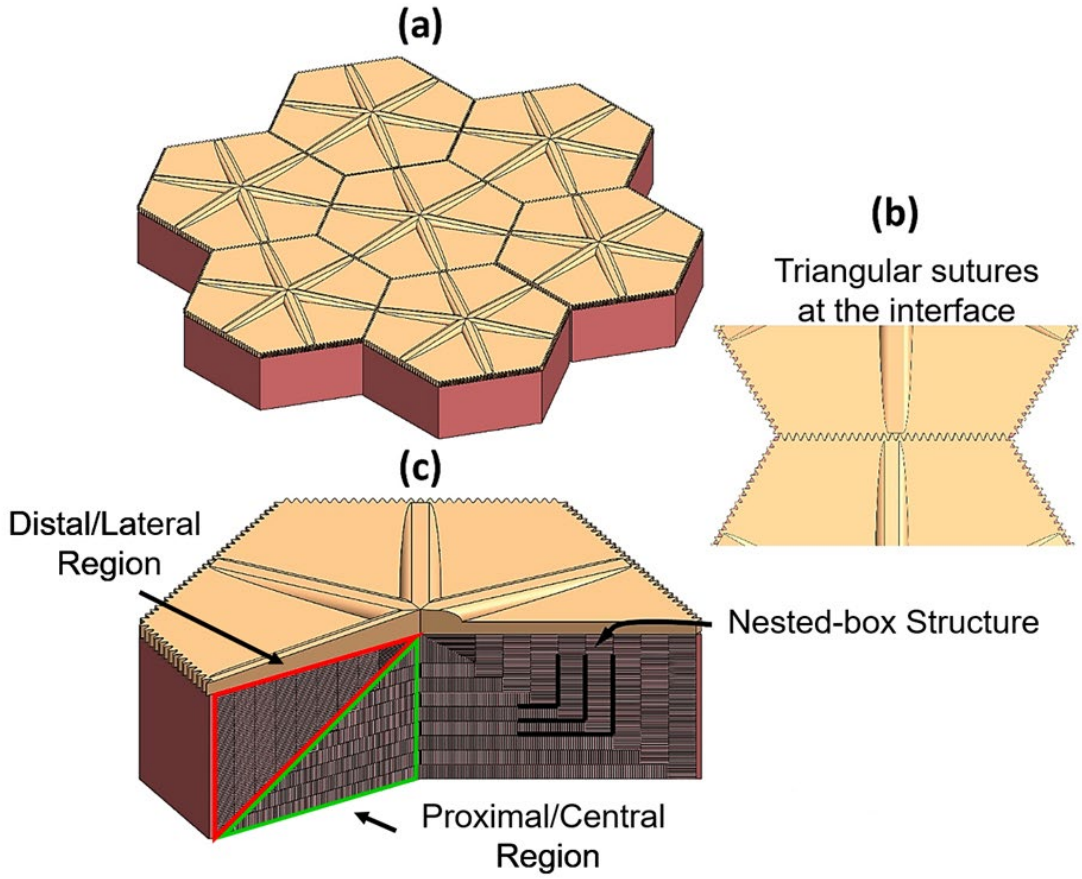

Figure 1.2: Boxfish armor structure, as similarly reported [4]. **(a)** The armor consists of predominately hexagonal scutes that feature raised ridges extending from their center to edge; **(b)** The scutes do not overlap, but instead have interlocking suture structures

In this work we build upon previous knowledge and present new evidence of the mechanisms that allow the boxfish to maintain flexibility and protection despite its rigid armor. The rigid dermal armor enables the boxfish to survive in its natural environment despite the lack of speed and ability to undulate like most other fish. Understanding the boxfish's dermal armor and specifically the complex collagen network beneath the mineralized scutes, will aid in future bioinspired engineering pursuits. For example, novel

materials have been synthesized inspired by the Bouligand structure that range from additive manufacturing resilient ceramic-polymer composites, self-assembling cellulose nanocrystals into a Bouligand structure to create a tough and strong photonic film, and also bio-templating a Bouligand structure from crustacean shells to create a hydrogel that changes color based on pH [30-32]. Essentially, utilizing this naturally ubiquitous structure in bioinspired engineering endeavors is creating novel fibrous composites with a combination of efficient mechanical performance and photonic properties. Therefore, further exploration and study of unique analogs of Bouligand-type structures found in nature can add to the repertoire for future bioinspired engineering.

1.3 Materials and Methods

Two boxfish samples were obtained from the Scripps Institution of Oceanography at the University of California, San Diego (*Lactoria cornuta,* catalog numbers SIO 14-20, SIO 95-125, SIO 95-141). A representative image [33] is shown in Figure 1.1. Samples were preserved in a 1:1 isopropanol and water solution to induce a semi-dehydrated state. The two fish selected measured ~50 mm in length and ~100 mm in length.

1.3.1 Structural Characterization

Scutes were cut from the mid-section of the boxfish samples using a scalpel such that each specimen consisted of two neighboring, connected, hexagonal scutes. Imaging was performed on 15 dehydrated specimens with the mineralized plates carefully polished to reveal the underlying collagen base. Polishing was carried out with 1700-grit SiC paper, using water as a lubricant, prior to sonicating in water to remove residuals. Scanning electron microscopy (SEM) was performed on 14 of these pairs of scutes. Another pair was

infiltrated with OsO_4, critically point dried, fixed in epoxy, and polished to a shine such that the collagen surfaces could be better observed. This pair of polished and stained scutes was used in both three-dimensional (3D) imaging with micro-computed tomography (μ-CT) and with confocal microscopy (Keyence VH-Z100UR).

Both the low- and high-resolution μ-CT was performed using a Zeiss Versa 510 microscope with a voxel size of 9 μm and 535 nm, respectively. The resulting μ-CT images (2,401 projections) were edited and stitched together using the Amira software (Thermo Fisher Scientific, Waltham, Massachusetts) to create a high-resolution 3D image.

1.3.2 *In situ* Mechanical Characterization

1.3.2.1 *In situ* Scanning Electron Microscopy

The scutes were mechanically analyzed using *in situ* tests within the SEM. Prior to testing, all samples were rehydrated in Hanks' balanced salt solution for 24 hours, then immediately tested, to ensure that all tests were performed in a hydrated state. To understand the rigid, non-overlapping interfaces of the boxfish's armor, the scute samples were tested in tension and shearing loading modes (see Figure 1.3a) with a focus on the interface between scutes. To ensure this, the samples were carefully sectioned with a scalpel from the boxfish to include exactly two scutes with a single, unaltered interface between them. In addition, samples were tested both in an intact form and with the surface mineralized plate removed. The surface plate was carefully polished off using same method mentioned in Section 2.1.

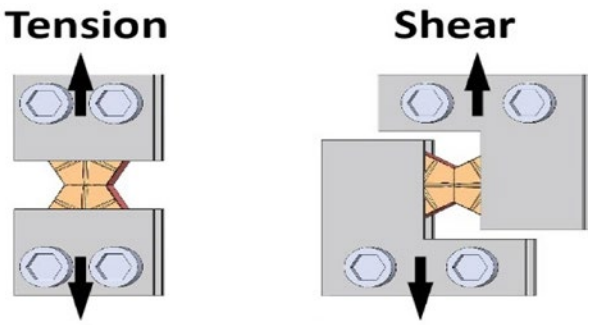

Figure 1.3: Schematic diagram of mechanical fixtures employed for in situ mechanical tests (with scanning electron microscopy and small-angle x-ray scattering) in both tensile and shearing modes.

In situ SEM testing was performed under step-loading at a displacement rate of 0.1 mm/min (slowest displacement rate available to best observe deformation mechanisms of collagen structures) using a Gatan Microtest 2kN bending stage (Gatan, Abington, UK) in a S4300SE/N variable pressure SEM (Hitachi America, Pleasanton, CA, USA) operated at a partial pressure of 35 Pa. Five samples were tested with the mineralized plate intact and seven were tested with the mineralized plate removed.

1.3.2.2 *In situ* Small-angle X-ray Scattering

Small-angle X-ray scattering (SAXS) patterns were collected during *in situ* uniaxial tensile testing at beamline 7.3.3 at the Advanced Light Source X-ray synchrotron at the Lawrence Berkeley National Laboratory [34]. As each scute was put under load, simultaneous measurements were made of the deformation of the tissue on the macro scale, as well as the deformation of the collagen fibrils within the tissue on the nanoscale.

Scutes were prepared for such SAXS analysis, as described above for *in situ* SEM testing. The scutes were clamped at their extremities into the jaws of TST-350 tensile stage (Linkam Scientific, Inc.) and subjected to a displacement rate of 5 μm/s. Five of the scutes

were measured in tension, and three in shear. During testing, each sample was exposed to x-rays of 10 keV energy for 1 s every 7.5 s, with the changing x-ray scattering patterns collected with a Pilatus3 2M detector (Dectris, Ltd.) at a distance of approximately 4 meters. The cumulative irradiation dose was kept underneath the limit of 30 kGy in order to minimize irradiation damage to the tissue which could affect its mechanical behavior [35]. Given these irradiation conditions, the displacement rate was chosen to be quick enough to prevent damaging irradiation of sample. Although hydration and drying of the sample in air was a concern, the power of the beam was considered too weak (on the order of a milliwatt) to cause significant heating. Therefore, hydration was not monitored.

Scattering of the x-rays, specifically with the *d*-period of the collagen fibrils, a 67 nm regular pattern of molecular gaps and overlaps, acted to create Bragg peaks on the detector, and as this molecular pattern was stretched by the applied loads, the strain in the fibrils could be measured from the resulting shifts in the Bragg peaks., *i.e.*, the *d*-period of the collagen fibrils was used an a nanoscale strain gauge. The SAXS data were analyzed with custom software written in LabVIEW, which subtracted out the background intensity with spline fits, located the azimuthal center of each Bragg peak with a Gaussian fit, and made a 5-degree radial integration around each azimuthal center. The *d*-period of the collagen fibrils was measured by fitting this radial integration with an exponentially modified Gaussian. The fibril strain was then derived from the changes in *d*-period, as compared to the *d*-period at zero load. The SAXS patterns also contained broader dot-shaped peaks created by the interaction of the x-rays with the regular lateral packing of the collagen fibrils; these were analyzed using the same software.

The tissue strain was obtained by collecting visible light charge coupled device (CCD) images of the scutes in parallel with the x-ray scattering data. The CCD images were processed with digital image correlation methods to follow the changes in spacing of patterns on the outside surface of the scute.

Previous reports on the use of SAXS on the collagen structures in fish scales have shown a diffraction pattern with distinct concentric arcs, corresponding to the *d*-period of the collagen fibril and its harmonics [13]. Figure 1.4a shows a diagram of this, where the lateral packing distance between collagen fibrils is displayed in the enlarged dots (horizontally aligned dots) and *d*-period spacing within collagen fibrils orthogonal to the x-ray beam are displayed in the smaller arcs (vertically aligned arcs). These characteristic x-ray interactions with complex collagen systems have also been well-documented in research performed in the past few decades with SAXS on human cornea collagen structures [36]. Figure 1.4b illustrates a simplified Bouligand structure (with only 0-45-90° oriented lamellae) where the diffraction patterns are expected from performing SAXS either transverse or parallel to the Bouligand (or helical) axis. It is important to note that Bouligand structures in biological materials typically have significantly smaller rotations between lamellae which give rise to overlapping arcs/dots which form a continuous circle for the diffraction pattern, as opposed to a few discrete arcs [11]. Furthermore, by comparing Figure 1.4a with Figure 1.4b, the diffraction patterns for a unidirectional system can be seen to have a similar pattern produced from the Bouligand structure transverse to its helical axis. This occurs because collagen fibrils are orthogonal (in red) to the incident x-rays (as in the unidirectional network); however, as the lamellae rotate to become parallel

with x-ray (in orange) the *d*-period of these layers becomes effectively hidden to the incident x-ray while the lateral packing of the fibrils remains. Therefore, the key difference between these two diffraction patterns is that the ratio of intensities between the *d*-period arcs and lateral packing dots will be less in the case of the Bouligand structure which allows for a nuanced strategy to tell the two structures apart.

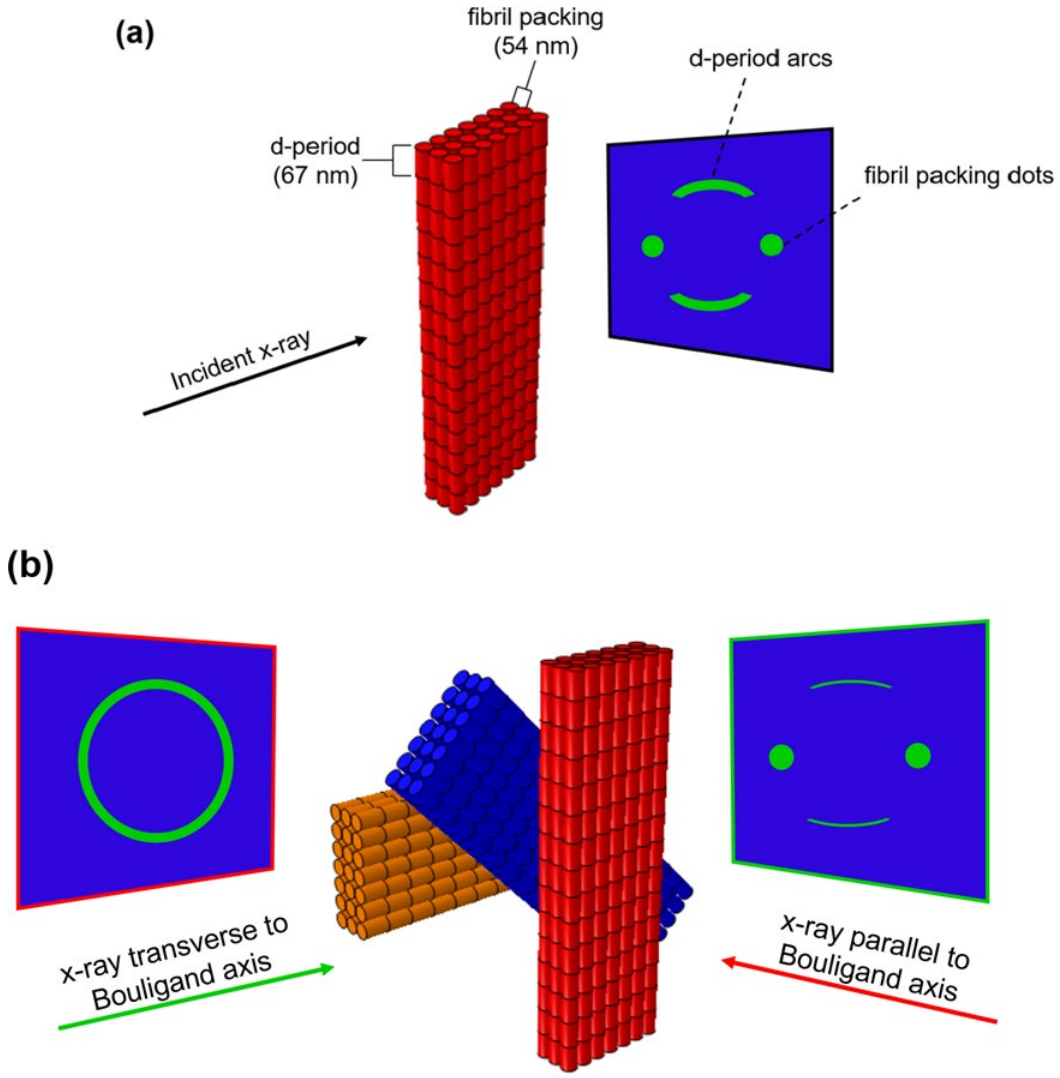

Figure 1.4: **(a)** Small-angle x-ray scattering diffraction pattern from analyzing a unidirectional network of packed collagen fibrils that are orthogonal to the incident x-rays. The periodicity of the characteristic *d*-period in collagen fibril as well as the packing of the fibrils are observed in the diffraction pattern which are represented by the arcs and dots, respectively. **(b)** Diffraction pattern from analyzing a rotating network of packed collagen fibrils (*i.e.*, Bouligand structure). When the incident x-rays are transverse to the axis of rotation (*i.e.*, Bouligand axis) a diffraction pattern that is nearly identical to the unidirectional network of fibrils, **(a)**, however, the ratio of the intensity of the *d*-period arcs and lateral packing dots should be less due to the *d*-period of the fibrils becoming effectively hidden to the incident x-rays when the fibrils are parallel with x-ray b(orange). Bouligand axis) a diffraction pattern that is nearly identical to the unidirectional network of fibrils, **(a)**, however, the ratio of the intensity of the *d*-period arcs and lateral packing dots should be less due to the *d*-period of the fibrils becoming effectively hidden to the incident x-rays when the fibrils are parallel with x-ray b (orange). The lateral packing of fibrils should be observed regardless of the angle of rotation of the lamellae. When the Bouligand structure is analyzed parallel to the Bouligand axis, a concentric ring is observed if the angle of rotation between lamellae is small enough due to overlap between *d*-period arcs and lateral packing dots that represent each lamella.

1.4 Results and Discussion

1.4.1 Confocal Microscopy

Confocal microscopy provided a relatively quick and easy approach to observe the underlying collagen structure within a boxfish scute to provide a basis for further advanced imaging. Figure 1.5a reveals a cross-section of the scute collagen network where it is clear that there is a periodic structure present that changes its axis of periodicity throughout the scute, giving rise to the nested-box structure previously observed [3]. Moreover, Figure 1.5a reveals that the pitch length (180° rotation of collagen planes) of the proximal/central of the nested-box decreases (~ 5 times smaller) compared to the distal/lateral regions.

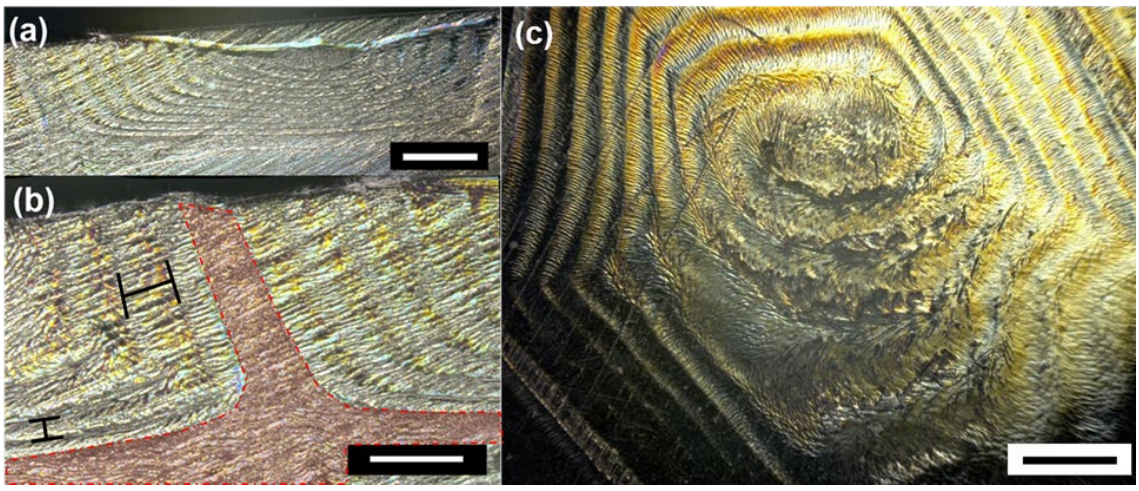

Figure 1.5: Confocal microscopy images of boxfish scute with top mineral plate removed. **(a)** Cross-section of whole scute revealing the nested-box structure (scale bar, 500 μm); **(b)** Zoom in on the cross-section of the interface between adjacent scute (highlighted in red). The lack of texture to the surface is indicative of a less structured region as compared to inside the scute. The pitch length (black brackets) in the distal/lateral regions (100 to 200 μm) is significantly larger than the proximal/central regions (~50 μm) (scale bar, 200 μm); **(c)** After careful removal of mineral plate, the periodic collagen structure can be seen. A portion of scute has been damaged through handling (scale bar, 500 μm).

Figure 1.5b provides a closer look at the interface between two scutes and reveals there seems to be a difference in contrast between the inner collagen (nested-box) and the

interfacial collagen. This difference suggests there is a structural difference between the two types of collagen that is further explored using μ-CT, SEM and subsequently SAXS. A top-down view of a scute with its mineral plate carefully polished off, in Figure 1.5c, reveals that the periodic structure aligns itself with the scutes' hexagonal edges. Artifacts of damage from polishing can also be seen.

1.4.2 Micro-Computed Tomography

High-resolution μ-CT was performed to determine the organization of collagen fibrils in the periodic regions. These 3D images revealed the helical interfibrillar gaps (seen as blue parallel lines in Figure 1.6b) that are similar to those in the twisted plywood, or Bouligand-type, structure of the exoskeleton of the lobster *Homarus americanus* and cuticle of the weevil *Curculio longinasus* [37-39]. This evidence corroborates research done by Besseau and Bouligand [3] to characterize the twisted plywood (Bouligand-type) structure in the collagen structure of the boxfish. However, this structure is contradictory to the most recent work by Yang *et al.* [4] that hypothesized the collagen structure in the boxfish scute follows a ladder-like structure rather than a Bouligand-type structure, *i.e.*, that the periodic structure seen on the top surface consists of rows of collagen planes separated and connected by orthogonal planes acting as the rungs of the 'ladder'. These claims, although proven here to be incorrect, still demonstrate that this structure consists of a unique type of Bouligand-type arrangement that can be confused for a different structure (ladder-like) when observing only the surface. Figure 1.6 reveals, using 3D imaging, the apparent rungs of the ladder-like structure are in-fact the tips of the helical interfibrillar gaps being exposed. The helical gaps are exposed on the top face when the

long axis of the gaps are parallel to the thickness of the dermis and on the front face when the width is orthogonal to the thickness. Although the Bouligand-type structure was revealed through the imaging of the helical interfibrillar gaps in the distal/lateral regions of the nested-box structure (Figure 1.6), these gaps did not appear in the proximal/central regions where the axis of periodicity changes to become parallel with the dermis. The absence of observable gaps and a decrease in pitch length previously suggested from confocal microscopy suggests this region maintains less ductility and more stiffness than the top/side regions.

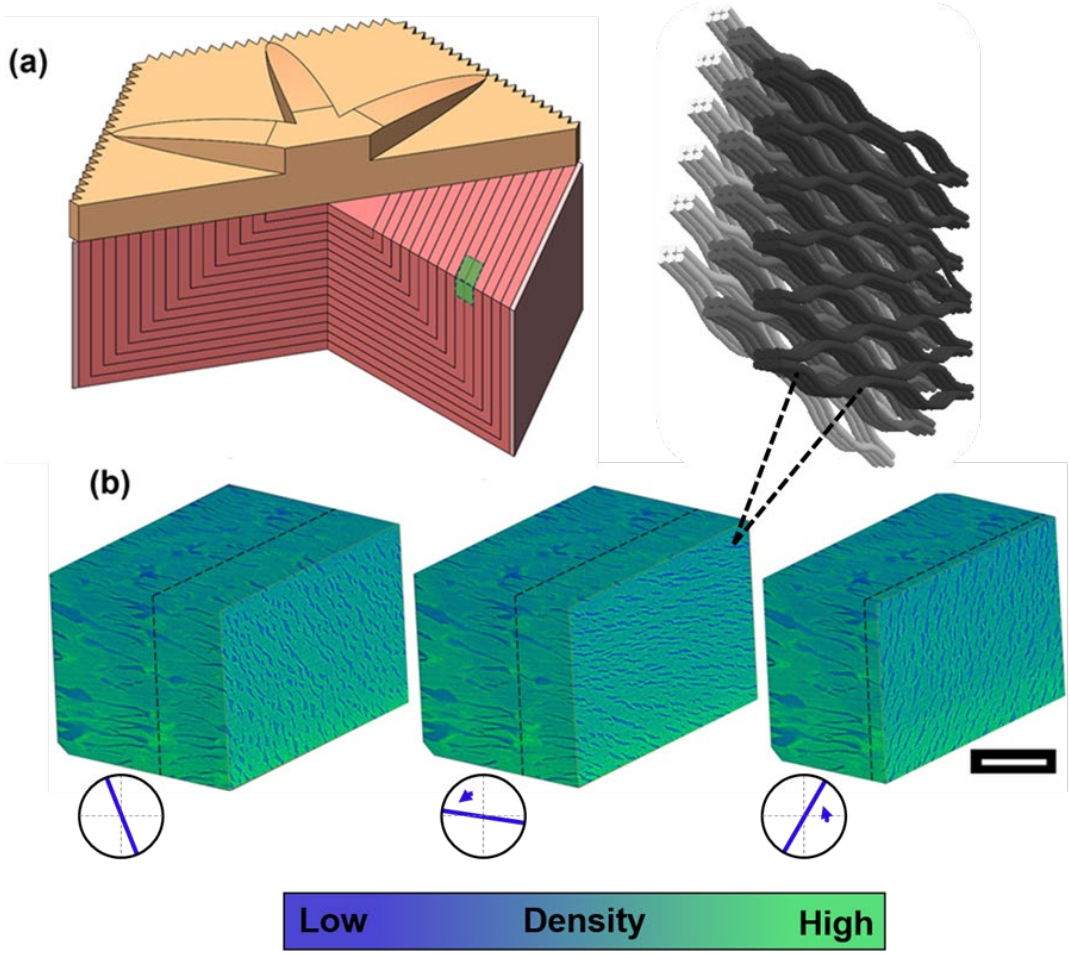

Figure 1.6: **(a)** Scute model with highlighted region representing approximate location of the micro-computed tomography (μ-CT) 3D images; **(b)** A series of the same3D μ-CT image is shown where a deeper cross section is taken with each image. The cross sections demonstrate continuous, helical interfibrillar gaps (porosity shown in blue) which are representative of a Bouligand-type structure. The aperture inset is representative of the direction the interfibrillar gaps have rotated to at this given cross-section. The thin, dashed black lines provide a reference between images.3D model of collagen fibrils represents the honeycomb-style Bouligand structure that these data reveal (scale bar, 100 μm).

The boxfish employs a complex and hierarchical network of collagen beneath its unique hexagonal scutes that we are now beginning to understand. The Bouligand structure, observed in many impact resistant natural materials manifests itself in varying materials (*i.e.*, collagen and chitin) and length scales (*e.g.*, the pitch length can vary from ~220 nm in *Cotinis mutabilis* exocuticle to 100 μm in the dactyl club of the mantis shrimp)

[17,18]. Moreover, the Bouligand structure found in the lobster exoskeleton possesses a unique type of honeycomb structure that is a variant of the Bouligand structure with interfibrillar gaps dispersed throughout the helical collagen fibrils that are proposed to act as microchannels for nutrient transport and also resist fiber pullout [37,38]. In this study, using μ-CT, it was observed that the distal/lateral regions of the collagen layer of the scute employs this honeycomb structure of helical interfibrillar gaps. Although this type of honeycomb structure has been observed before, the boxfish appears to uniquely utilize an abrupt shift in the helical axis giving rise to the previously described nested-box structure. Typically, for Bouligand structures found in natural materials, the helical axis aligns with the loading/impact axis (*e.g.*, fish scale's helical axis aligns with the thickness of the scale) [11]. Therefore, it is hypothesized that the unique nested-box structure evolved to resist bending forces that occur when the boxfish's dermal armor interlocks and recruits multiple scutes during a biting attack. In other words, the axis of compression during concave bending of the dermal armor would align with the helical axis of the Bouligand structure found in the distal/lateral region and would help explain the unique macro-organization that the boxfish employs in the collagen layer, although further investigation is needed to confirm such a hypothesis. Future research in designing bioinspired Bouligand structures to create novel impact resistant fiber reinforced composites may benefit from learning more about why the boxfish's Bouligand-type structure utilizes the higher-order nested-box structure.

1.4.3 *In situ* Scanning Electron Microscopy

1.4.3.1 Localized Failure

Samples were tested with an *in situ* micro-mechanical testing system to further investigate failure between neighboring scutes and investigate load-bearing capabilities of these structures. Scutes tested in tension (Figure 1.7a) showed failure occurring entirely at the interface. The mineralized sutures sustain no visible damage and, while some cracks form within the mineralized plates, the collagen base below can be seen to separate and tear (Figure 1.7b). When tested in a shearing mode (Figure 1.7c), more damage is visible to the mineralized plate, including the sutures that, in many cases, lock together and fracture. However, final failure still occurs predominantly in the collagen base (Figure 1.7d).

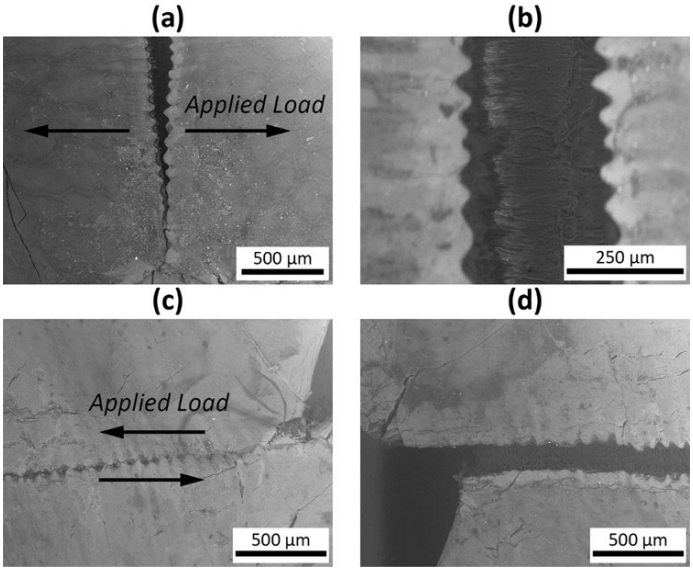

Figure 1.7: *In situ* SEM images with the mineralized plate under: **(a, b)**, tensile loading and **(c, d)**, shear loading. **(a)** In tension little damage to the mineralized plates is observed with the scutes splitting at the interface; **(b)** close observation of the interface shows no damage to the mineralized sutures, with the collagen base failing underneath; **(c)** In shear, the mineralized plate experiences more cracking at and near the sutures, however **(d)** failure occurs again predominantly in the underlying collagen base.

Given that the majority of failure occurred in the collagen base which was obscured by the presence of the mineralized plate, *in situ* SEM mechanical testing was performed with the mineralized plate carefully removed. Despite the somewhat weakened structure and the hence exacerbated deformation of the collagen, failure was predominantly located at the interface in both tensile (Figure 1.8a) and shearing (Figure 1.8b) loading modes. Consistent failure modes both with and without the presence of the mineralized plate suggest that the mineralized plate's primary purpose does not offer significant defense against either tension or shear between the scutes. This is generally consistent with the scales of other fish species, where the outer surface of an individual scale provides a rigid barrier against sharp penetration [7, 8], but the combined scale/scute structure provides toughness and ductility [22]. Additionally, the interlocking of the scute's sutured interfaces, unique to the boxfish, during shear modes allows for the force of a predator's attack to efficiently delocalize through the carapace thereby circumventing the issue of lacking enough strength to locally resist the attack. [40]

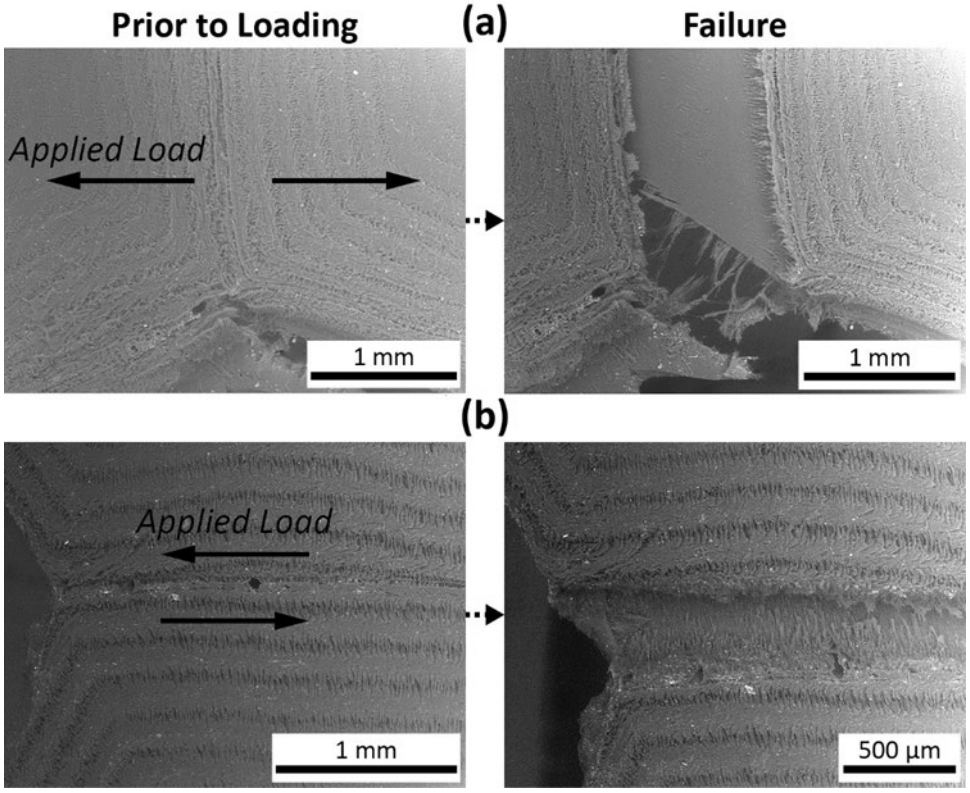

Figure 1.8: *In situ* SEM images with the mineralized plate removed, loaded in **(a)** tension and **(b)** shear. Regardless of the loading mode, failure occurs almost entirely at the interface.

1.4.3.2 Nonlinear Deformation Response

When observed in the SEM, the previously observed ladder-like structures of collagen within the scute interior can be seen (Figure 1.9a) [4]. However, during *in situ* SEM mechanical loading, it can be seen that these collagen planes deform in a much more complex way than would be expected from a ladder-like structure consisting of bidirectional/orthogonal collagen fibrils; instead, they form a somewhat double-twisted S-shape structure resulting from the applied shear-load (Figure 1.9b). This manner of behavior was observed throughout the interior of the scute's collagen base. It is proposed that this structure allows for the collagen planes to distort and realign with an applied stress, providing some measure of isotropy of at least some of its mechanical properties, thereby

increasing the deformation resistance of the scute interior, which is similar to previous conclusions reported for the deformation response of Bouligand structures found in nature [11,18,19].

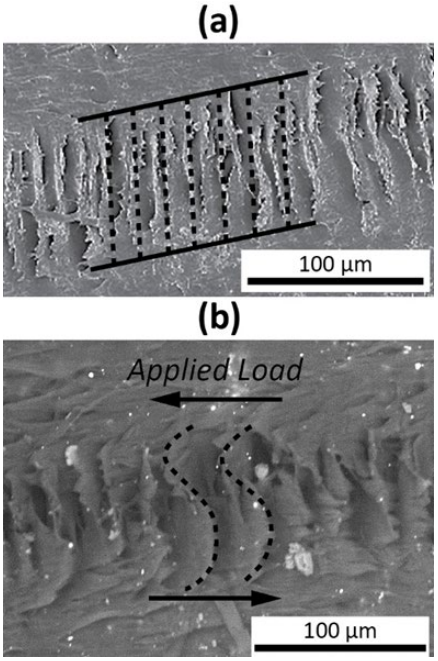

Figure 1.9: Scanning electron microscopy images of **(a)** The previously identified ladder-like structures [4] within the interior of the scute's collagen base consist of collagen planes (dashed lines) that bridge the gap between dense collagen bands (solid lines); **(b)** When a shearing load is applied to this structure, the collagen planes deform into a complex, sinusoidal S-shape, suggesting a different structure than a bidirectional ladder-like structure.

1.4.4 *In situ* Small-Angle X-ray Scattering

The SAXS data (Figures 10a, d) displayed rings superimposed with oriented arcs and broad dot-shaped peaks, which yielded various levels of information that needed to be carefully considered with other data, such as *a priori* knowledge of a Bouligand-type structure and the change in direction of the Bouligand structure throughout the higher-order nested-box structure of the boxfish scute. The dot-shaped peaks derive from the regular spacing of closely packed and closely aligned collagen fibrils; they are similar to patterns

reported previously for other natural systems, such as human cornea [36]. Measurements of the distance between neighboring collagen fibrils (roughly the collagen fibril diameter), made from these dots, gave a fibril diameter value of 53 ± 10 nm, which agrees closely with corresponding measurements of collagen fibril diameter in the SEM [4] of 55 ± 10 nm.

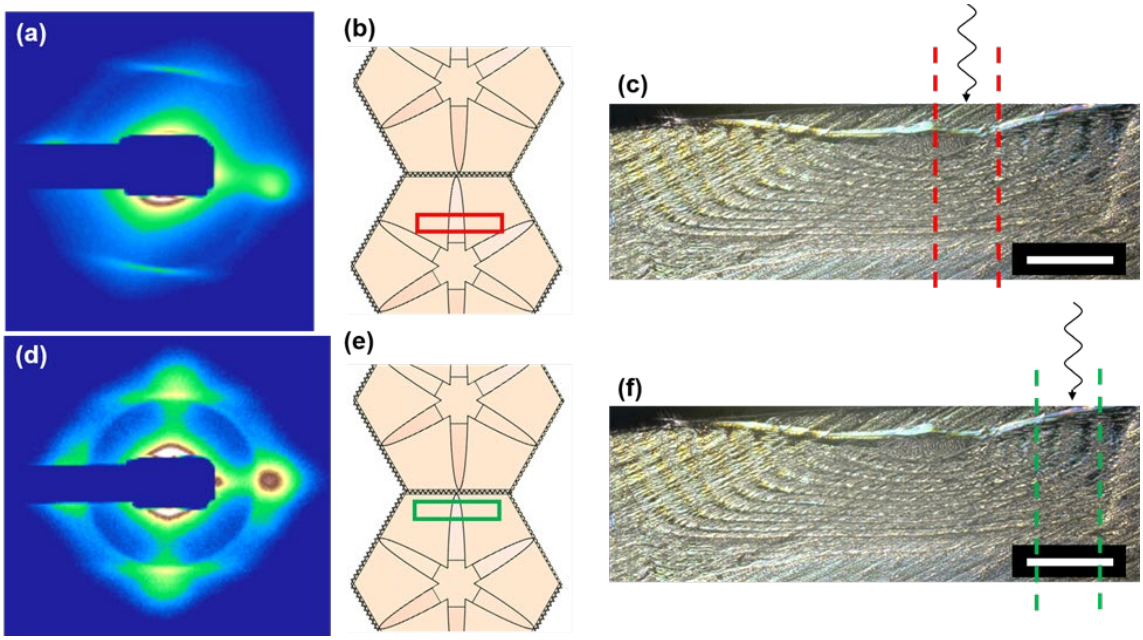

Figure 1.10: **(a, d)** Small-angle x-ray scattering diffraction (SAXS) patterns from boxfish scutes. **(b, e)** Representation of two neighbored boxfish scutes anchored vertically to apply a tensile load. Red and green rectangles represent the regions of interest (ROI); **(c, f)** Confocal microscopy cross-section view of nested-box collagen structure. Dotted lines represent the width of ROI to reveal which sections of the structure were analyzed with SAXS. (scale bar: 0.5 mm) **(a)** Displays a pair of vertical arcs and horizontal dots that represent the *d*-period of collagen and the lateral packing of collagen fibrils, respectively. **(d)** Displays two pairs of dots and arcs orthogonal to each other which is proposed to be representative of both the proximal/central region and distal/lateral regions.

Samples were imaged through the thickness of the scutes with different placements of the region of interest (ROI) that helped deduce what attributes were representative of which regions of the underlying nested-box structure (Figure 1.10). As shown in Figures 10a-c, when the ROI is closer to the center of one a scute, a pattern representative of the

proximal/central region of the nested-box is observed, where the Bouligand structure is expected to align with the incident x-rays. As shown in Figures 10d-f, the ROI closer to the interface between the two scutes garnered data that represents both the proximal/central region but also the distal/lateral region, which we hypothesize, from the μ-CT data, is where the Bouligand axis is transverse to the incident x-rays.

Figure 1.10a, which targeted the proximal/central region of the nested-box structure, most noticeably demonstrates a unidirectional fibril system from the bold horizontal dots and vertical arcs representative of the periodicities of the lateral packings of collagen fibrils and *d*-period spacing within the fibrils, respectively (Figure 1.10b). The direction of these fibrils is orthogonal to the edges of the hexagonal shape of the scute. Additionally, there appears to be a faint concentric ring that suggests the expected Bouligand-structure with its axis parallel to the thickness of the scute and the incident x-rays. Therefore, we corroborate previous results [3] that reveal a combination of both a unidirectional and Bouligand structure network in the proximal/central region.

Figure 1.10d, which encapsulates both regions of the nested-box structure, contains nearly identical information to Figure 1.10a but also appears to include an orthogonal direction of unidirectional fibrils. However, due to previous reports on the presence of a Bouligand structure [3] and the findings in this work with μ-CT, we hypothesize that these attributes are likely due to the SAXS beam interacting with the Bouligand structure transverse to its helical axis rather than due to additional unidirectional fibrils. It is worth noting that Besseau and Bouligand [3] also found unidirectional fibrils running transverse (aligned with the thickness of the scute) to the Bouligand structure in the distal/lateral

region. However, we do not expect these fibrils to contribute much to the resultant diffraction patterns as the fibrils are aligned with the incident x-rays and, therefore, their *d*-periods are effectively hidden.

Overall, we observed three main characteristics resulting from the SAXS patterns, utilizing previous research on the boxfish collagen structure, evidence from data acquired in this work, and the fundamental knowledge of the interaction of SAXS in collagen systems. These three main characteristics, shown in Figure 1.11 are:

- A Bouligand structure in the proximal/central region of nested-box structure.
- A unidirectional network of radial collagen fibrils that transversely intersect the Bouligand structure in the proximal/central region.
- A Bouligand structure in the outer/top region with its helical axis transverse to the thickness of the scute and aligned normal to the hexagonal edges of the scute.

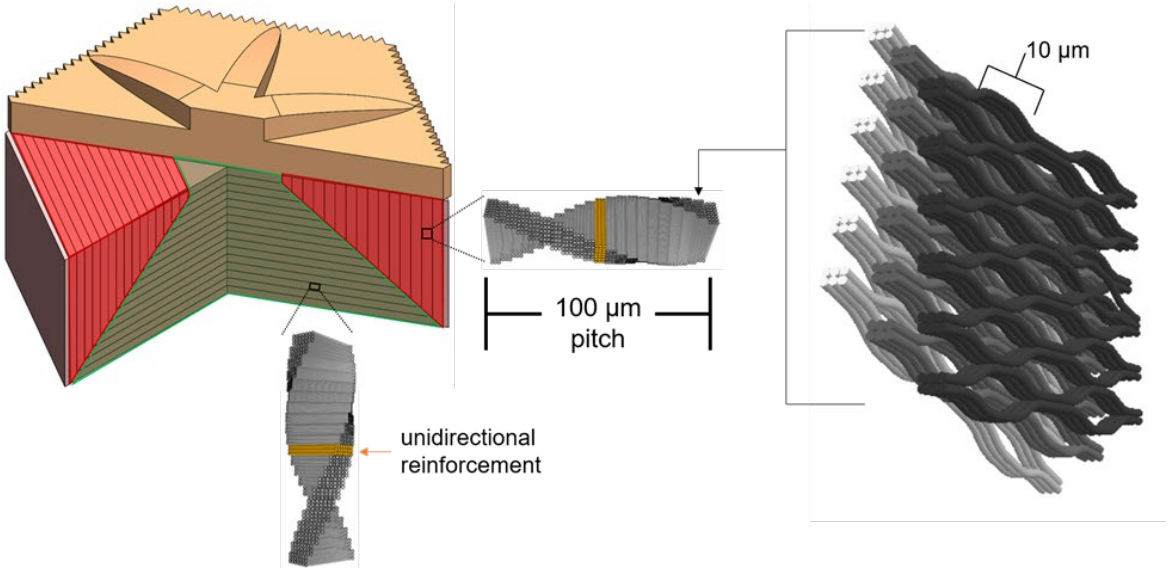

Figure 1.11: Summary of structural characterizations within the collagen beneath a scute. The scute is comprised of a hexagonal nested-box structure that contains rotating lamellae of collagen fibrils that either have its axis of rotation (Bouligand axis) parallel or transverse to the thickness of the scute. The Bouligand structures parallel to thickness dominate the inner and lower regions (green) of the scute, whereas the Bouligand structure transverse dominate the top and outer regions (red), giving rise to the overall nested-box appearance. These Bouligand structures in both regions are reinforced by a separate unidirectional network of collagen fibrils that run transverse the Bouligand axis. µ-CT revealed that the distal/lateral regions contained spiraling interfibrillar gaps that are like those found the exoskeleton of the lobster Homarus americanus and exocuticle of the weevil Curculio longinasus[36-38].

When mechanically tested *in situ,* the scutes showed surprising ductility, especially in shear (Figure 1.12). The stiffness during tensile tests is likely due to the alignment of the unidirectional collagen fibrils in the proximal/central region of the scutes with the tensile axis. Conversely, the ductility observed in shear tests is likely due the non-linear deformation responses previously observed with *in situ* SEM. The dotted lines in Figures 12c,d represent a theoretical maximum where all tissue strains are due to the tensile deformation of the constituent collagen fibrils. The data demonstrate a considerable portion of the tissue strain is not from the fibrils being tracked through SAXS. This is expected, as the collagen in the scute is organized into a complex network that cannot be simply

explained through the fibril strains of only the underlying unidirectional system. Moreover, in Figure 1.12d, a tissue strain of over 40% is observed, while only reaching a fibril strain of ~3%. This corroborates the hypothesis that the system of collagen being observed in the SAXS diffraction patterns is normal to the hexagonal edges of the scutes; therefore, they are perpendicular to the shearing axis explaining why modest fibril tensile strain is observed.

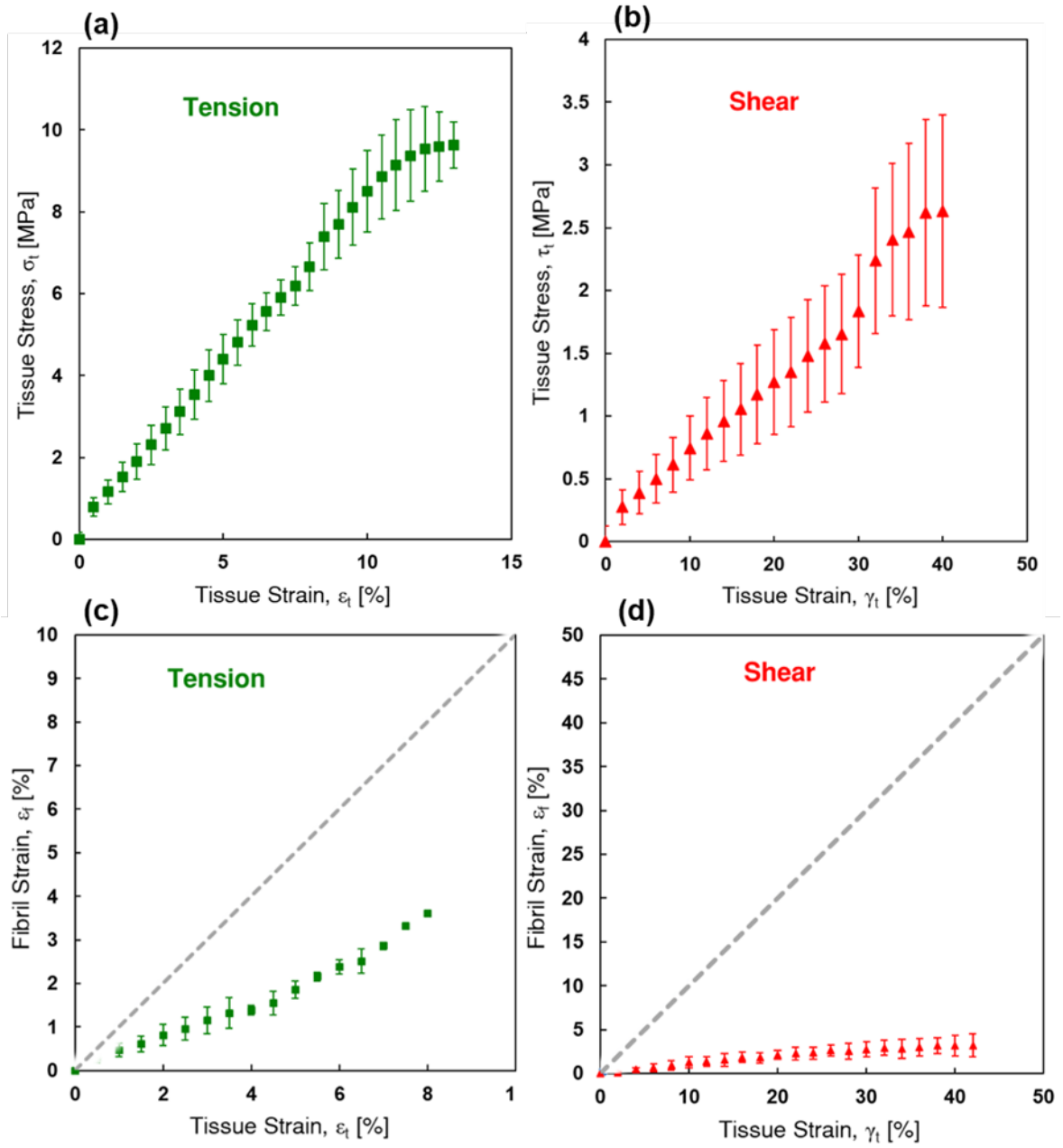

Figure 1.12: Mechanical data produced from *in situ* small-angle x-ray scattering (SAXS) on neighboring scutes with their mineral plates removed; **(a)**, **(c)** and **(b)**, **(d)** are the averaged data from the tensile and shear experiments, respectively. Tissue strain was obtained using digital image correlation to track the relative movements of the surface texture of the collagen network. Fibril strains were taken from the *d*-period arcs produced from the unidirectional fibrils in the proximal/central regions of the scutes. Dotted lines represent a 1:1 relationship between the tissue and fibril strains that would be produced if all strain occurring on the tissue level was due to the stretching or compressing of the constituent collagen fibrils; Results demonstrate the scutes are designed to be stiffer and stronger in a tensile mode, while more ductile in a shear mode.

1.4.5 Finite Element Modeling of Bouligand Structure in Shear

To understand the reason why the S-shape developed in collagen after a shear test, a 3D finite element (FE) model of material element cell was developed by an arrangement of N ($N = 20$) stacked layers of continuum shell elements of thickness l and a pitch distance of L as presented in Figure 1.13a. This material element cell represents the behavior of the Bouligand structure inside the collagen scutes, showing the material element cell in the forms of N helicoidally stacked layers with different orientations. The unit cell contains layers of linear elastic layers with the pitch angle of 9 °.The orthotropic elastic properties that are used for this study are the following [41]:

$$E_1 = 144\ GPa, \nu_{12} = 0.44, G_{12} = 47.2\ GPa$$

$$E_2 = 76\ GPa, \nu_{13} = 0.06, G_{13} = 25.6\ GPa$$

$$E_3 = 82\ GPa, \nu_{23} = 0.18, G_{23} = 41.3\ GPa$$

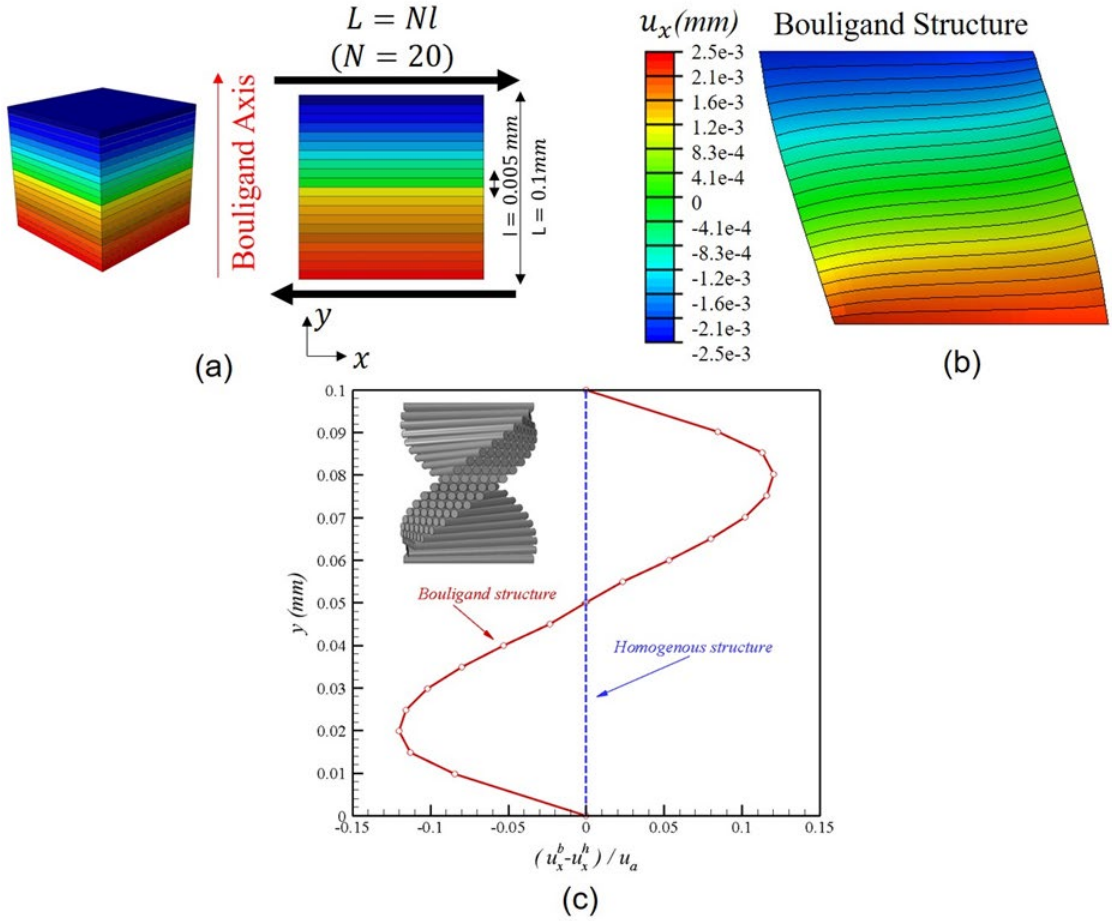

Figure 1.13: **(a)** Schematic diagram of the layered model for finite element modeling studies. The parameter, L is the pitch distance (the distance to make a rotation of 180˚); l is the layer thickness; N is the number of layers in the pitch and is equal to 20; **(b)** horizontal displacement of element unit cell for Bouligand cells; **(c)** the normalized horizontal displacements of Bouligand structure and homogenous material along vertical (y) direction. Directions u_x^b and u_x^h represent the horizontal displacement for the Bouligand structure and homogenous unit cell, respectively. Direction u_a represents the horizontal length of the unit cell.

The layers are completely bonded together, and shear displacement-controlled load is applied to the top and bottom surface of the model. The horizontal displacement (u_x) of the Bouligand unit cell under shear loading is presented in Figure 1.13b. The comparison between normalized horizontal displacement of both a homogenized material and the Bouligand microstructure are presented in Figure 1.13c. Results present a S-shape response for the Bouligand unit cell although the material assigned to the layers is linear elastic. This

nonuniform displacement distribution can be related to the Bouligand orientation of the unit cell and thus, one can conclude that the Bouligand orientation inside the unit cell induces a non-homogeneous displacement across an entire pitch.

1.4.6 Finite Element Modeling of Collagen Interface between Scutes

1.4.6.1 Collagen scute geometry

Table 1.1: The initial geometry of the collagen scutes used for the tensile test.

Test numbers	**Average width (mm)**	**Average thickness (mm)**	**Initial length L_0 (mm)**
Lower bound	3.76	0.54	2.68
Upper bound	3.38	0.64	2.94

FE models of the collagen scutes without mineralized plates (similar to those examined in the *in situ* SEM tests) were developed to characterize both the collagen and its interface connection. Testing a single coupon sample of scutes was too difficult due to their small size; as a result, the *in situ* SEM tensile experiments were performed between two scutes without mineralized plates. Such *in situ* SEM tests generated a variety of stress-strain curves. The upper and lower load-displacement curves from experimental tests are termed as the upper and lower bounds, respectively. The dimensions of the scutes related to the upper and lower bounds are presented in Table. 1. In the modeling, the effect of the Bouligand microstructure was ignored inside the collagen and an interface between the hexagonal collagen base was modeled with zero thickness cohesive elements, as shown in Figure 1.14a.

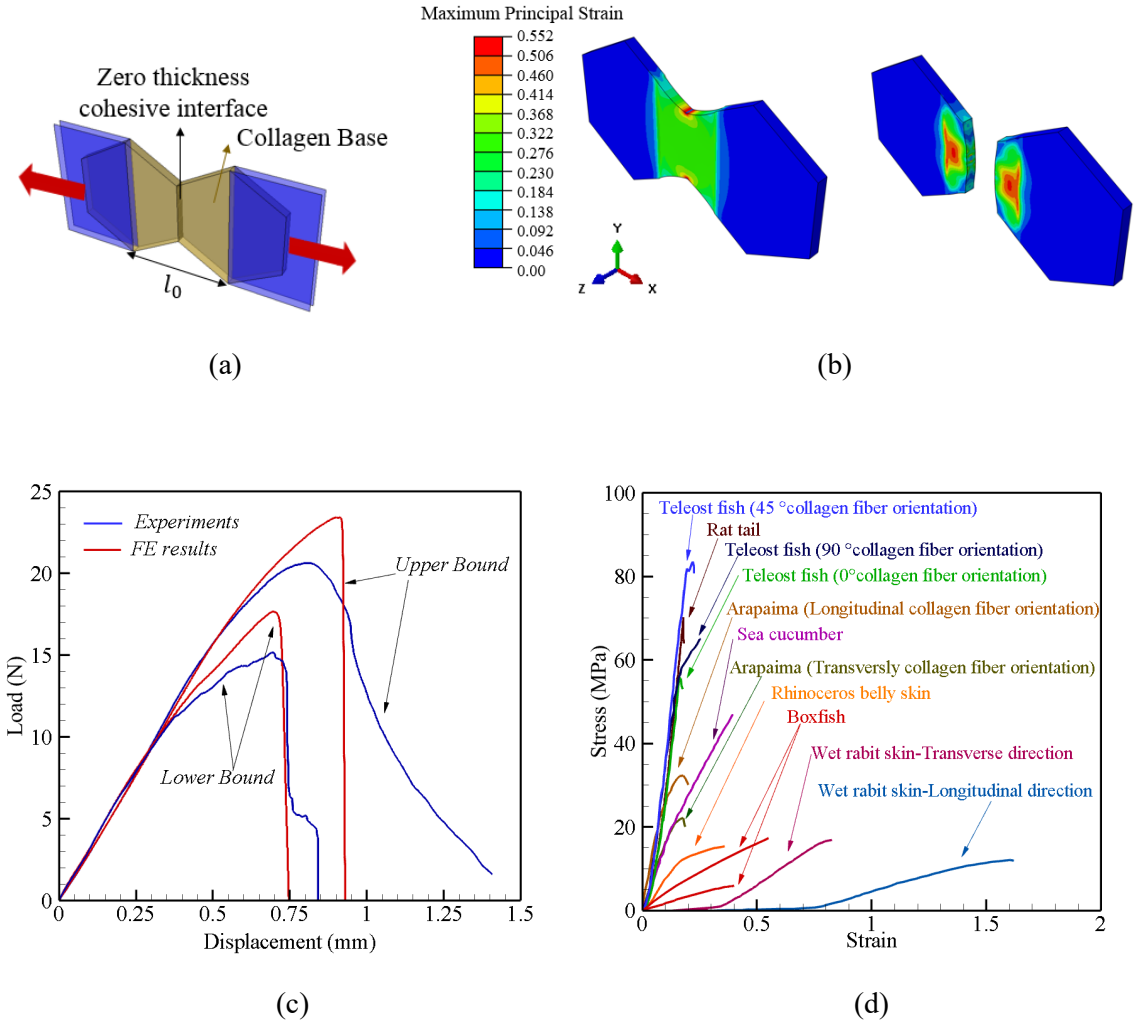

Figure 1.14: Finite element (FE) model for two collagen scute, **(a)** boundary condition and geometry of the two collagen along with the zero thickness cohesive interface, **(b)** the maximum principal strain distribution along two collagen scute under tensile loading in the middle of loading and after separation, **(c)** a comparison between the load-displacement curves from the FE models for the upper and lower bounds and SEM tests of two collagen scute, **(d)** a comparison between the stress-strain curve of collagen in boxfish and various other collagen-based materials [42-47].

1.4.6.2 Type I Collagen and Interface Characterization

The mechanical properties of pure collagen are not available in the literature. Previous studies on collagen of different species do not necessarily represent collagen materials that are pertinent to boxfish scutes, but instead present a wide spectrum of collagen with varying fibril densities and orientations [42-47]. Type I collagen is found in

body of many animals in nature; for example, rat tail, rabbit skin, human skin, human tendons, bone [42-47]. In all the cases, the collagen has shown a hyperelastic behavior. Thereby, in this section a parametric and systematic study was run to develop the stress-strain curves for collagen in boxfish scute using the experimental data from our *in situ* SEM tensile tests. Since the *in situ* test was not a pure uniaxial test, the stress-strain curve for collagen cannot be obtained directly. As such, several FE analyses were needed to fit the correct behavior of both the collagen and interface. The process of separation between two scutes under tensile loading, based on SEM observation [4], confirmed that separation between two scutes occurs along the interface between two scutes in the underlying collagen base.

The initial stiffnesses from the stress-strain curves in the *in situ* experiments are related to the hexagonal collagen base material while, the interface is mainly responsible for the values of peak stress and failure strain obtained from the stress-strain curves. Several FE simulations with various hyperelastic ranges, including the geometry of the upper and lower bounds, were developed to estimate the initial stiffness of the collagen base. In the FE models, once the correct initial stiffness of the collagen was determined, the next step was to develop an accurate model for the cohesive interface. The bilinear separation law in ABAQUS [48] can be defined by two parameters, the maximum normal strength (σ_{max}), and fracture energy (G_{IC}).

To validate the uniqueness of the result for the cohesive interface, two sets of parametric analyses were conducted. For the first case study, the maximum strength was kept constant, and the fracture energy was changed, while for the second case study, the

fracture energy was kept constant, and the value of maximum stress was varied. The results were found to produce a good match of the simulations and these parametric studies and are presented in Table 2 and Figure 1.14.

1.4.6.3 Finite element results and discussion

The Lagrangian strain contour of the FE model for two-collagen bases during tensile loading and after separation is presented in Figure 1.14b. The FE results state that the strain concentration occurs along the interface area. A comparison between the finite element model and SEM tensile tests of two collagen scutes without the mineralized plate is presented in Figure 1.14c. The displacement-controlled load was applied on the boundary condition for the FE models. As the displacement increases in the boundaries, the value of reaction force increases up to the peak load. The comparison between FE simulation and experiments confirmed similar initial stiffness for both upper and lower bounds. As previously discussed, the nominal strength of the interface is responsible for the peak load in the force-displacement curve. After reaching the peak load, the interface starts stretching until the separation occurs between two hexagonal collagen scutes. In the modeling, the cohesive elements of the interface are removed as they reach the final fracture energy and a complete separation can be observed in simulations after all the cohesive elements were removed (Figure 1.14b). For the purpose of comparison, the stress-strain curves of type I collagen of various animals with the type I collagen in boxfish (results from the characterization) are presented in Figure 1.14d [42-47]. For the purpose of comparison, the stress-strain curves of type I collagen of various animals with the type I collagen in boxfish (results from the characterization) are presented in Figure 1.14d [42-

47]. These curves offer enormous variety in the stress-strain curves of collagen because the collagen fibril's hierarchical organization varies among different species and tissues. Finally, there is excellent agreement between the load-displacement curves for simulation and experimental results.

Table 1.2: Cohesive interface characterization using ABAQUS for the lower and upper bounds

	Maximum normal strength σ_{max} **(MPa)**	**Fracture energy** G_{IC}
Lower bound	12	5
Upper bound	15	8

1.5 Conclusions

While other fish species ensure flexibility of both their armor and bodies through overlapping scales, the rigid-bodied boxfish utilizes unique adaptations to delocalize compressive stress from predator bites, thereby providing itself a higher level of defense than its counterparts. The results described here point to numerous mechanisms that the boxfish employs to ensure its defense. Confocal microscopy and micro-computed tomography (μ-CT) revealed that underneath the mineralized plate is a complex system of collagen fibrils in a Bouligand-type structure organized into a higher-order nested-box structure. As observed through *in situ* scanning electron microscopy (SEM) mechanical testing and confirmed through finite element analysis, the Bouligand structure will deform and align with loading, allowing for some manner of mechanical property isotropy. *In situ* small-angle x-ray scattering further reveals the complex network of collagen and shows how individual collagen fibrils get stretched and compressed to accommodate the whole-

scute's change of shape and deformation. This complex organization of stretched/compressed fibrils allows for relatively large levels of tissue strain to occur without inducing scute fracture, providing enhanced ductility and toughness. Furthermore, the collagen interface between scutes is less dense and complex in structure than the organized interior of the scute. In addition, the mineralized sutures account for only ~4% of the thickness of the interface and provide little or no mechanical advantage there. Failure both with the mineralized plate and without occurs at the interface with little or no damage to the scute interior. All of this results in a structure that ensures failure occurs predominantly at the interface between scutes where greater flexibility can be achieved while maintaining the complex interior of the scute intact.

Based upon this study's results on the structure and *in-situ* failure mechanisms of the boxfish's rigid armor, the following conclusions can be made:

- The boxfish employs a novel Bouligand-type structure (nested-box) that employs abrupt 90° shifts in its orientation that is unlike any other Bouligand-type structures found in nature.
- A rare analog of the Bouligand-structure is observed in the distal/lateral regions referred to as a honeycomb structure previously seen in the exoskeleton of the *Homaris americanus* lobster and the exocuticle of the *Curculio longinasus* weevil.
- The interfaces of the boxfish's scutes are less dense and complex than the interior and feature very little mechanical reinforcement from the mineralized surface plate and interlocking sutures. This structure provides flexibility at the interface and ensures that failure occurs at specific locations when mechanically stressed in tension or shear. The

combination of a compliant interface and stiff interior to the boxfish's scutes allows for it to maintain some flexibility for both motion and defense despite its rigid and non-overlapping armor.

- The interior of the boxfish's scutes consist of a complex collagen-based structure that combines a unidirectional network of collagen fibrils intersecting with Bouligand-type structures. When mechanically stressed, these structures are capable of deforming to align with the applied force and provide damage resistance. These adaptations allow for the interior of the boxfish's scutes to resist damage and provide defense.
- The 3D finite element results of the unit cell with the Bouligand microstructure confirm the S-shape shear deformation response seen in experimental results with *in situ* SEM and suggest this unique response is due to the Bouligand orientation of the unit cell.

Further studies on the complex and novel collagen structure of the boxfish will aid in the field of bioinspired fiber reinforced materials, and more specifically in understanding the different tropes and utility of a Bouligand, or twisted plywood, structure. These novelties that are worth further exploration for use in lightweight reinforced materials are the following:

1. Utilization of abrupt 90° changes in the orientation of Bouligand structures, overall referred to as the nested-box structure. We hypothesize this is used in response to converting compressive biting forces into a delocalized concave bending that both interlocks the mineral scutes and also applies in-plane compressive forces which align with the distal/lateral Bouligand axis. Exploring the nested-box Bouligand structure under bending may further elaborate on the utility of this novel structure.

2. Employing the honey-comb structure, also seen in the lobster *Homarus americanus* and the weevil *Curculio longinasus* [37-39]. This structure is previously proposed to both supply microchannels for nutrients supply and also to provide a high density of interfaces to avoid fiber pullout. Exploring bio-inspired fiber composites that can utilize the channels of a honey-comb derivative of a Bouligand structure for transport of a self-healing matrix or to help tune the bulk density are likely worth exploring.
3. The boxfish applies a combination of Bouligand structures with unidirectional fibrous networks of collagen, and further exploring this strategy may reveal how to further control the mechanical properties of Bouligand structures in specified directions under various loading conditions.

1.6 Acknowledgements

Chapter 1, in part, is published as "The role of collagen in the dermal armor of the Boxfish" Journal of Materials Research and Technology" Journal of Materials Research and Technology, 9(6), 13825–13841, November 2020. This work was coauthored by Garner, S. N., Naleway, S. E., Hosseini, M. S., Acevedo, C., Gludovatz, B., Schaible, E., Jung, J.-Y., Ritchie, R. O., Zavattieri, P., & McKittrick, J. The dissertation author is the first and corresponding author of this work. This work is supported by a Multi-University Research Initiative through the Air Force Office of Scientific Research (AFOSR-FA9550-15-1-0009). We thank the A.Z. Weber group for providing their tensile stage, which was supported by DOE EERE Fuel-Cell Performance and Durability Consortium (FC-PAD). This work was performed in part at the San Diego Nanotechnology Infrastructure (SDNI)

of UCSD, a member of the National Nanotechnology Coordinated Infrastructure, which is supported by the National Science Foundation (Grant ECCS-1542148). This work used the Extreme Science and Engineering Discovery Environment (XSEDE), which is supported by National Science Foundation grant number ACI-1548562 [49]. We also acknowledge the use of beamline 7.3.3 at the Advanced Light Source, which is supported by the U.S. Department of Energy, Office of Science, Office of Basic Energy Sciences, Division of Materials Sciences and Engineering, under contract no. DE-AC02-05CH11231 to the Lawrence Berkeley National Laboratory. Special thanks are due to Prof. P. Hastings of the Scripps Institute of Oceanography, UC San Diego, for providing the boxfish specimens and Dr. James Tyler of the Smithsonian for helpful discussions.

1.7 References

[1] Naleway SE, Porter MM, McKittrick J, Meyers MA. "Structural design elements in biological materials: Application to bioinspiration." Advanced Materials (2015);27:5455-5476.

[2] Meunier FJ, Francillon Viellot H. "Structure and mineralization of the scutes in ostracion lentiginosum (Teleostei, tetraodontiforme, ostraciidae)." Annales des Sciences Naturelles-Zoologie et Biologie Animale (1995);16:33-46.

[3] Besseau L, Bouligand Y. "The twisted collagen network of the box-fish scutes." Tissue & Cell (1998);30:251-260.

[4] Yang W, Naleway SE, Porter MM, Meyers MA, McKittrick J. "The armored carapace of the boxfish." Acta Biomaterialia (2015);23:1-10.

[5] Naleway SE, Taylor JRA, Porter MM, Meyers MA, McKittrick J. "Structure and mechanical properties of selected protective systems in marine organisms." Materials Science and Engineering C (2016);59:1143-1167.

[6] Yang W, Chen IH, Gludovatz B, Zimmermann EA, Ritchie RO, Meyers MA. "Natural flexible dermal armor." Advanced Materials (2013);25:31-48.

[7] Zhu D, Ortega CF, Motamedi R, Szewciw L, Vernerey F, Barthelat F. "Structure and mechanical performance of a “modern” fish scale." Advanced Engineering Materials (2012);14:B185-B194.

[8] Zhu DJ, Szewciw L, Vernerey F, Barthelat F. "Puncture resistance of the scaled skin from striped bass: Collective mechanisms and inspiration for new flexible armor designs " Journal of the Mechanical Behavior of Biomedical Materials (2013);24:30-40.

[9] Bruet BJF, Song JH, Boyce MC, Ortiz C. "Materials design principles of ancient fish armour." Nature Materials (2008);7:748-756.

[10] Song JH, Ortiz C, Boyce MC. "Threat-protection mechanics of an armored fish." Journal of the Mechanical Behavior of Biomedical Materials (2011);4:699-712.

[11] Yang W, Sherman VR, Gludovatz B, Mackey M, Zimmermann EA, Chang EH, Schaible E, Qin Z, Buehler MJ, Ritchie RO, Meyers MA. "Protective role of Arapaima gigas fish scales: Structure and mechanical behavior." Acta Biomaterialia (2014);10:3599–3614.

[12] Yang W, Gludovatz B, Zimmermann EA, Bale HA, Ritchie RO, Meyers MA. "Structure and fracture resistance of alligator gar (Atractosteus spatula) armored fish scales." Acta Biomaterialia (2013);9:5876-5889.

[13] Zimmermann EA, Gludovatz B, Schaible E, Dave NKN, Yang W, Meyers MA, Ritchie RO. "Mechanical adaptability of the Bouligand-type structure in natural dermal armour." Nature Communications (2013);4:2634.

[14] Bouligand Y. "Twisted fiberous arrangements in biological materials and cholesteric mesophases." Tissue & Cell (1972);4:189-217.

[15] Dastjerdi AK, Barthelat F. "Teleost fish scales amongst the toughest collagenous materials." Journal of the Mechanical Behavior of Biomedical Materials (2015);52:95-107.

[16] Sharma V, Crne M, Park JO, Srinivasarao M. "Bouligand structures underlie circularly polarized iridescence of scarab beetles: A closer view" Materials Today: Proceedings (2014); 1: 161-171.

[17] Yang R, Zaheri A, Gao W, Hayashi C, Espinosa HD (2017). "Exoskeletons: AFM identification of beetle exocuticle: Bouligand structure and nanofiber anisotropic elastic properties." Advanced Functional Materials, 27(6).

[18] Yaraghi NA, Guarín-Zapata N, Grunenfelder LK, Hintsala E, Bhowmick S, Hiller JM, Betts M, Principe EL, Jung JY, Sheppard L, Wuhrer R, McKittrick J, Zavattieri P, Kisailus D. "Biocomposites: A Sinusoidally Architected Helicoidal Biocomposite." Advanced Materials (2016);28(32):6769-6769.

[19] Suksangpanya N, Yaraghi NA, Kisailus D, Zavattieri P. "Twisting cracks in Bouligand structures." Journal of the Mechanical Behavior of Biomedical Materials (2017);76, 38-57.

[20] Vernerey FJ, Barthelat F. "Skin and scales of teleost fish: Simple structure but high performance and multiple functions " Journal of the Mechanics and Physics of Solids (2014);68:66-76.

[21] Vernerey FJ, Barthelat F. "On the mechanics of fishscale structures " International Journal of Solids and Structures (2010);47:2268-2275.

[22] Vernerey FJ, Musiket K, Barthelat F. "Mechanics of fish skin: A computational approach for bio-inspired flexible composites." International Journal of Solids and Structures (2014);51:274-283.

[23] Lin YS, Wei CT, Olevsky EA, Meyers MA. "Mechanical properties and the laminate structure of Arapaima gigas scales." Journal of the Mechanical Behavior of Biomedical Materials (2011);4:1145-1156.

[24] Wang B, Yang W, Sherman VR, Meyers MA. "Pangolin armor: Overlapping, structure, and mechanical properties of the keratinous scales." Acta Biomaterialia (2016);41:60-74.

[25] Connors MJ, Ehrlich H, Hog M, Godeffroy C, Araya S, Kallai I, Gazit D, Boyce M, Ortiz C. "Three-dimensional structure of the shell plate assembly of the chiton Tonicella marmorea and its biomechanical consequences." Journal of Structural Biology (2012);177:314.

[26] Martini R, Barthelat F. "Stretch-and-release fabrication, testing and optimization of a flexible ceramic armor inspired from fish scales." Bioinspiration & Biomimetics (2016);11, 066001.

[27] Li Y, Ortiz C, Boyce MC. "A generalized mechanical model for suture interfaces of arbitrary geometry." Journal of the Mechanics and Physics of Solids (2013);61:1144-1167.

[28] Li Y, Ortiz C, Boyce MC. "Stiffness and strength of suture joints in nature." Physical Review E (2011);84, 062904.

[29] Li Y, Ortiz C, Boyce MC. "Bioinspired, mechanical, deterministic fractal model for hierarchical suture joints." Physical Review E (2012);85:031901.

[30] Feilden E, Ferraro C, Zhang Q, García-Tuñón E, D'Elia E, Giuliani F, Vandeperre L, Saiz E. "3D printing bioinspired ceramic composites." Scientific Reports (2017);7(1).

[31] Natarajan B, Krishnamurthy A, Qin X, Emiroglu CD, Forster A, Foster EJ, Weder C, Fox DM, Keten S, Obrzut J, Gilman JW. "Binary cellulose nanocrystal blends for bioinspired damage tolerant photonic films." Advanced Functional Materials (2018);28(26), 1800032.

[32] Nguyen T, Peres BU, Carvalho RM, Maclachlan MJ. "Photonic hydrogels from chiral nematic mesoporous chitosan nanofibril assemblies." Advanced Functional Materials (2016);26(17):2875-2881

[33] Hastings PA, Walker HJ, Galland GR. "Fishes: a guide to their diversity." Berkeley: University of California Press (2015).

[34] Hexemer A, Bras W, Glossinger J, Schaible E, Gann E, Kirian R, MacDowell A, Church M, Rude B, Padmore H. "A SAXS/WAXS/GISAXS beamline with multilayer monochromator" Journal of Physics: Conference Series (2010);247, 012007.

[35] Barth HD, Zimmermann EA, Schaible E, Tang SY, Alliston T, Ritchie RO. "Characterization of the effects of x-ray irradiation on the hierarchical structure and mechanical properties of human cortical bone." Biomaterials (2011);32(34):8892-8904.

[36] Meek KM, Quantock AJ. "The use of x-ray scattering techniques to determine corneal ultrastructure." Progress in Retinal and Eye Research (2001);20(1):95-137.

[37] Raabe D, Romano P, Sachs C, Al-Sawalmih A, Brokmeier H, Yi S, Servos G, Hartwig H.. "Discovery of a honeycomb structure in the twisted plywood patterns of fibrous biological nanocomposite tissue." Journal of Crystal Growth (2005);283(1-2):1-7.

[38] Romano P, Fabritius H, Raabe D. "The exoskeleton of the lobster Homarus americanus as an example of a smart anisotropic biological material. Acta Biomaterialia (2007);3(3):301-309.

[39] Jansen MA, Singh SS, Chawla N, Franz NM. "A multilayer micromechanical model of the cuticle of Curculio longinasus Chittenden, 1927 (Coleoptera: Curculionidae)." Journal of Structural Biology (2016);195(2):139-158.

[40] Chintapalli RK, Mirkhalaf M, Dastjerdi AK, Barthelat F. "Fabrication, testing and modeling of a new flexible armor inspired from natural fish scales and osteoderms." Bioinspiration & Biomimetics (2014);9(3), 036005.

[41] Barthelat F, Li CM, Comi C, Espinosa HD. "Mechanical properties of nacre constituents and their impact on mechanical performance." Journal of Materials Research (2006);21(8): 1977-1986.

[42] Gentleman E, Lay AN, Dickerson DA, Nauman EA, Livesay GA, Dee KC. "Mechanical characterization of collagen fibers and scaffolds for tissue engineering." Biomaterials (2003);24(21):3805-3813.

[43] Haut RC. "The influence of specimen length on the tensile failure properties of tendon collagen." Journal of biomechanics (1986);19(11):951-955.

[44] Miyazaki H, Kozaburo H. "Tensile tests of collagen fibers obtained from the rabbit patellar tendon." Biomedical Microdevices (1999);2(2):151-157.

[45] Yang Tingting, Wen Wang, Hongze Zhang, Xinming Li, Jidong Shi, Yijia He, Quan-shui Zheng, Zhihong Li, and Hongwei Zhu. "Tactile sensing system based on arrays of graphene woven microfabrics: electromechanical behavior and electronic skin application." ACS nano (2015);9(11):10867-10875.

[46] Rigby, Bernard J., Nishio Hirai, John D. Spikes, and Henry Eyring. "The mechanical properties of rat tail tendon." The Journal of general physiology 43, no. 2 (1959): 265-283.

[47] Freed AD, Doehring TC. "Elastic model for crimped collagen fibrils." Journal of biomechanical engineering (2005);127(4):587-593.

[48] ABAQUS 2018 Abaqus Analysis User's Manual (RI, USA: SIMULIA Inc)

[49] John Towns, Timothy Cockerill, Maytal Dahan, Ian Foster, Kelly Gaither, Andrew Grimshaw, Victor Hazlewood, Scott Lathrop, Dave Lifka, Gregory D. Peterson, Ralph

Roskies, J. Ray Scott, Nancy Wilkins-Diehr, "XSEDE: Accelerating Scientific Discovery", Computing in Science & Engineering, vol.16, no. 5, pp. 62-74, Sept.-Oct. 2014, doi:10.1109/MCSE.2014.80

CHAPTER 2: Mechanical Optimization of Diatomite Monoliths from Freeze-Casting for High-throughput Applications

2.1 Abstract

The silica cell wall of a diatom, abundant microalgae 1 – 100 μm in size, contains highly ordered hierarchical porosity and is widely available through its fossilized form, diatomite. The goal of this research is to use this cost-effective source of porous silica in a unidirectional freezing process called ice-templating, or freeze-casting, to create a ceramic membrane with unidirectional lamellar walls (~15 μm) that allows for efficient mass transport of fluids (i.e., low pressure-drop) while maintaining sufficient mechanical properties. In this study, control over the monoliths was explored by varying the mass ratio of diatomite and sodium carbonate and the solids ratio in the initial slurry before freeze casting. The resultant monolith's properties are measured using scanning electron microscopy, mercury intrusion porosimetry, and mechanical testing. The membranes then undergo in-line vacuum filtration of methylene blue dye and monodisperse latex beads to quantify the membranes filtration performance through chemical adsorption and depth filtration capabilities, respectively. Control over the bioinspired ceramic monolith's material properties allows for a cost-efficient and hierarchically porous ceramic template with efficient mass transfer capabilities that can be potentially functionalized with a plethora of sophisticated nanomaterials for various adsorbent, filter, catalysis, and sensor applications.

2.2 Introduction

The field of ceramic membranes has been around for centuries and is still experiencing rapid growth through novel innovations. Applications range from liquid treatment (e.g., wastewater and food/beverage industries) and gas separation to use in the energy sector as hydrogen fuel cells [50]. Ceramic membranes have been replaced with polymer membranes in recent decades due to the cost-effectiveness of the latter, even considering the higher fluxes and lifetimes of ceramic membranes [50]. This is because ceramic membranes usually require expensive starting materials, and the fabrication processes are more complex. Therefore, research into using cheaper starting materials and utilizing novel fabrication processes may aid in improving several fields in which ceramic membranes can be implemented.

Diatomaceous earth, or diatomite, is the fossilized form of diatoms, which are a unicellular photosynthetic microalga with over 100,000 different species that each produce intricately unique and hierarchically porous silica shells called frustules [51, 52]. Diatomite is mined throughout the world (approximately 1.8 million tons per year) and sold most commonly as a cheap commercial farm feed dehydrant and insecticide [53]. More generally, diatom nanotechnology has seen a surge in engineering applications in recent decades throughout several fields, including drug delivery, biosensing, filtering, and catalysis [54-56]. This interest is due to diatom's abundance and their multitude of physical/chemical properties. These include excellent open porosity for mass-transfer, extended drug release features, ease of functionalization, and their non-toxic and cost-efficiency otherwise not possible with porous synthetic silica [51, 57]. Recent research has

been exploring genetic control over the complex frustule geometries and for their industry-scaled bioproduction for the emerging fields utilizing them [58-60]. Until these pursuits are actualized, diatomite has been used as a cheaper and more available form of diatoms, where fractured frustules and mineral impurities are to be dealt with.

A key industry utilizing diatomite is the field of water treatment and filtration, dating back to 1890 [55, 61-67]. Typically, diatomite in water treatment is used as a filter aid for pre-coat filtration and processed into a filter candle [63]. However, when packed into a bed there is a high probability that closed pores are formed which leads to inefficient use of volume, negatively affecting the flux during filtration. Recent research into diatomite membranes have been adopting novel processes of forming monoliths (i.e. hydrothermal production, foam-gelcasting, and spark-plasma sintering with compression molding) to explore potential cheaper processing routes, to enable easier methods of extraction and regeneration, and to produce microstructures which may further benefit membrane properties [68-74]. The foam-gelcasting of diatomite membranes notably produces more porous monoliths compared to its counterparts (bulk density of 0.35 to 0.45 g/cm^3) and ensures an efficient use of the entire volume of the diatomite membranes by minimizing closed porosity and providing efficient mass-transfer channels [69, 70].

A novel method, known as freeze casting (or ice-templating), has garnered increasing interest in several fields that benefit from the material-agnostic process which produces micro-porous monoliths [75, 76]. Freeze casting is an ice-templating process which directionally freezes a slurry such that the particles within the slurry are rejected from the growing crystals (usually ice) and under certain conditions form staggered, or

lamellar, walls of particles and ice. The frozen monoliths are then freeze dried to carefully remove the ice which produces open porosity where all the ice originally formed. If the constituent particles are inorganic, a final sintering process ensures rigidity of the green body. Few publications have demonstrated potential for these porous monoliths to be used for filtration purposes [77-79]. Among them, Chen et al. [78] utilized diatomite as the constituent material in the freeze casting process and demonstrated the resulting hierarchically porous membranes are capable of efficiently separating oil from water. This research aims to further explore these freeze caste diatomite monoliths for their potential in producing cost-effective ceramic membranes which utilize the open porosity of the diatom frustules as well as the open microstructure from the freeze casting process. Recent research also demonstrated incorporating 3D printing sacrificial scaffolding in freeze caste monoliths to yield macrostructural control [80] which shows promise for future applications that look to have substantial control over several length scales. By combining the advents of structural control from the macro-microscale in the field of freeze casting with the structural diversity of diatom frustules and further nanostructural functionalizations (i.e. metal-organic frameworks, zeolites, nanoparticles, and shape-preserving chemical alterations) of them, the future of diatomite freeze caste monoliths will potentially produce a wide-reaching array of applications [51, 56, 69, 74, 81-87].

This work explores the trade-off between mechanical strength and porosity of the freeze caste diatomite monoliths through the addition of a flux agent (i.e., sodium carbonate) in the initial slurry. Previous studies have demonstrated sodium carbonate as the optimal flux agent when considering diatomite as a filter aid [88, 89]. Lastly, we

demonstrate the ability of the membranes to undergo pressurized in-line flow without mechanical failure which demonstrate potential for these membranes to be functionalized for use in high-flux applications or in applications which benefit from efficient hierarchical mass-transfer.

2.3 Materials and Methods

2.3.1 Freeze-Casting

A similar freeze casting method was applied as done in Chen et al. [78]. Aqueous slurries were created by mixing food-grade diatomite powder (Fossil Shell Flour®, purchased from Perma-Guard Inc., USA.) and deionized water with varying concentration (i.e., 0, 3, 5, 7, and 9 wt. % of total ceramics) of sodium carbonate anhydrous (Fischer Scientific S263). Each slurry contained polymer binders (1 wt. % of Polyvinyl alcohol, 98–99% hydrolyzed, average molecular weight (M.W.) 88,000–97,000, Alfa Aesar, USA and 1 wt. % of polyethylene glycol, average M.W. 5400–6600, Alfa Aesar, USA), and a dispersant (3 wt. % of sodium polyacrylate anionic dispersant, DARVAN® 811, Vanderbilt Minerals, USA). The slurry was heated up to approximately 90 °C while stirring for 15 minutes.

The obtained slurry was poured into PVC tube and attached to the freeze-casting device previously described [77], representation shown in Figure 2.1. A copper finger connects a proportional-integral-derivative controller, the slurry, and a liquid nitrogen bath to enable a controlled cooling from 20 to -170 °C at a rate of 10 °C/min of the diatomite slurry. The slurry was held -170 °C for 30 minutes before the scaffold was removed from the mold and put into a freezer to be held until the subsequent freeze-drying step. Multiple

scaffolds (5-10) were added to the freeze dryer (Labconco, Kansas City, MO) at -50 °C and 350 Pa for 48 h. The green bodied scaffolds were then sintered in an open-air furnace at a rate of 5 C/min to 1050 °C, held at 1050 °C for 4 hours, and cooled at 10 °C/min to room temperature. Finally, the top and bottom 5 mm were removed using a PCS-400 sectioning saw with a DB412-8 diamond blade (Mark V Lab, East Granby, Connecticut). The scaffolds were then cut into 3 – 4 mm thickness membranes still maintaining the same diameter as the original scaffolds (~ 11 mm).

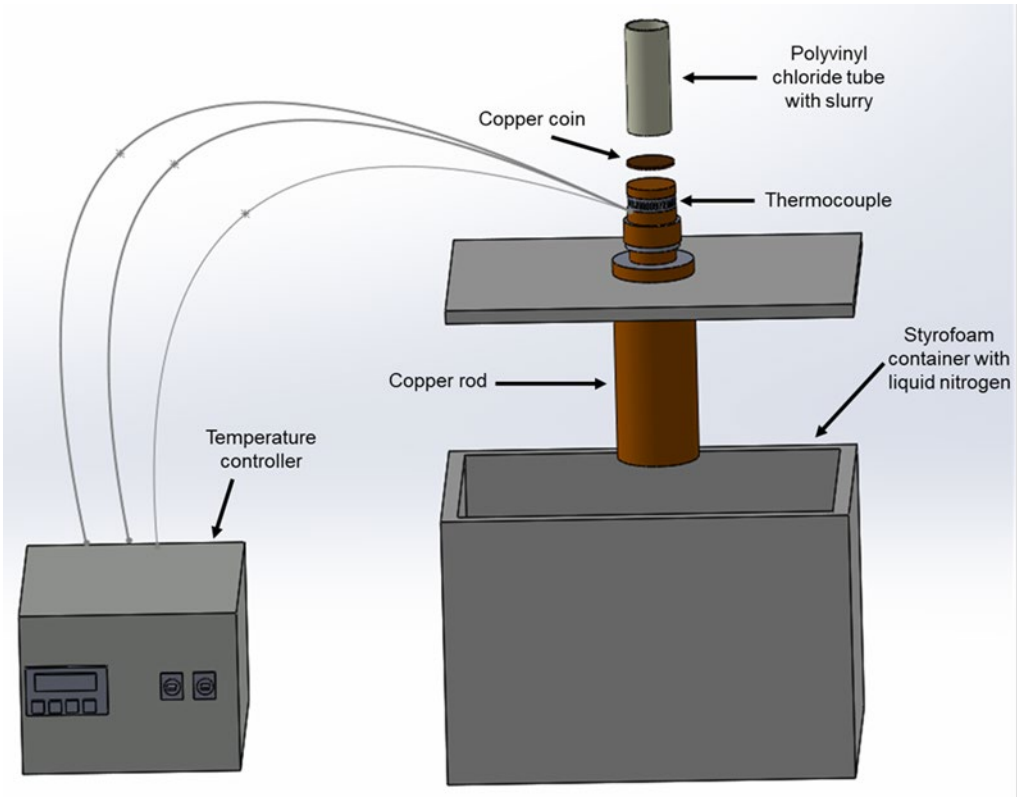

Figure 2.1: Unidirectional freeze cast (or ice-templating) set-up used for fabrication of diatomite membranes. Styrofoam container holds the liquid nitrogen where the copper rod protrudes inside that is connected to the copper coin and polyvinyl tube shown here. The cooling from nitrogen is measured and controlled to a rate of 10 C°/min using a thermocouple attached to a temperature controller. The scaffolds are frozen to -170 C° and thermally soaked for 30 minutes before subsequent freeze drying.

2.3.2 Material Characterization

2.3.2.1 Structural Analysis

Structural analyses were performed using multiple techniques consisting of scanning electron microscopy (SEM), microcomputed tomography (μ-CT), nitrogen sorption analysis, and mercury porosimetry. SEM was performed using a FEI Quanta FEG250 (Thermo Fisher Scientific, Waltham, Massachusetts) using an electron voltage of 5 kV. Samples were prepared by fixing the diatomite membranes onto aluminum pucks with double-sided carbon tape on the bottom and wrapped around the edges of the membrane. The samples were sputter coated in iridium prior SEM using a K575X Iridium Sputter Coater (Emitech, Montigny, France) to ensure maximum electron conduction. M-CT was performed using a Zeiss Versa 510 microscope with a voxel size of 7.3673 μm, with 1601 projection images using a 40 kV voltage. The images were edited and stitched together using Amira software (Thermo Fisher Scientific, Waltham, Massachusetts) to create a high-resolution 3-dimensional image. N_2 physisorption analyses were performed on an ASAP 2020 (Micrometrics, Norcross, GA) applying the Brunauer–Emmett–Teller (BET) theory. Prior to analysis, samples were activated under vacuum at 105 °C overnight and experiments were run at 77 K. Mercury porosimetry results were obtained using a PoreMaster-60 Mercury Intrusion Analyzer (Anton Paar Quanta Tech Inc., Boynton Beach, FL). Diatomite membranes were cut into small cubes (1 cm^3) and intruded to a pressure of 4170 PSIA (max pressure before structural collapse of material), corresponding to a reading of pores with diameters down to 50 nm. This was performed on samples containing 5 and 7 wt. % of sodium carbonate.

2.3.2.2 Compositional Analysis

Compositional analyses were performed using x-ray diffraction (XRD) to observe crystalline phases present, energy dispersive spectroscopy (EDS) to observe ratio of elements present, and Fourier-transform infrared spectroscopy (FTIR) to observe functional groups and chemical bonds present in the diatomite membranes. XRD analyses were performed on a D2 Phaser (Bruker AXS Inc., Madison, WI) instrument using Cu Kα radiation with a step size of 0.006° 2θ, a minimum count time of 0.3 s, and a 2θ range from 10 – 60°. EDS was performed using the same microscope used for SEM using an electron voltage of 5 kV. FTIR was performed on a Spectrum Two Spectrometer (Perkin Elmer, Waltham, MA) used in reflection mode with a KBr beam splitter, a mid-IR source, and a lithium tantalate detector. The resolution was 8 cm^{-1} and the frequency range tested was from 400 to 4000 cm^{-1}. The results from XRD and EDS of the raw diatomite purchased is shown in Figure 2.2. Results demonstrate that the powder consists mainly of amorphous silica with modest amounts of aluminum and magnesium.

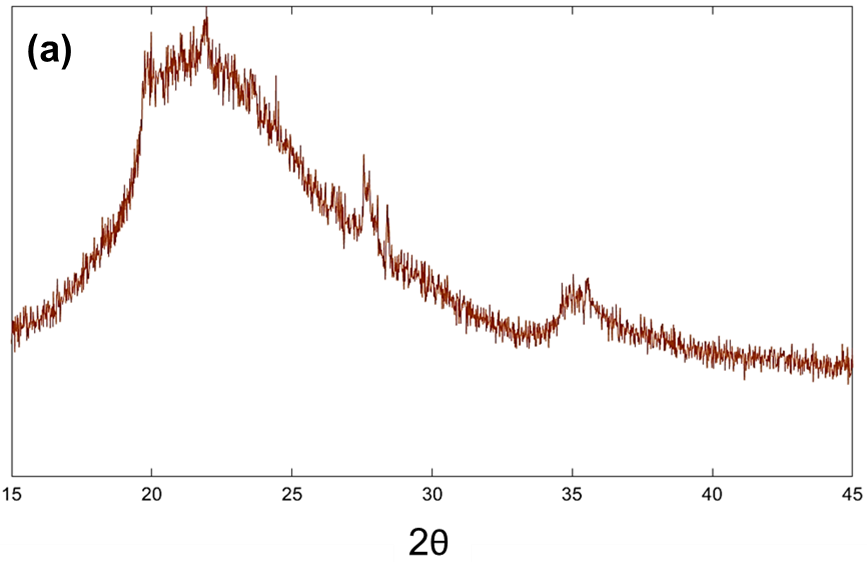

(b)

Element	Atom %
Oxygen	54.79 ± 3.41
Silicon	41.33 ± 3.54
Aluminum	3.25 ± 0.18
Magnesium	0.62 ± 0.15

Figure 2.2: **(a)** X-ray diffraction spectrum of raw food grade diatomite and demonstrates it consists mainly of amorphous silica; **(b)** Energy dispersive spectroscopy results reveal the diatomite is mainly composed of silica and its main impurities are aluminum and magnesium.

2.3.2.3 Mechanical Analysis

The sintered diatomite membranes were cut into cubes 5 mm in all primary dimensions. These cubes were compressed with a strain rate of 0.1% per second in an Instron machine (Instron 3342, Instron, Massachusetts, USA). The cubes were tested in two directions: (1) axial direction (parallel to the direction of ice growth) and (2) transverse direction (orthogonal to the direction of ice growth). The Young's modulus and ultimate compressive strength were determined from the gradient of linear region and maximum

stress on the stress-strain curve. Mechanical testing was performed on all types of scaffolds created (i.e. 0, 3, 5, 7, 9 sodium carbonate wt. %)

2.3.3 Filtration

The custom-built filtration apparatus is shown in Figure 2.3. The cationic methylene blue dye (Sigma-Aldrich M9140) and the monodisperse amine-modified polystyrene beads (florescent red: Sigma-Aldrich L2778) with diameters of approximately 1 μm were used to perform vacuum filtration to quantify the adsorption capabilities of the diatomite freeze caste membranes with varying sodium carbonate (5, 7, and 9 wt. %). Scaffolds with 0 and 3 wt. % of sodium carbonate were omitted due to both the lack of mechanical rigidity to avoid failure under vacuum pressure and also due to their dusty nature which could interfere with spectrophotometry results of the effluents. Initial concentrations of methylene blue dye and latex beads were both 100 mg/g for all experiments. The effluents of methylene blue and latex beads solution were collected, and the concentrations were measured by spectrophotometry (product manufactured by Molecular Devices, LLC. 1311 Orleans Drive, Sunnyvale, California, United States of America 94089. SoftMax Pro Software version 7.0.3). The absorbance mode was using for methylene blue effluents at 664 nm wavelength while the florescent mode was used for the amine-modified latex beads at a 575 nm excitation and 610 nm emission wavelengths.

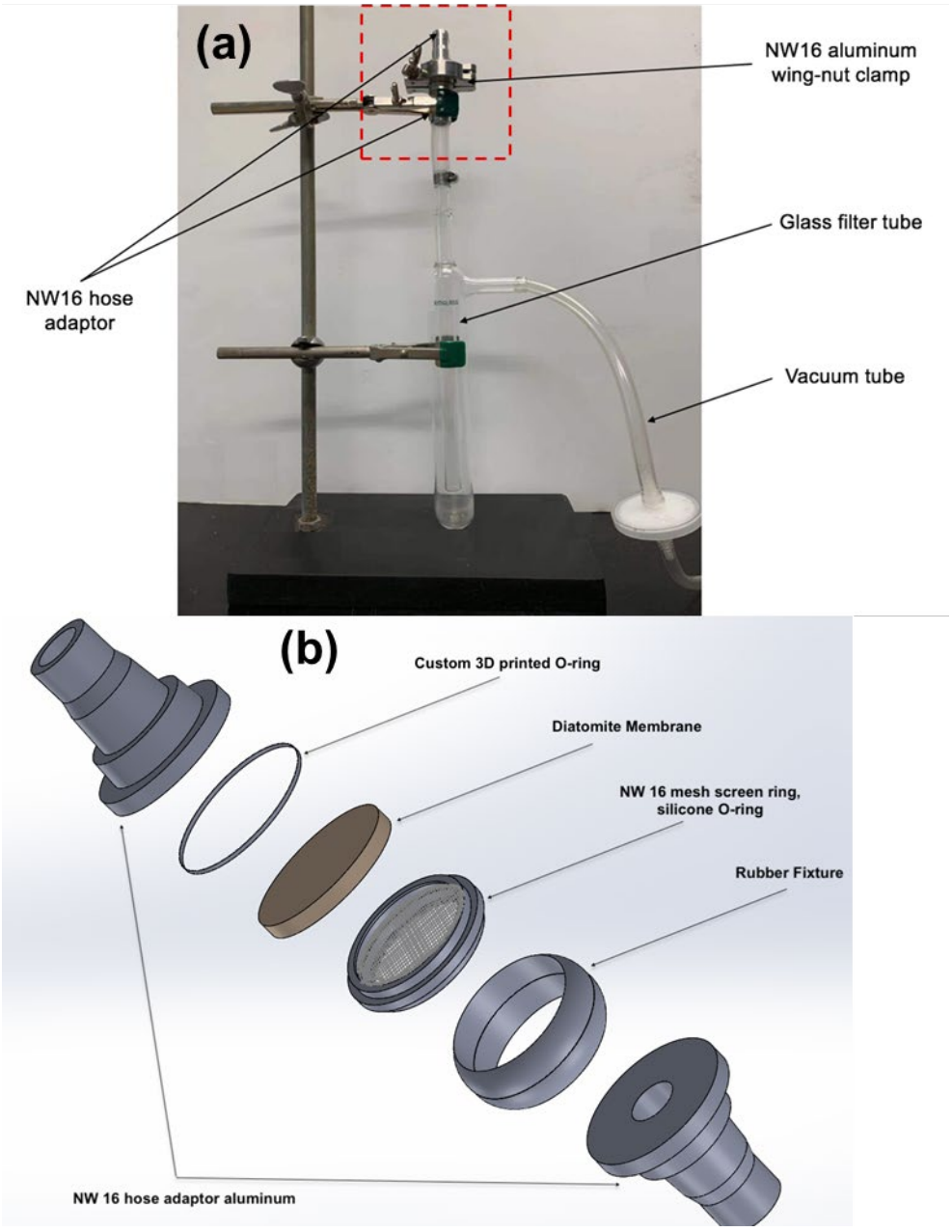

Figure 2.3: **(a)** Custom built vacuum filtration apparatus used to test the size selection and electrostatic adsorption filtration capabilities of the freeze cast diatomite membranes. **(b)** Vacuum parts (red box in **(a)**) were used to contain the diatomite membrane and a custom 3D printed O-ring was used to ensure the filtrate did not pass through the voids between vacuum housing and diatomite membrane.

2.4 Results and Discussion

2.4.1 Lamellar Structure

Micro-computed tomography was used to visualize the open porosity from the freeze casting process as shown in Figure 2.4. A key attribute observed was the translamellar bridging which significantly contributes to stress-delocalization and overall rigidity of the final scaffold. Research done by Frank et al. [77] demonstrated an increase in mechanical properties (i.e. stiffness and strength) the larger the constituent platelets were which is unexpected for sintered ceramics because smaller particles allow for more bonding to occur during the sintered step. However, translamellar bridging is more likely to occur with larger particles and is the cornerstone to obtaining a strong freeze caste scaffold. The diatomite powder consists of a distribution of sizes of diatoms and finer particles which are expected to each serve an important role. For example, the larger diatom frustules allow for a large number of inter-lamellar bridging to occur, while the finer particles help fill in the gaps of the larger diatoms to promote stronger jointing.

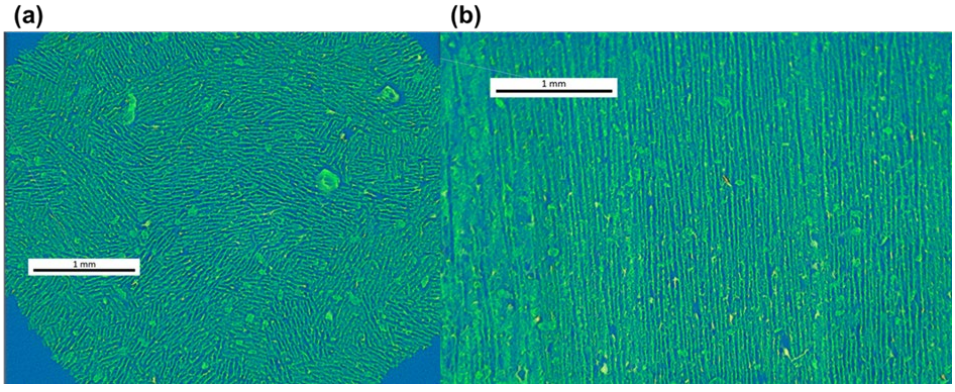

Figure 2.4: Micro-computed tomography images of diatomite membranes created from a freeze casting process. The top-down **(a)** and transverse **(b)** cross-sections (with respect to the lamellar walls that are common in unidirectionally freeze caste materials) are demonstrated. Lamellar walls are shown to be ~ 15 µm, are continuous, and have translamellar bridging that produce a combination of porosity and mechanical rigidity to undergo high-throughput flow applications.

2.4.2 Addition of $NaCO_3$

Due to the potential demonstrated by Chen et al. [78] for freeze caste diatomite membranes, we further explored how to optimize the membranes properties, specifically its mechanical properties. The membranes, without any further treatment, would crush without applying much pressure and would leave dust when applying scotch tape. These properties are clearly undesirable for a membrane used to filter out unwanted impurities and conflict with the desirable properties of the membranes, such as the efficient hierarchical porosity both from the freeze casting process (~15 μm lamellar walls) and the natural porosity of the diatom frustules. Therefore, changing the processing conditions were considered to further increase the stiffness and strength. We chose to include sodium carbonate ($NaCO_3$), a flux agent, to locally reduce the phase change activation energy of the amorphous silica to a crystalline phase (i.e., cristobalite), as shown in previous research on adding flux agent to diatomite for improving filtration capabilities [88, 89]. This was performed, as opposed to simply increasing the sintering temperature and soaking time, to save cost on energy and because the flux agent locally targets loose aggregates which increases permeability and avoids the issue of having dust remain on the surfaces of the sintered membrane. The trade-off that is expected with adding flux agents to diatomite is that, if too much is added then the natural porosity of the diatomite may be melted together. Therefore, finding the right amount of sodium carbonate that is needed to increase mechanical properties with minimal closure of the natural porosity of diatom frustules was a major goal in this research.

2.4.2.1 Effects on Porosity

Freeze casting of diatomite membranes was performed by varying the amount of sodium carbonate with 3, 5, 7, and 9 wt. % (will further be referred to as SC3, SC5, SC7, and SC9, respectively) in the initial ceramic loading of the freeze cast slurry. In other words, all membranes were created with 25 wt. % of ceramics (i.e., diatomite and sodium carbonate) in the initial slurry and of this 25 wt. % different proportions of sodium carbonate were used.

SEM was performed on the diatomite membranes after the sintering process, shown in Figure 2.5, and reveal, as expected, that the natural porosity of the diatom frustules begins to close with more sodium carbonate being added. However, both SC3 and SC5 membranes appear to have little effects on the closing of the frustule pores. Further SEM imaging was performed on the SC5 samples, shown in Figure 2.6, to both demonstrate the various levels of the hierarchical porosity the membranes possess and to also demonstrate that pores smaller than 100 nm appeared unaltered despite the presence of sodium carbonate during the high-temperature sintering process.

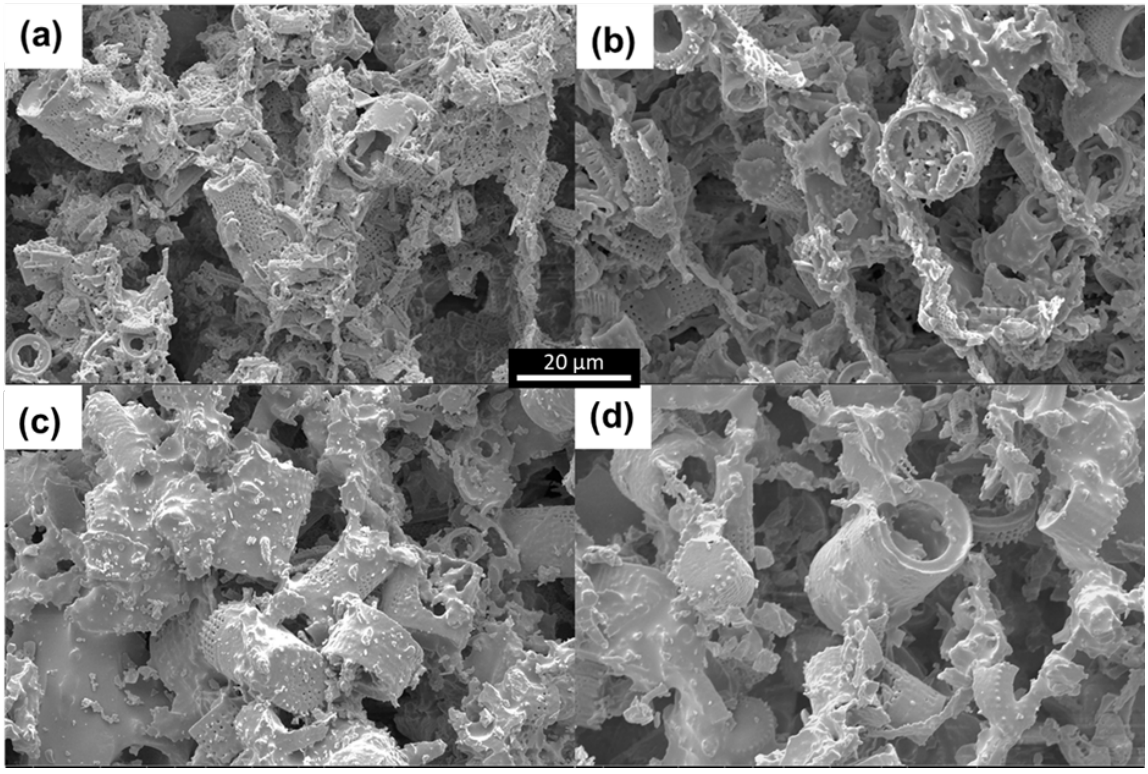

Figure 2.5: Scanning electron micrographs with varying magnifications of the freeze caste diatomite monoliths with varying sodium carbonate content: **(a)**, **(b)**, **(c)**, and **(d)** are 3, 5, 7, and 9 wt. %, respectively, after being sintered at 1050 C° for 3 hours. It is clear the texture of the diatom surfaces becomes smoother the more sodium carbonate content there is demonstrating a loss in surface area and porosity.

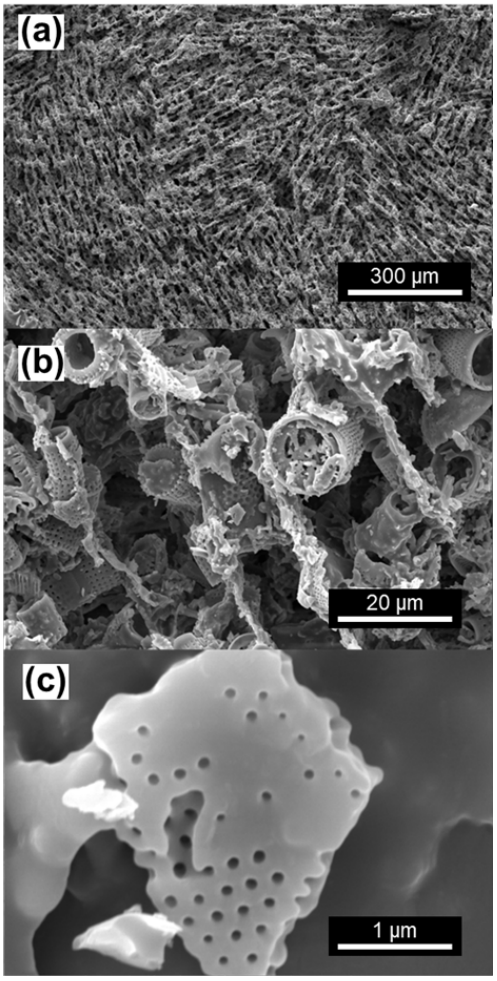

Figure 2.6: **.** Scanning electron micrographs with varying magnifications of the ice-templated diatomite monoliths with 5 wt. % sodium carbonate and sintered at 1050 C° for 3 hours. **(a)** and **(b)** demonstrate the lamellar porosity from ice-templating process and the natural porosity of the diatom frustules, respectively. **(c)** demonstrates the retention of pores ~ 100 nm despite thermal processing.

N_2 physisorption was performed on the raw diatomite used, as well as the sintered membranes with varying sodium carbonate (including no sodium carbonate content) to observe the change in specific surface area (SSA) expected from thermal treatment. The initial diatomite yielded a BET surface area of 38.15 ± .15 m^2/g with a total pore volume of 0.11 cc/g at saturation, while all of the sintered membranes showed negligible values.

This comes to no surprise, as this method of testing for porosity is in the range of 2 – 10 nm and pores with such low diameters are expected to sinter close under high-temperatures.

From SEM, it appeared that SC5 membranes had little effect on the porosity, while the SC7 membranes appeared to have a clear effect. Therefore, mercury porosimetry was performed to compare the hierarchical porosity across a broad range of pore size for the SC5 and SC7 membranes, as shown in Figure 2.7. Pore size distributions were obtained by measuring the volume of mercury intruded into the pores as a function of applied pressure using the Washburn equation:

$$r = -\frac{(2\gamma cos\theta)}{P} \tag{2.1}$$

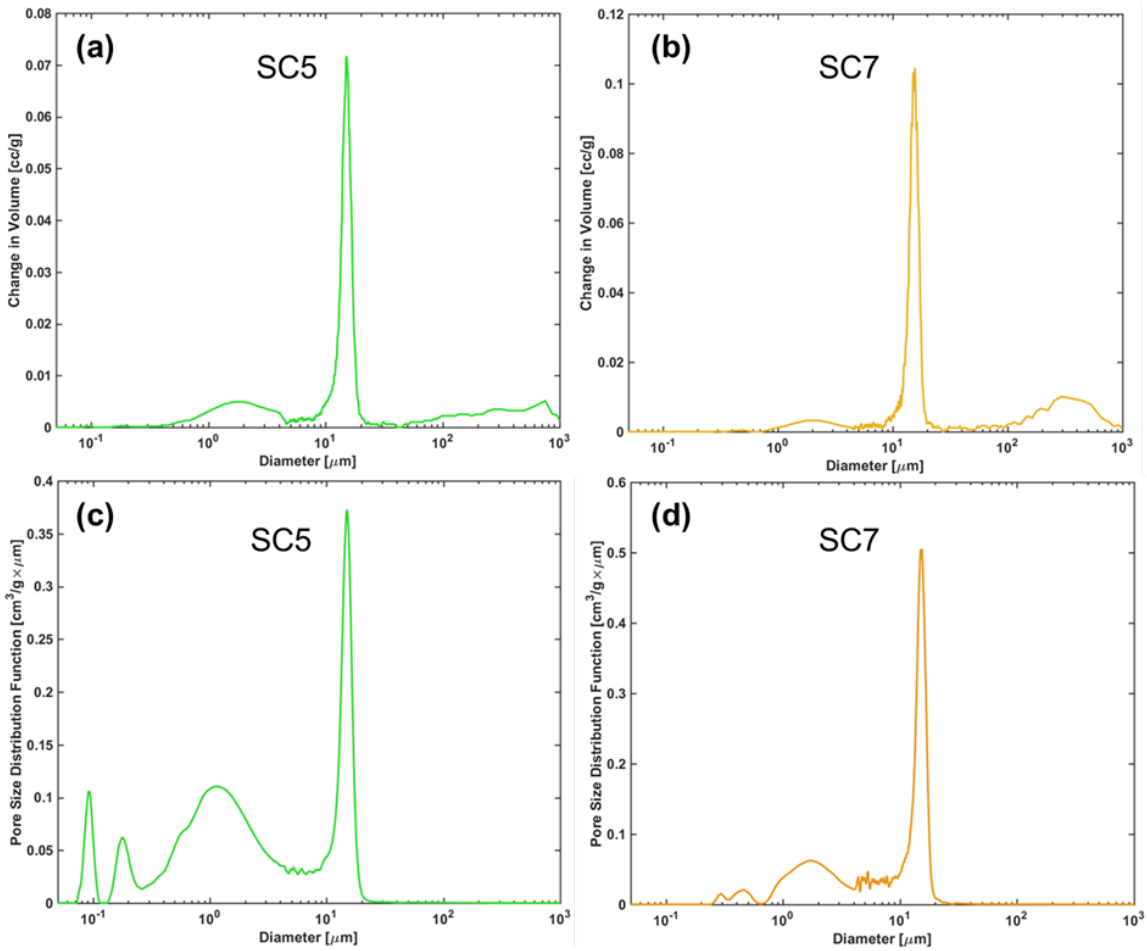

Figure 2.7: Mercury porosimetry analysis (down to 50 nm pore diameter) on diatomite membranes with a sodium carbonate content of either 5 wt. % (left) or 7 wt. % (right). **(a)** and **(b)** are the slopes of the incremental volume vs. pressure plots plotted again pore diameters and reveal most of the change in volume occurs due to the lamellar pores created from the freeze casting process. Bands are also observed in the 1 mm region which are likely due to the width of lamellar pores, while the band observed in the 1 μm range are due to the diatom's natural porosity. **(c)** and **(d)** are pore distribution plots that allow a closer look in the higher pressure (lower diameter) regions of the porosimetry results. There appears to be more porosity in sub-micron regions with the lower sodium carbonate content, as expected.

Where γ and θ are material constants of mercury and are the surface tension and contact angle, respectively [90]. Therefore, as pressure, P, is steadily increased, smaller pores (r = radius) are being filled with mercury. Volume of mercury intruded or cumulative volume, V, was also measured. Typically, cumulative volume is plotted against pressure or pore size, however this tends to lose information from multimodal porous materials due to

the largest band of pores dominating the cumulative volume. By obtaining *dV/dP* and plotting against pore size, we are able to observe the spread of pore sizes and how much each band of pores (i.e., lamellar walls from freeze casting processing, the various hierarchical levels of diatom porosity, and interparticle spacing) is contributing to the overall porosity as shown in Figure 2.7a,b. These plots demonstrate both SC5 and SC7 membranes have similar lamellar wall structures, as expected, from the large peaks around 15 μm. Both types of membranes also show a modest contribution of volume from pores in the diameter range of 1 – 2 μm which is likely from the largest pores seen on the diatom frustules. The pores sizes observed that are greater than 100 μm are likely due to the anisotropic geometry of the lamellar structure.

The *dV/dP* method of analysis gives more weight to larger pores (lower pressures); therefore, further analysis was done to give more weight to larger pressures by plotting the pore size distribution function, *Dv(r)*, against pore size:

$$Dv(r) = \frac{P}{r}\frac{dV}{dP} \tag{2.2}$$

By giving more weight to smaller pore sizes we are able to observe what we expected to occur by adding excess sodium carbonate. That is, that there should be less porosity observed for SC7 samples compared to SC5 which is shown by comparing Figure 2.7c and Figure 2.7d. The SC5 membranes have a narrow band of pores with diameters below 100 nm that are not seen with the SC7 samples which are likely from similar pores to the uniform pores observed in Figure 2.6c. Moreover, the ratio of volume contribution between the pore band around 2 μm and the steep band around 15 μm (representative of

the porous lamellar walls) appears greater for SC5 which suggests that these 2 μm pores are also being affected from adding in excess sodium carbonate. Overall, these porosimetry results corroborate the SEM results which suggest that adding more than 7 wt. % of sodium carbonate significantly closes the natural porosity of the diatomite.

2.4.2.2 Effects on Mechanical Properties

As mentioned previously, the trade-off we expect by adding in sodium carbonate is between porosity (favorable for filtration and further functionalization for other applications) and the mechanical properties (favorable for larger flow rates, handling, and a decrease in dust impurities from membrane itself). By quantifying both of these material properties we can: (i) map out what processing conditions are necessary for tailoring the membranes to their desired application and (ii) observe diminishing returns in mechanical properties with adding in sodium carbonate.

The effect that sodium carbonate has on the material properties of the diatomite membranes were initially observed by obtaining the shrinkage and bulk densities of the sintered membranes, as shown in Figure 2.8. The shrinkage of the membranes is obtained by measuring the diameters before and after sintering:

$$Shrinkage\ \% = 100(1 - \frac{D_{final}}{D_{initial}}) \tag{2.3}$$

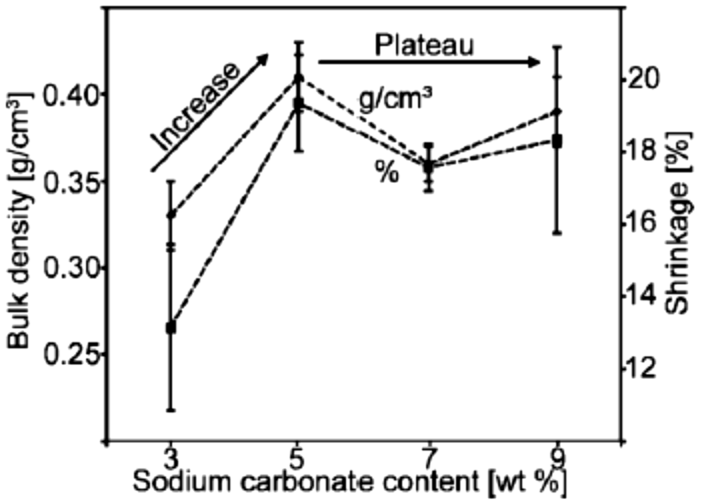

Figure 2.8: Bulk density of sintered diatomite scaffolds with varying sodium carbonate contents (3, 5, 7, and 9 wt %) and the shrinkage of their diameters [$1 - D_{final}/D_{initial}$] as a result of the sintering process. As expected, the bulk density and shrinkage seem to be in strong correlation. It appears that there is a noticeable increase in density with an increasing sodium carbonate content from 3 to 5%, but thereafter, the values plateau.

This was done as a simple way to quantify the effect increasing the sodium carbonate content has on the final product. Results demonstrate a clear correlation between shrinkage and bulk density, as expected. Moreover, these results reveal a noticeable increase in shrinkage and bulk density from 13.15 ± 2.29 % and 0.33 ± 0.02 g/cc to 19.36 ± 1.33 % and 0.41 ± 0.02 g/cc for SC3 and SC5 membranes, respectively. However, the addition of more sodium carbonate (i.e., SC7 and SC9) did not significantly further increase these measured variables and appeared to hit a plateau.

Mechanical compression results further reveal the effect sodium carbonate has on the sintered diatomite membranes, shown in Figure 2.9. Figure 2.9a demonstrates that adding in any amount of sodium carbonate significantly increases the mechanical properties (i.e. Young's Modulus and ultimate compressive strength) of the sintered membranes. Moreover, Figure 2.9a and 9b reveal a clear increase in these properties from SC3 to SC5 in the axial direction (compression axis aligned with lamellar walls), but

thereafter sample types begin to experience diminishing returns with increase sodium carbonate content. A surprising decrease in Young's Modulus is also observed in the axial direction from SC7 to SC9 which suggests finding an optimum region of sodium carbonate that considers both mechanical properties and maintaining the natural porosity of the diatomite is between 3 and 7 wt. %. Lastly, the compression results in the transverse direction show a peak in mechanical properties for SC5 membranes. This suggests there may be competing mechanisms that contribute to the mechanical properties, with the obvious one being the sodium carbonate reducing the activation energy of crystallization during sintering. The second may be due to a decrease in lamellar bridging which is a critical determinate in the mechanical properties of freeze-caste scaffolds [76, 77]. An increase in sodium carbonate also means a decrease in diatomite per volume of the final membranes due to the overall amount of ceramics added into the initial slurries being held constant. A decrease in diatomite density will result in a particle size distribution that is proportional, and due to larger particles increasing the probability of lamellar bridging to occur, this would explain how adding too much sodium carbonate could result in a decrease in the mechanical properties.

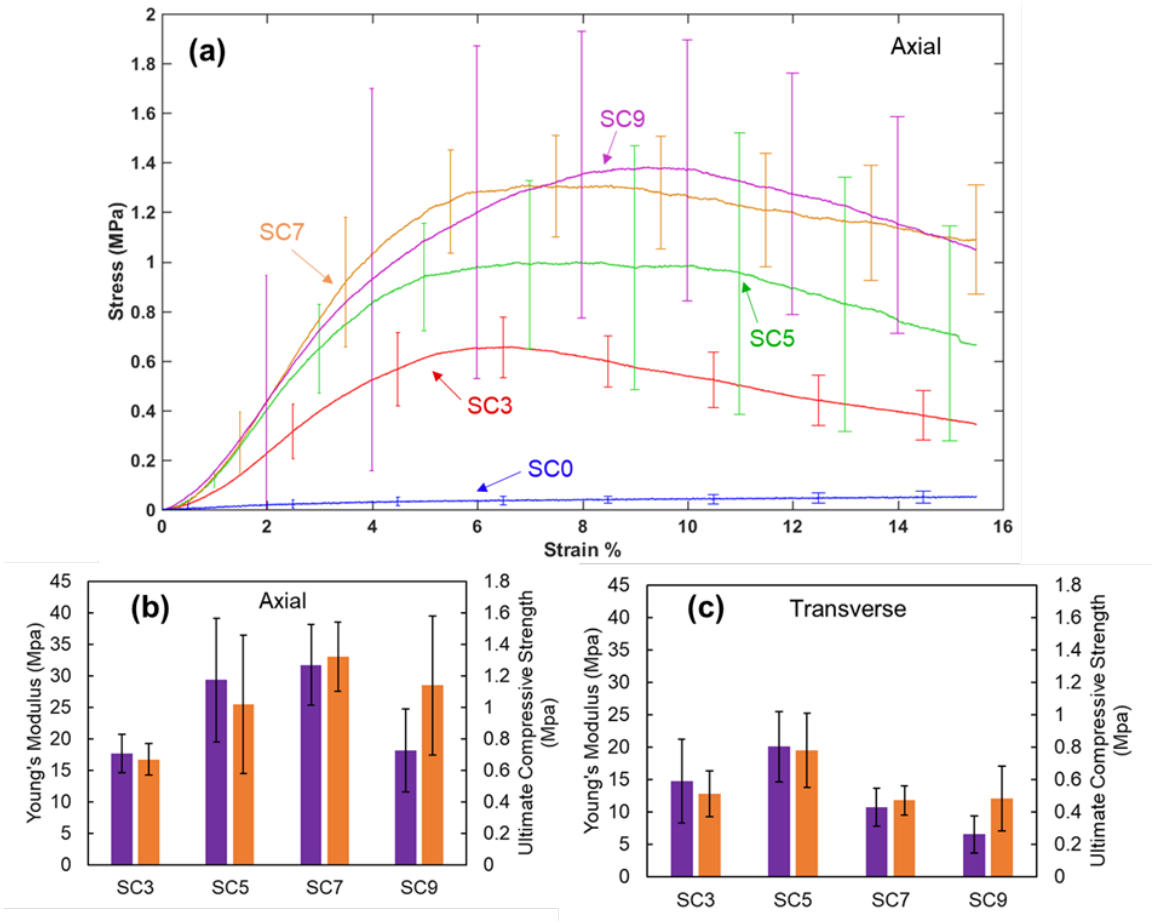

Figure 2.9: Summary of compressive mechanical properties of diatomite membranes with varying sodium carbonate content (i.e. 0, 3, 5, 7, and 9 wt. %). **(a**) Axial stress-strain plots demonstrating a significant increase in mechanical properties due to the addition of sodium carbonate, however the trend of increasing stiffness and strength appears to quench after 7 wt. %; **(b)** summarizes the axial properties of the membranes (i.e. axis the lamellar walls are aligned in) and demonstrate a noticeable jump in Young's Modulus after 3 wt. %, but otherwise do not demonstrate a linear trend of increasing mechanical properties with sodium carbonate content; **(c)** summarizes the transverse properties which are noticeably weaker than the axial direction, as expected.

2.4.3 Compositional Analysis

X-ray diffraction (XRD) and Fourier-Transform Infrared (FTIR) analyses were performed on each type of membranes to observe the compositional effect sodium carbonate has on the crystallization of the diatomite silica, shown in Figure 2.10. From the change in color with increasing sodium carbonate (Figure 2.10a), it is clear there is a compositional change that warranted further investigation. Previous literature that uses

sodium carbonate as a flux agent for diatomite demonstrate an increase in cristobalite content that is correlated with how white the sintered byproducts become [88]. Therefore, we expected to observe increasing crystallization content in XRD and FTIR with more sodium carbonate content, specifically of the cristobalite phase. However, XRD results (Figure 2.10b and 2.10c) revealed that all samples achieve significant crystallization due to large and narrows peaks. All samples, including SC0, contain peaks that resemble crystalline silica of the cristobalite phase (JCPDS#39-1425), with the most noticeable peaks being for the '101', '200', and '102' planes. Upon closer inspection of the '101' plane we can clearly observe the effect sodium carbonate has on the crystal structure of the crystallized diatomite. With increasing sodium carbonate content, the '101' peak decreases in intensity and is shifted to a higher angle. Important to note, is that all sample's '101' peaks are ~ 0.3 2θ less than the reference for the '101' cristobalite peak. Therefore, a decrease in the angle of the '101' peaks with decreasing sodium carbonate suggests that the aluminum and magnesium impurities, quantified through energy dispersive spectroscopy, may be causing substitutional and/or interstitial defects, thereby producing lattice strains on what is mainly a cristobalite crystal lattice. Furthermore, increasing sodium carbonate content may be decreasing the number of defects responsible for decreasing the lattice parameter compared to the cristobalite reference by further lowering the energy barrier needed for crystallization of pure cristobalite despite the entropically favorable defects due to impurities present.

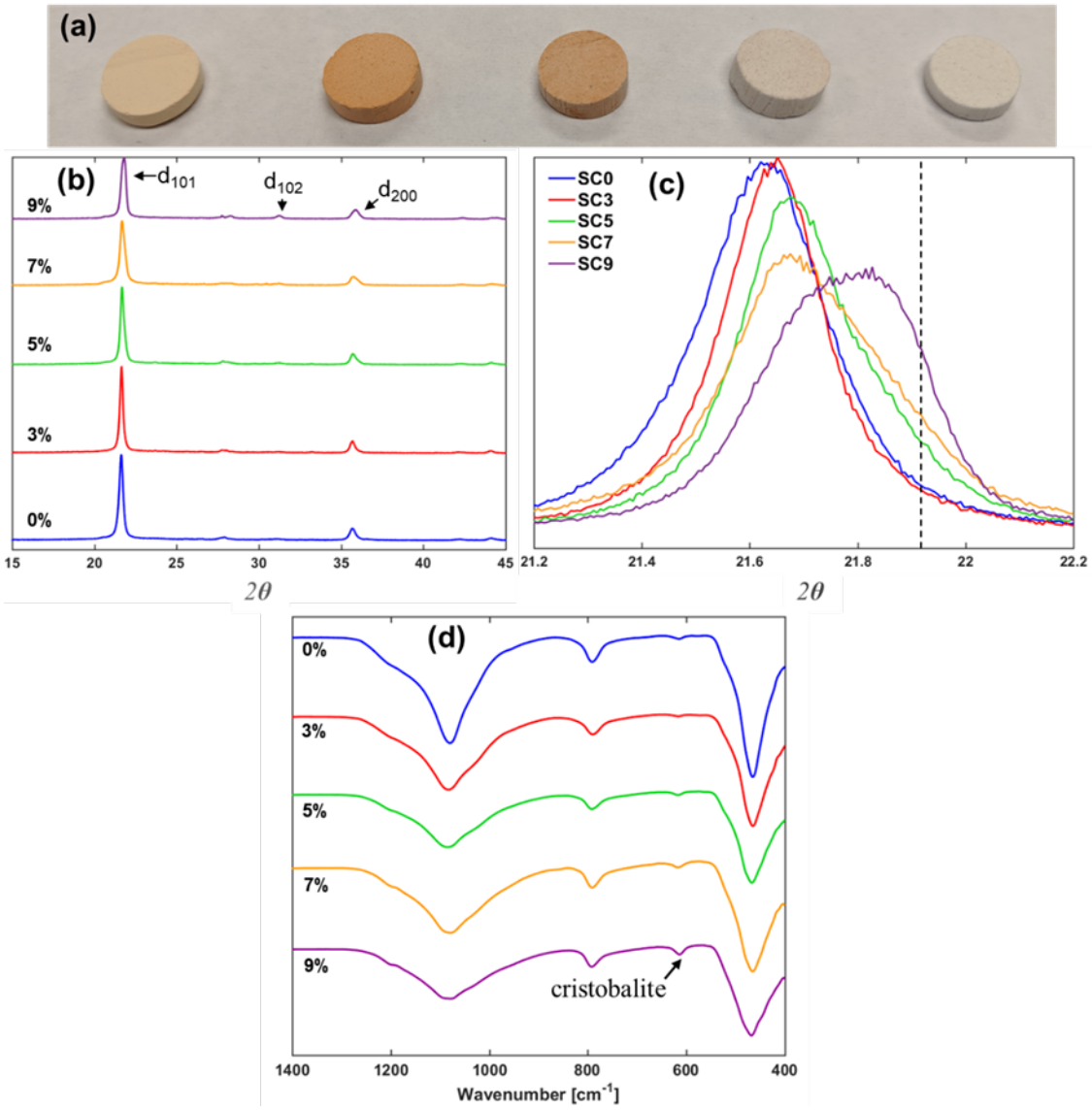

Figure 2.10: Images of the sintered diatomite membranes with varying sodium carbonate (left to right: 0, 3, 5, 7, and 9 sodium carbonate wt. %) that demonstrate a change to an orange color with a subsequent gradual whitening as more sodium carbonate content is used. **(b)** and **(c)** are x-ray diffraction spectra of the diatomite membranes. **(b)** demonstrates that all types of the membranes obtained crystallization to a cristobalite phase as demonstrated by the d_{101} and d_{200} peaks present on all the spectra. However, with 9 wt. % sodium carbonate the d_{102} plane of cristobalite becomes more pronounced than for membranes with less sodium carbonate. Furthermore, **(c)** is a closer look at the d_{101} peak of cristobalite and demonstrates the peak intensity decreases and is shifted to a larger angle (smaller lattice parameter) that is closer to crystalline cristobalite (JCPDS#39-1425) that is denoted by the dotted vertical line. **(d)** is Fourier-transform infrared spectroscopy and reveals all membranes have noticeable bands at 1095, 792, and 475 cm^{-1} which are representative of the asymmetric stretching, symmetric stretching and bending vibrations of Si-O-Si bonds, respectively [40]. However, the 617 cm^{-1} band is assumed to be representative of the cristobalite phase which becomes more pronounced as more sodium carbonate is added (black circle).

2.4.4 Filtration Results

2.4.4.1 Electrostatic Adsorption

Diatomite is naturally anionic on its surface and therefore a cationic dye, methylene blue, was used to observe the effectiveness the diatomite, freeze-caste membranes have for electrostatic adsorption during in-line vacuum-assisted flow, shown in Figure 2.11. The retention of methylene blue (mg of methylene blue retained per g of membrane) was 0.129 ± 0.027, 0.169 ± 0.037, and 0.191 ± 0.049 mg/g for SC5, SC7, and SC9 membranes, respectively, for an initial concentration of 100 mg/g of methylene blue dye. These results show a proportional relationship between sodium carbonate content and adsorption of methylene blue dye; however, error bars are overlapping which suggest the changes are negligible. Regardless, this trend is surprising given that an increase in sodium carbonate causes the porosity to decrease due to surface melting. This trend is likely due to changes in the surface chemistry and the membrane's electrostatic surface potential due to the effect sodium carbonate has in aiding the crystallization of amorphous diatomite silica into cristobalite.

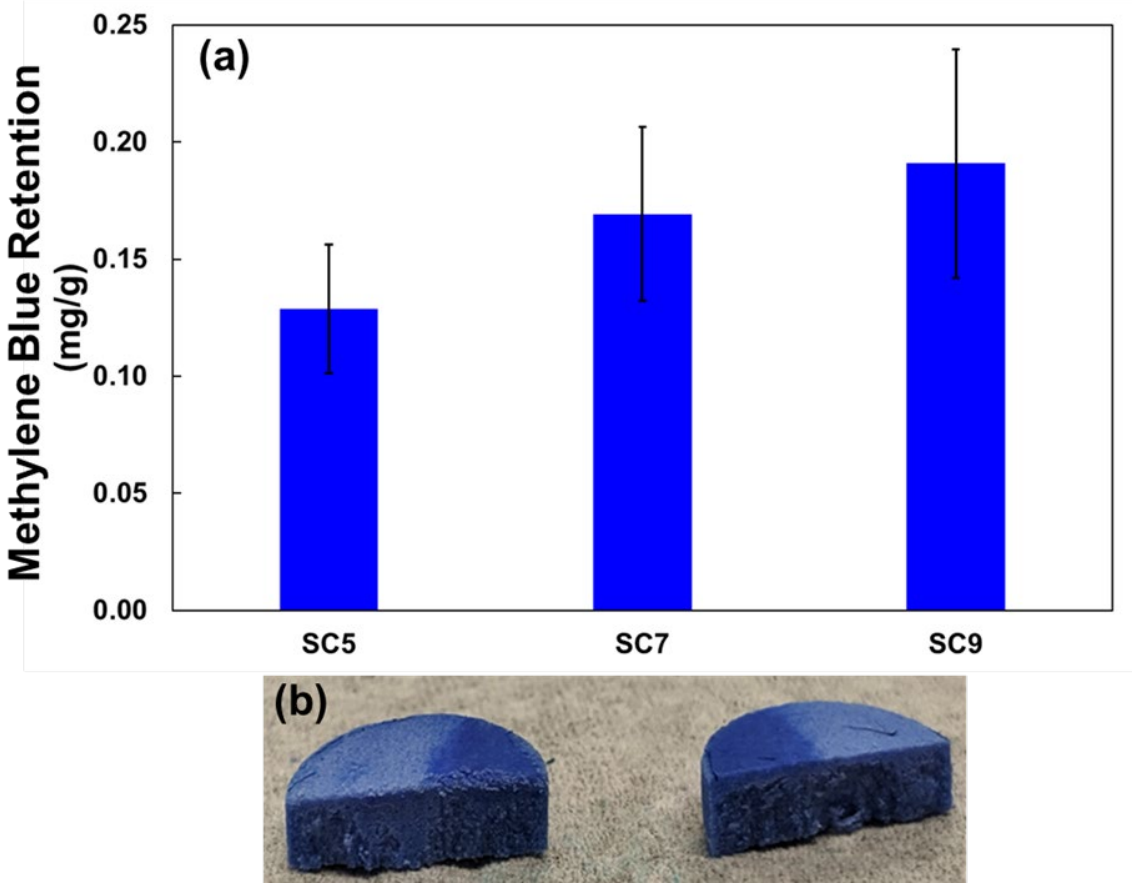

Figure 2.11: **(a)** Electrostatic adsorption filtration results of 100 mg/L methylene blue aqueous solution through 3 – 4 mm thick diatomite membranes with varying sodium carbonate content (5, 7, and 9 wt. %). Values were quantified using spectrophotometry before and after filtration. Results demonstrate a slight increase in adsorption capabilities with increased sodium carbonate content, however the increase is negligible as the error bars are overlapping. **(b)** Image captured right after filtration demonstrating a thorough adsorption of the dye despite the low contact time due to rapid vacuum assisted flow.

Figure 2.11b shows a cross-section of the diatomite membranes after undergoing filtration and reveals a homogenous adsorption of methylene blue dye throughout the membrane. These results demonstrate the robustness of the membranes to undergo vacuum-assisted flow and an ability to quickly electrostatically adsorb methylene blue dye which show promise for future applications. However, further research will be needed to properly quantify the ability and capacity of these membranes for the use in electrostatic filtration.

2.4.4.2 Size Selection

It is essential for filtration membranes to have size selective properties to quickly remove the bulk of impurities of various sizes, while the adsorption capabilities in the previous section are complimentary to remove dissolved/ionic molecules and nano-impurities. Therefore, monodisperse 1 μm latex beads were used to observe the diatom membranes size-selective properties. Monodisperse latex beads are commonly used to quantify filtration efficiency due to their similar size to bacteria [91]. It is important to note that the diatomite membrane is mainly composed of 15 μm lamellar walls that provide continuous channels for the filtrate to pass through and therefore it is likely the latex beads pass straight through the membrane. Figure 2.12 shows a surprising retention of 38.8 ± 2.4, 41.3 ± 6.4, and 26.3 ± 6.2 % for the SC5, SC7, and SC9 membranes, respectively. Where retention is defined as:

$$Retention\ \% = 100(1 - \frac{C_{final}}{C_{initial}}) \tag{2.4}$$

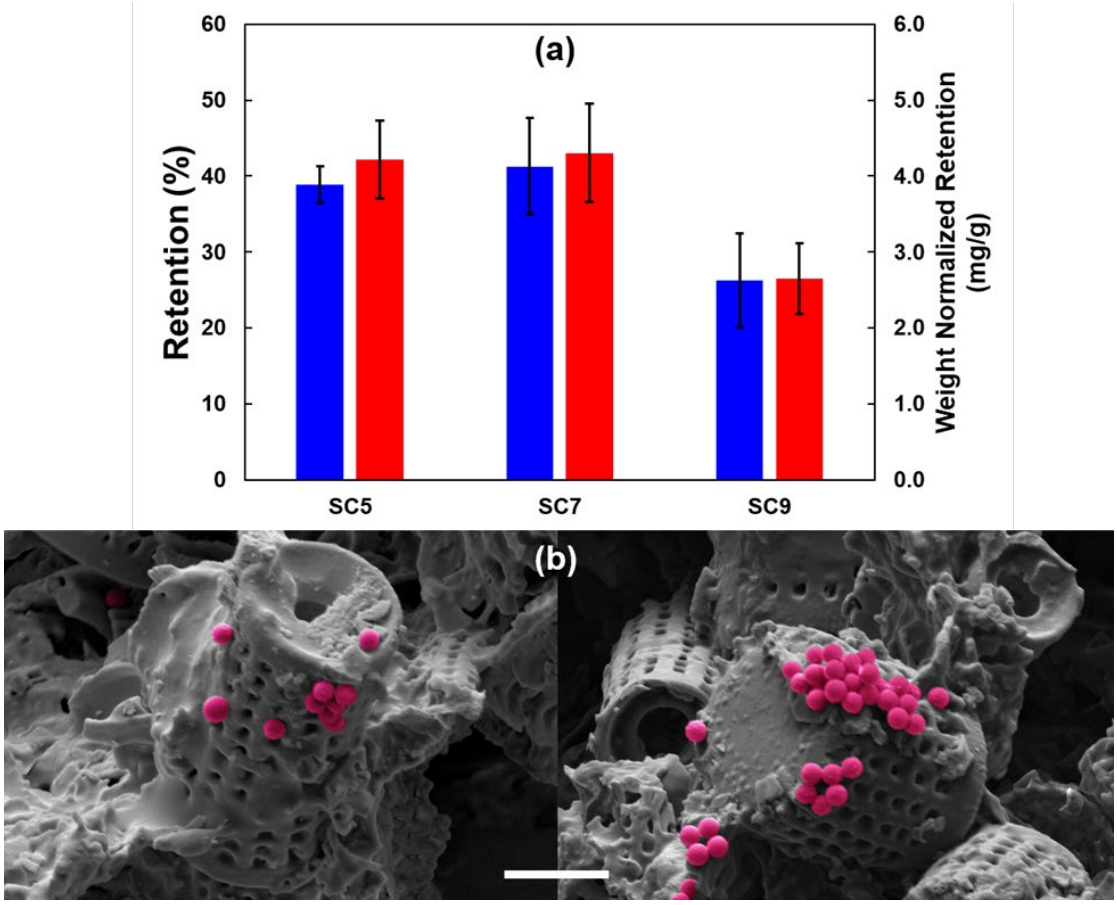

Figure 2.12: **(a)** Size selection filtration results of monodisperse 1-µm florescent latex beads through 3 – 4 mm thick diatomite membranes with varying sodium carbonate (5, 7, and 9 wt. %). Values were quantified using spectrophotometry before and after filtration. **(b)** are scanning electron micrographs that reveal the latex beads commonly become trapped onto the diatom frustule's natural porosity. The phenomenon likely occurs due to the open porosity of the frustules allowing the vacuum forces to permeate during filtration, thereby forcibly entrapping the particles. This mechanism likely explains why the retention of latex beads is around 40% despite the membranes have open lamellar walls ~ 15x larger than the diameter of the beads. Scale bar is 5 µm. Latex beads are artificially colored.

With C_{final} and $C_{initial}$ being the concentrations of latex beads before and after filtration, respectively. Figure 2.12b shows an SEM micrograph of an SC5 membrane after filtration and reveals how the latex beads aggregate on the uniform porosity of the walls in the diatom frustules. This may be a consequence of the open porosity of the diatoms allowing for efficient mass-transfer of the pressurized flow to force the beads into place during the filtration process. Furthermore, a clear drop in retention of beads for the SC9

samples can be explained due to the closure of these uniform pores, seen in SEM, responsible for partially enveloping and stabilizing the beads. A negligible difference between the SC5 and SC7 retention of beads can similarly be explained as the uniform pores (~ 800 nm) did not experience complete closure as observed through mercury porosimetry and SEM.

2.5 Conclusions

In this work, diatomite monoliths were produced through a freeze casting process, first performed by Chen et al. [78], and further reinforced by adding a flux agent (i.e., sodium carbonate) at various concentrations in the initial slurry. Imaging through SEM and μ-CT reveals that the freeze casting process provides an open network of lamellar porosity, reinforced through bridging, which compliments the naturally open porosity of the constituent diatom frustules. Using these hierarchically porous silica monoliths with efficient mass transport capabilities has the potential to be functionalized (i.e., metal-organic frameworks, zeolites, nanoparticles, and shape-preserving chemical alterations) for use in a plethora of applications, which are already being explored for both freeze casting and diatom nanotechnology, independently [51, 58, 69, 74, 81-87]. However, a key issue that has been solved in this work, through the addition of sodium carbonate, is to ensure the mechanical rigidity of these highly porous scaffolds. However, it was hypothesized and demonstrated that adding too much sodium carbonate results in surface melting of the natural porosity of the diatomite which would hinder future applications. We determined the optimal sodium carbonate in the initial slurry is 5 wt. % of the total ceramics used (sample SC5) due to achieving sufficient mechanical properties while maintaining porosity

below 100 nm. The bulk density, Young's modulus, and ultimate compressive strength of SC5 samples are 0.41 ± 0.02 g/cc, 29.37 ± 9.80 MPa, and 1.02 ± 0.44 MPa, respectively. To the best of our knowledge, seldom work has been performed to create highly porous diatomite monoliths, but of those referenced, the results here are similar (i.e., comparing bulk density and compressive strength), although the microstructures are completely different. The lamellar-wall microstructure is highly anisotropic which can potentially be taken advantage of in applications involving in-line flow (i.e., filtration, catalysis, sensing) due to the direction of maximum reinforcement being parallel with the forces of pressurized flow. Therefore, these diatomite membranes were tested under in-line vacuum filtration using methylene blue dye and 1 μm monodisperse latex beads to quantify the performance through electrostatic and size-selection capabilities, respectively. Results demonstrate potential for these membranes, under further functionalization, to be able to undergo high flow-rate applications which benefit from efficient mass-transfer and size-selection capabilities spanning several length scales.

2.6 Acknowledgements

Chapter 2, in part, is published as "Mechanical Optimization of Diatomite Monoliths from Freeze Casting for High-Throughput Applications" ACS Applied Bio Materials 2020 3 (7), 4444-4453. This work was coauthored by Z. Li, D. Lee, O. A. Graeve, D. D. Deheyn, and J. M. McKittrick. The dissertation author is the first author of this work. This work was performed in part at the San Diego Nanotechnology Infrastructure (SDNI) of UCSD, a member of the National Nanotechnology Coordinated Infrastructure, which is supported by the National Science Foundation (Grant ECCS-1542148). We acknowledge

Jessica Moreton, Dr. Brian Pimentel and Prof. Seth M. Cohen (Dept. of Chemistry & Biochemistry, UCSD) for assistance with gas sorption experiments. We acknowledge Dr. Ekaterina Novitskaya and Prof. Olivia Graeve (Dept. of Mechanical Aerospace Engineering, UCSD) for assistance with X-ray diffractions experiments.

2.7 References

[50] V. Gitis and G. Rothenberg, Ceramic Membranes: New Opportunities and Practical Applications. Boschstr. 12, 69469 Weinheim, Germany: Wiley-VCH, 2016.

[51] R. Ragni, S. R. Cicco, D. Vona, and G. M. Farinola, "Multiple Routes to Smart Nanostructured Materials from Diatom Microalgae: A Chemical Perspective," Advanced Materials, vol. 30, no. 19, May 2018, Art no. 1704289, doi: 10.1002/adma.201704289.

[52] M. Sumper and E. Brunner, "Learning from diatoms: Nature's tools for the production of nanostructured silica," Advanced Functional Materials, vol. 16, no. 1, pp. 17-26, Jan 2006, doi: 10.1002/adfm.200500616.

[53] H. Hadjar, B. Hamdi, M. Jaber, J. Brendlé, Z. Kessaïssia, H. Balard, J.B. Donnet, "Elaboration and characterisation of new mesoporous materials from diatomite and charcoal," Microporous and Mesoporous Materials, vol. 107, no. 3, pp. 219-226, Jan 2008, doi: 10.1016/j.micromeso.2007.01.053.

[54] B. H. Jo, C. S. Kim, Y. K. Jo, H. Cheong, and H. J. Cha, "Recent developments and applications of bioinspired silicification," Korean Journal of Chemical Engineering, vol. 33, no. 4, pp. 1125-1133, Apr 2016, doi: 10.1007/s11814-016-0003-z.

[55] M. Thakkar, Z. Q. Wu, L. P. Wei, and S. Mitra, "Water defluoridation using a nanostructured diatom-ZrO2 composite synthesized from algal Biomass," Journal of Colloid and Interface Science, vol. 450, pp. 239-245, Jul 2015, doi: 10.1016/j.jcis.2015.03.017.

[56] J. C. Qian, Z. G. Chen, C. B. Liu, F. Wang, Y. Z. Zhang, and M. M. Wang, "Biotemplated fabrication of hierarchical mesoporous CeO2 derived from diatom and its application for catalytic oxidation of CO," Chinese Science Bulletin, vol. 59, no. 26, pp. 3260-3265, Sep 2014, doi: 10.1007/s11434-014-0306-6.

[57] I. Rea, M. Terracciano, and L. De Stefano, "Synthetic vs Natural: Diatoms Bioderived Porous Materials for the Next Generation of Healthcare Nanodevices," Advanced Healthcare Materials, vol. 6, no. 3, Feb 2017, Art no. 1601125, doi: 10.1002/adhm.201601125.

[58] A. S. Miron, A. C. Gomez, F. G. Camacho, E. M. Grima, and Y. Chisti, "Comparative evaluation of compact photobioreactors for large-scale monoculture of microalgae," (in English), Journal of Biotechnology, Article; Proceedings Paper vol. 70, no. 1-3, pp. 249-270, Apr 1999.

[59] E Virginia Armbrust [1], John A Berges, Chris Bowler, Beverley R Green, Diego Martinez, Nicholas H Putnam, Shiguo Zhou, Andrew E Allen, Kirk E Apt, Michael Bechner, Mark A Brzezinski, Balbir K Chaal, Anthony Chiovitti, Aubrey K Davis, Mark

S Demarest, J Chris Detter, Tijana Glavina, David Goodstein, Masood Z Hadi, Uffe Hellsten, Mark Hildebrand, Bethany D Jenkins, Jerzy Jurka, Vladimir V Kapitonov, Nils Kröger, Winnie W Y Lau, Todd W Lane, Frank W Larimer, J Casey Lippmeier, Susan Lucas, Mónica Medina, Anton Montsant, Miroslav Obornik, Micaela Schnitzler Parker, Brian Palenik, Gregory J Pazour, Paul M Richardson, Tatiana A Rynearson, Mak A Saito, David C Schwartz, Kimberlee Thamatrakoln, Klaus Valentin, Assaf Vardi, Frances P Wilkerson, Daniel S Rokhsar., "The genome of the diatom Thalassiosira pseudonana: Ecology, evolution, and metabolism," (in English), Science, Article vol. 306, no. 5693, pp. 79-86, Oct 2004, doi: 10.1126/science.1101156.

[60] Artem A. Trofimov, Alison A. Pawlicki, Nikolay Borodinov, Shovon Mandal, Teresa J. Mathews, Mark Hildebrand, Maxim A. Ziatdinov, Katherine A. Hausladen, Paulina K. Urbanowicz, Chad A. Steed, Anton V. Ievlev, Alex Belianinov, Joshua K. Michener, Rama Vasudevan, and Olga S. Ovchinnikova, "Deep data analytics for genetic engineering of diatoms linking genotype to phenotype via machine learning," (in English), Npj Computational Materials, Article vol. 5, p. 8, Jun 2019, Art no. 4, doi: 10.1038/s41524-019-0202-3.

[61] Y. Liu, W. Y. Zhu, K. Guan, C. Peng, and J. Q. Wu, "Freeze-casting of alumina ultra-filtration membranes with good performance for anionic dye separation," Ceramics International, vol. 44, no. 10, pp. 11901-11904, Jul 2018, doi: 10.1016/j.ceramint.2018.03.160.

[62] R. W. McIndoe, "DIATOMACEOUS EARTH FILTRATION FOR WATER SUPPLIES .1," (in English), Water & Wastes Engineering, Article vol. 6, no. 10, pp. 50-&, 1969.

[63] B. Michen, A. Diatta, J. Fritsch, C. Aneziris, and T. Graule, "Removal of colloidal particles in ceramic depth filters based on diatomaceous earth," (in English), Separation and Purification Technology, Article vol. 81, no. 1, pp. 77-87, Sep 2011, doi: 10.1016/j.seppur.2011.07.006.

[64] B. Michen, F. Meder, A. Rust, J. Fritsch, C. Aneziris, and T. Graule, "Virus Removal in Ceramic Depth Filters Based on Diatomaceous Earth," (in English), Environmental Science & Technology, Article vol. 46, no. 2, pp. 1170-1177, Jan 2012, doi: 10.1021/es2030565.

[65] M. Wegmann, B. Michen, and T. Graule, "Nanostructured surface modification of microporous ceramics for efficient virus filtration," (in English), Journal of the European Ceramic Society, Article vol. 28, no. 8, pp. 1603-1612, 2008, doi: 10.1016/j.jeurceramsoc.2007.11.002.

[66] M. A. Al-Ghouti, M. A. M. Khraisheh, S. J. Allen, and M. N. Ahmad, "The removal of dyes from textile wastewater: a study of the physical characteristics and adsorption

mechanisms of diatomaceous earth," (in English), Journal of Environmental Management, Article vol. 69, no. 3, pp. 229-238, Nov 2003, doi: 10.1016/j.jenvman.2003.09.005.

[67] W. T. Tsai, K. J. Hsien, and J. M. Yang, "Silica adsorbent prepared from spent diatomaceous earth and its application to removal of dye from aqueous solution," Journal of Colloid and Interface Science, vol. 275, no. 2, pp. 428-433, Jul 2004, doi: 10.1016/j.jcis.2004.02.093.

[68] A. A. Reka, B. Pavlovski, and P. Makreski, "New optimized method for low-temperature hydrothermal production of porous ceramics using diatomaceous earth," (in English), Ceramics International, Article vol. 43, no. 15, pp. 12572-12578, Oct 2017, doi: 10.1016/j.ceramint.2017.06.132.

[69] Yubao Bi, Lei Han, Yangfan Zheng, Yunpeng Guan, Haijun Zhang*, Shengtao Ge, Huifang Wang, Quanli Jia, Yuxin Zhang, and Shaowei Zhang, "Lotus-Seedpod-Bioinspired 3D Superhydrophobic Diatomite Porous Ceramics Comodified by Graphene and Carbon Nanobelts," Acs Applied Materials & Interfaces, vol. 10, no. 32, pp. 27416-27423, Aug 2018, doi: 10.1021/acsami.8b05878.

[70] L. Han, F. L. Li, X. G. Deng, J. K. Wang, H. J. Zhang, and S. W. Zhang, "Foam-gelcasting preparation, microstructure and thermal insulation performance of porous diatomite ceramics with hierarchical pore structures," Journal of the European Ceramic Society, vol. 37, no. 7, pp. 2717-2725, Jul 2017, doi: 10.1016/j.jeurceramsoc.2017.02.032.

[71] F. Akhtar, P. O. Vasiliev, and L. Bergstrom, "Hierarchically Porous Ceramics from Diatomite Powders by Pulsed Current Processing," Journal of the American Ceramic Society, vol. 92, no. 2, pp. 338-343, Feb 2009, doi: 10.1111/j.1551-2916.2008.02882.x.

[72] Aleksandra Šaponjić, Miroslav Stanković, Jelena Majstorović, Branko Matović, Svetlana Ilić, Adela Egelja, Maja Kokunešoski, "Porous ceramic monoliths based on diatomite," (in English), Ceramics International, Article vol. 41, no. 8, pp. 9745-9752, Sep 2015, doi: 10.1016/j.ceramint.2015.04.046.

[73] W. N. Shen, L. J. Feng, A. Lei, and M. J. Guo, "Preparation and characterization of diatomite-based porous ceramics," Patent 1-3, 2012. [Online]. Available: <Go to ISI>://WOS:000319169600182

[74] W. W. Yuan, P. Yuan, D. Liu, W. B. Yu, L. L. Deng, and F. R. Chen, "Novel hierarchically porous nanocomposites of diatomite-based ceramic monoliths coated with silicalite-1 nanoparticles for benzene adsorption," (in English), Microporous and Mesoporous Materials, Article vol. 206, pp. 184-193, Apr 2015, doi: 10.1016/j.micromeso.2014.12.004.

[75] S. Deville, "The lure of ice-templating: Recent trends and opportunities for porous materials," (in English), Scripta Materialia, Article vol. 147, pp. 119-124, Apr 2018, doi: 10.1016/j.scriptamat.2017.06.020.

[76] S. Deville, "Freezing Colloids: Observations, Principles, Control, and Use Applications in Materials Science, Life Science, Earth Science, Food Science, and Engineering Preface," in Freezing Colloids: Observations, Principles, Control, and Use: Applications in Materials Science, Life Science, Earth Science, Food Science, and Engineering, (Engineering Materials and Processes. Cham: Springer International Publishing Ag, 2017, pp. VII-IX.

[77] Michael B. Frank, Steven E. Naleway, Tsuk Haroush, Chin-Hung Liu, Sze Hei Siu, Jerry Ng, Ivan Torres, Ali Ismail, Keyur Karandikar, Michael M. Porter, Olivia A. Graeve, Joanna McKittrick, "Stiff, porous scaffolds from magnetized alumina particles aligned by magnetic freeze casting," (in English), Materials Science & Engineering C-Materials for Biological Applications, Article vol. 77, pp. 484-492, Aug 2017, doi: 10.1016/j.msec.2017.03.246.

[78] Y. H. Lo, C. Y. Yang, H. K. Chang, W. C. Hung, and P. Y. Chen, "Bioinspired Diatomite Membrane with Selective Superwettability for Oil/Water Separation," (in English), Scientific Reports, Article vol. 7, p. 11, May 2017, Art no. 1426, doi: 10.1038/s41598-017-01642-2.

[79] R. P. Liu, J. Yuan, and C. A. Wang, "A novel way to fabricate tubular porous mullite membrane supports by TBA-based freezing casting method," Journal of the European Ceramic Society, vol. 33, no. 15-16, pp. 3249-3256, Dec 2013, doi: 10.1016/j.jeurceramsoc.2013.06.005.

[80] Jae-Young Jung, Steven E. Naleway, Yajur N. Maker, Kathryn Y. Kang, Jaehong Lee, Jungmin Ha, Sung Sik Hur*, Shu Chien, and Joanna McKittrick, "3D Printed Templating of Extrinsic Freeze-Casting for Macro-Microporous Biomaterials," (in English), Acs Biomaterials Science & Engineering, Article vol. 5, no. 5, pp. 2122-2133, May 2019, doi: 10.1021/acsbiomaterials.8b01308.

[81] Wenbin Yu, Peng Yuan, Dong Liu, Liangliang Deng, Weiwei Yuan, Bo Tao, Hefa Cheng, Fanrong Chen, "Facile preparation of hierarchically porous diatomite/MFI-type zeolite composites and their performance of benzene adsorption: The effects of NaOH etching pretreatment," (in English), Journal of Hazardous Materials, Article vol. 285, pp. 173-181, Mar 2015, doi: 10.1016/j.jhazmat.2014.11.034.

[82 Zhihao Bao, Michael R. Weatherspoon, Samuel Shian, Ye Cai, Phillip D. Graham, Shawn M. Allan, Gul Ahmad, Matthew B. Dickerson, Benjamin C. Church, Zhitao Kang, Harry W. Abernathy III, Christopher J. Summers, Meilin Liu, and Kenneth H. Sandhage, "Chemical reduction of three-dimensional silica micro-assemblies into microporous silicon

replicas," (in English), Nature, Article vol. 446, no. 7132, pp. 172-175, Mar 2007, doi: 10.1038/nature05570.

[83] Stan C. Davis, Vonda C. Sheppard,Gousia Begum, Ye Cai, Yunnan Fang, John D. Berrigan, Nils Kröger, and Kenneth H. Sandhage, "Rapid Flow-Through Biocatalysis with High Surface Area, Enzyme-Loaded Carbon and Gold-Bearing Diatom Frustule Replicas," (in English), Advanced Functional Materials, Article vol. 23, no. 36, pp. 4611-4620, Sep 2013, doi: 10.1002/adfm.201203758.

[84] Y. N. Fang, J. D. Berrigan, Y. Cai, S. R. Marder, and K. H. Sandhage, "Syntheses of nanostructured Cu- and Ni-based micro-assemblies with selectable 3-D hierarchical biogenic morphologies," (in English), Journal of Materials Chemistry, Article vol. 22, no. 4, pp. 1305-1312, 2012, doi: 10.1039/c1jm13884g.

[85] D. Losic, J. G. Mitchell, and N. H. Voelcker, "Diatomaceous Lessons in Nanotechnology and Advanced Materials," (in English), Advanced Materials, Review vol. 21, no. 29, pp. 2947-2958, Aug 2009, doi: 10.1002/adma.200803778.

[86] Y. T. Liu and T. Tian, "Fabrication of Diatomite/Silicalite-1 Composites and Their Property for VOCs Adsorption," Materials, vol. 12, no. 4, Feb 2019, Art no. 551, doi: 10.3390/ma12040551.

[87] Dingxin Liu, Jiajun Gu, Qinglei Liu, Yongwen Tan, Zhuo Li, Wang Zhang, Yishi Su, Wuxia Li, Ajuan Cui, Changzhi Gu, and Di Zhang, "Metal-Organic Frameworks Reactivate Deceased Diatoms to be Efficient CO2 Absorbents," Advanced Materials, vol. 26, no. 8, pp. 1229-1234, Feb 2014, doi: 10.1002/adma.201304284.

[88] Z. J. Ren, H. M. Gao, H. Q. Zhang, and X. Liu, "Effects of fluxes on the structure and filtration properties of diatomite filter aids," (in English), International Journal of Mineral Processing, Article vol. 130, pp. 28-33, Jul 2014, doi: 10.1016/j.minpro.2014.05.011.

[89] R. J. Zheng, Z. J. Ren, H. M. Gao, A. L. Zhang, and Z. Bian, "Effects of calcination on silica phase transition in diatomite," Journal of Alloys and Compounds, vol. 757, pp. 364-371, Aug 2018, doi: 10.1016/j.jallcom.2018.05.010.

[90] H. Giesche, "Mercury porosimetry: A general (practical) overview," Particle & Particle Systems Characterization, vol. 23, no. 1, pp. 9-19, Jun 2006, doi: 10.1002/ppsc.200601009.

[91] Xue Bin Ke, Zhan Feng Zheng, Hong Wei Liu, Huai Yong Zhu, Xue Ping Gao, Li Xiong Zhang, Nan Ping Xu, Huanting Wang, Hui Jun Zhao, Jeffrey Shi, and Kyle R. Ratinac, "High-flux ceramic membranes with a nanomesh of metal oxide nanofibers," Journal of Physical Chemistry B, vol. 112, no. 16, pp. 5000-5006, Apr 2008, doi: 10.1021/jp709837r.

CHAPTER 3: Surface-enhanced Raman Scattering Sandwich Assay for Point-of-Care Biosensing

3.1 Abstract

A point-of-care biosensor based on a surface-enhance Raman spectroscopy (SERS) sandwich assay platform is developed using silver nanocubes (AgNCs) on a gold capture substrate. The specific chemistry of the streptavidin-biotin system is used as a model system to demonstrate the facile and sensitive biosensing capabilities. Both the AgNCs and the capture substrate were functionalized with a heterobifunctional ligand, biotin-polyethylene glycol-thiol. The ability for the AgNCs to bind to the capture substrate depends on the concentration streptavidin present and is characterized using SERS and scanning electron microscopy. The Raman reporter, 2-napthethalenethiol, is also bound to the surface of the AgNCs for ultrasensitive SERS detection of AgNC binding. The flat surface of the AgNCs bound to the gold surface provide a high area of plasmon coupling between the localized surface plasmons of the AgNCs and the long-range plasmons of the gold capture substrate; thereby, providing a near-field enhancement of the Raman reporter unavailable to similar SERS sandwich assay platforms. Further functionalization and surface treatment of the capture substrates were performed to reduce the non-specific binding of AgNC and increase the biosensor's signal-to-noise ratio. The optimized sensor was able to sense streptavidin in the picomolar range with a limit of detection of 70 pM.

3.2 Introduction

The importance of both accurate and rapid biosensing has been highlighted by the 2019 coronavirus disease (COVID-19) pandemic where detecting the virus provides

crucial information for preventing further spread of the virus and for further treatment of the patient [92-94]. Applications of biosensing extend into a plethora of medical diagnoses where the detection of biomolecules (e.g., small molecules, nucleic acids, and proteins) can reveal the presence of various diseases (e.g., diabetes, heart disease, cancer, etc.) [95]. Current gold standard techniques for the accurate detection of nucleic acids and proteins are polymerase chain reaction (PCR) and enzyme-linked immunosorbent assay (ELISA). However, these techniques require a mixture of a laboratory setting, expensive reagents/equipment, long test-times, and trained professionals to perform the tests. To circumvent these issues, point-of-care testing (POCT) aims to provide rapid results directly to patients without the need of sending samples to a laboratory [96]. For example, the lateral flow immunoassay (LFIA) is one of the most used POCT techniques, including for diagnosis of COVID-19, due to a combination of its low price, ease-of-use, and quick results. However, LFIA's reliance on non-quantitative colorimetric analysis results in low sensitivity and the inability to determine the concentration of a target analyte [96]. Therefore, developing techniques that increase the sensitivity of such POCT techniques will enable the detection low analyte concentration applications and trust in these techniques to give minimal false results, preventing the need of further expensive and time-consuming tests.

Recent research has investigated POCT techniques which use surface-enhanced Raman scattering (SERS) as the method of detection due to its ultrasensitive capabilities [96-98]. SERS is obtained from plasmonic nanostructure or nanoparticles which possess oscillating free electrons capable of concentrating light into "hot spots" of localized large

field enhancements. These hot spots, located near the surface of plasmonic nanoparticles, provide orders of magnitude increase in the Raman scattering of molecules located inside which have resulted in single-molecule detection [8, 9]. Although SERS biosensors in some cases detect analytes directly [102, 103], it is common for the nanoparticles (SERS nanotags) to be molecularly functionalized with large Raman cross-sections molecules (Raman reporters) to increase the sensitivity [98, 103-6]. The advantages of using SERS nanotags as the labeling agent, as opposed to other colorimetric labeling approaches (e.g., fluorescence and horse-radish peroxide), are the ability for multiplexed detection, minimal photobleaching, use of near-infrared excitation to avoid autofluorescence of biological samples, and quantification (assuming the SERS signal is proportional to SERS nanotags) [99, 107-109]. However, a key disadvantage for SERS-based POCT is the need for a Raman spectrometer which currently have commercial cost greater than $12,000 U.S. [110]. This limits widespread personal use of such techniques, however, its use as a rapid, easy-to-use, ultrasensitive diagnostic technique in hospitals has been demonstrated to accurately detect various forms of cancer [104, 111-113]. Moreover, further advances in custom Raman spectrometers have demonstrated prices below $1,000 U.S. which show promise for future widespread use of SERS-based POCT [110].

Efforts made to maximize the electric field enhancement of plasmonic nanostructures make use of plasmon coupling which occurs when neighboring plasmons in resonance start to hybridize [102, 106, 115-118]. Compared to a single nanoparticle, this plasmon resonance achieves several orders of magnitude increase in the electric field enhancement in a small region (i.e., the nanogap) between the two nanoparticles. SERS-

based biosensors that make use of the large electric field enhancement in the nanogap can obtain unrivaled sensitivities. For example, a 100-attomole detection of the malaria parasite *Plasmodium falciparum* was detected using a core-gap-shell nanoparticle with a Raman reporter loaded inside the nanogap obtained by the resonance between the core and shell [105]. Another example instead utilizes the large field enhancements of the nanogap in a sandwich immunoassay of silver nanocubes (AgNCs) on a gold substrate for surface-enhanced fluorescence (SEF) detection of the cardiac biomarker B-type natriuretic peptide [119]. The uniform nanogap created by the flat AgNCs and gold substrate provide a large area of large electric field enhancement that resulted in more than 100-fold fluorescence enhancement of the detection antibody. Zeng et al. further investigated AgNCs on a gold substrate by fabricating a metasurface of equally spaced AgNCs using a Langmuir-Blodgett deposition method [116]. The results, coupled by simulation, demonstrate an order of magnitude increase in overall field enhancement compared AgNCs on a silicon substrate (no plasmon coupling).

Here, we investigate the use of AgNCs labeled with the Raman reporter, 2-naphthalenethiol, as the SERS nanotag in a sandwich assay to rapidly detect streptavidin. Streptavidin forms a biotin-streptavidin-biotin bridge between AgNCs and a gold capture substrate which are both functionalized with the heterobifunctional linker, biotin-PEG-thiol. The SERS spectrum of the fabricated AgNC sandwich assay were obtained and the distinct peaks from the AgNC-bound Raman reporter were quantified. In this work, two key assumptions which are necessary to obtain a SERS nanotag-based quantitative biosensor [99] were investigated: (i) the AgNC binding to the capture substrate is directly

proportional to the amount of bound streptavidin and (ii) the SERS signal is directly proportional to the amount of AgNC binding to the capture substrate. In addition to providing quantitation, the investigation of the adherence to these assumptions serves to decrease background signal from nonspecific binding of either streptavidin or AgNCs to the substrate and achieve a low limit of detection. This SERS sandwich assay platform uses the streptavidin-biotin complex as a model system but can potentially be further extended into a variety of specific binding chemistries (e.g., antibodies, aptamers, peptides, etc.) for ubiquitous rapid and sensitive biosensing.

3.3 Materials and Methods

3.3.1 AgNC Synthesis and Ligand Exchange:

AgNC (average edge length 70 - 80 nm) were synthesized using a modified polyol method previously described [116, 120, 121]. The as synthesized AgNC are capped with polyvinyl pyrrolidone (PVP, average M_W 55 kDa). After filtration with 0.65, 0.45, and 0.22 μm mesh filter paper (Millipore Durapore) the AgNCs are centrifuged and solvent exchanged from 1,5-pentanediol to ethanol. The AgNCs are then centrifuged, and solvent exchanged again with a mixture of water and ethanol (50:50 v/v). Next, the dispersed AgNCs undergo a ligand exchange process to displace the PVP with a mixture of 1 μM 2-naphthalenethiol and 10 μM biotin-PEG-thiol (average M_W 5 kDa, Nanocs) in a mixture of water and ethanol (50:50 v/v). After 72 h of continuous mixing, the biotinylated AgNCs are then centrifuged, and solvent exchanged 7 times with PBS-T to ensure complete removal of unbound ligands. Controlling the pH was necessary to promote the specific binding chemistry of the biotin head groups from both the capture substrate and AgNCs with the streptavidin used in the sandwich assay fabrication. Moreover, the Tween20 is necessary due to maintaining the stability of AgNCs despite the increase in pH and ionic strength from the buffer solution. The ligand exchange of the AgNCs were characterized UV-vis spectroscopy (Agilent Cary 60 UV-vis Spectrophotometer).

3.3.2 Au Capture Substrate Fabrication

Diced silicon substrates (1 x 1 cm) were sputtered with a Denton Discovery 18 system to obtain a thin Au surface layer. These Au substrates were then treated with piranha solution for 2 minutes and further washed with water and ethanol. Next, each cleaned Au

substrates was immersed overnight on a rocking table in 1 mL of ethanolic solution containing 1 mM total of biotin-polyethylene glycol (biotin-PEG-thiol, average M_W 1 kDa, Nanocs) or a mixture of biotin-PEG-thiol and polyethylene glycol methyl ether thiol (mPEG-thiol, average M_n 800, Sigma-Aldrich). The functionalized Au capture substrates were then washed with 5 times with 1 mL ethanol and 2 times with 1 mL water and then transferred into 1 mL of 1X PBS buffer solution (pH 7.4) containing 0.1 wt.% of Tween20 (PBS-T) for 30 minutes. The PBS-T incubation was used as a blocking step to prevent nonspecific binding of streptavidin in the following step in the sandwich assay fabrication.

3.3.3 AgNC Sandwich Assay Fabrication

The biotinylated Au capture substrates incubated with varying concentrations of the analyte streptavidin (Thermo Fisher Scientific) in a PBS-T solution for 1 h and with control samples undergoing same procedure but without streptavidin exposure. After streptavidin incubation the capture substrates are washed five times with PBS-T to ensure only specifically bound streptavidin remain. The sandwich assay is then fabricated by immersing the streptavidin-functionalized capture substrates in 1 mL of biotinylated AgNCs (OD 5 unless otherwise stated) for 1.5 h. The AgNC sandwich assays undergo the final washing process consisting of each substrate being immersed in 3 consecutive beakers with 50 mL water followed by 10 mL of ethanol and left to dry before further characterization. To prevent the non-specific binding of streptavidin and AgNCs to the capture substrate, one experiment included extra steps before and after the streptavidin incubation that consisted of a 1 h and a 30 min incubation with 3 wt.% bovine serum

albumin (BSA, Sigma-Aldrich) in PBS-T, respectively. The blocking steps were followed up with a single wash of PBS-T solution to remove unbound BSA.

3.3.4 AgNC Sandwich Assay Characterization

AgNC sandwich assays were first characterized using a Raman spectroscopy set-up (Renishaw inVia microscope) and excited with a 785 nm laser line (Renishaw 300 mW stripe diode laser). A 49-point (7 x 7) map of Raman spectra were obtained that were each 20 μm apart near the center of the substrates. The 49 spectra per sandwich assay were averaged in Origin graphing software and further analyzed for biosensor characterization. The sandwich assays were then imaged with scanning electron microscopy (SEM) using a Zeiss Sigma 500 at 5k eV power. These SEM images were processed in ImageJ software to quantify the surface coverage of the nanocubes on the gold substrates.

3.4 Results and Discussion

3.4.1 Functionalization of AgNCs

In this work we develop a point-of-care (POC) biosensor based on a SERS sandwich assay platform using AgNCs on a gold capture substrate, as shown in Figure 3.1. Figure 3.1a shows the AgNCs, as synthesized, are capped with polyvinylpyrrolidone (PVP) and undergo a ligand exchange process to displace the PVP with a mixture thiol-PEG-biotin and 2-naphthalenethiol. The AgNC ligand exchange was confirmed with UV-vis spectroscopy (Figure 3.2a) which shows a splitting of the dipole resonance peak with a blue-shifted peak appearing which suggests a change in surface ligands due to a change in the AgNC surface dielectric constant. For these biotinylated AgNCs to be able to efficiently bind to streptavidin the AgNCs need to be redispersed from water to a PBS (pH 7.4) buffer

solution. However, as shown in Figure 3.2b, the change in pH and electrolyte concentration causes quick aggregation of AgNCs due to a decrease in the repulsion of the electric double layer that prevented aggregation caused by Van der Waals attraction between AgNCs. Therefore, a polysorbate-type nonionic surfactant, Tween20, is also added to the PBS (PBS-T, 0.1 wt.%) solution before the addition of the biotinylated AgNCs to ensure AgNC stability while maintaining an environment that enables the specific binding chemistry of streptavidin and biotin head groups. Tween20 is commonly used to prevent non-specific binding onto capture substrates of enzyme-linked immunosorbent assays and to ensure the stability of metal nanoparticles in biological buffers [122, 123].

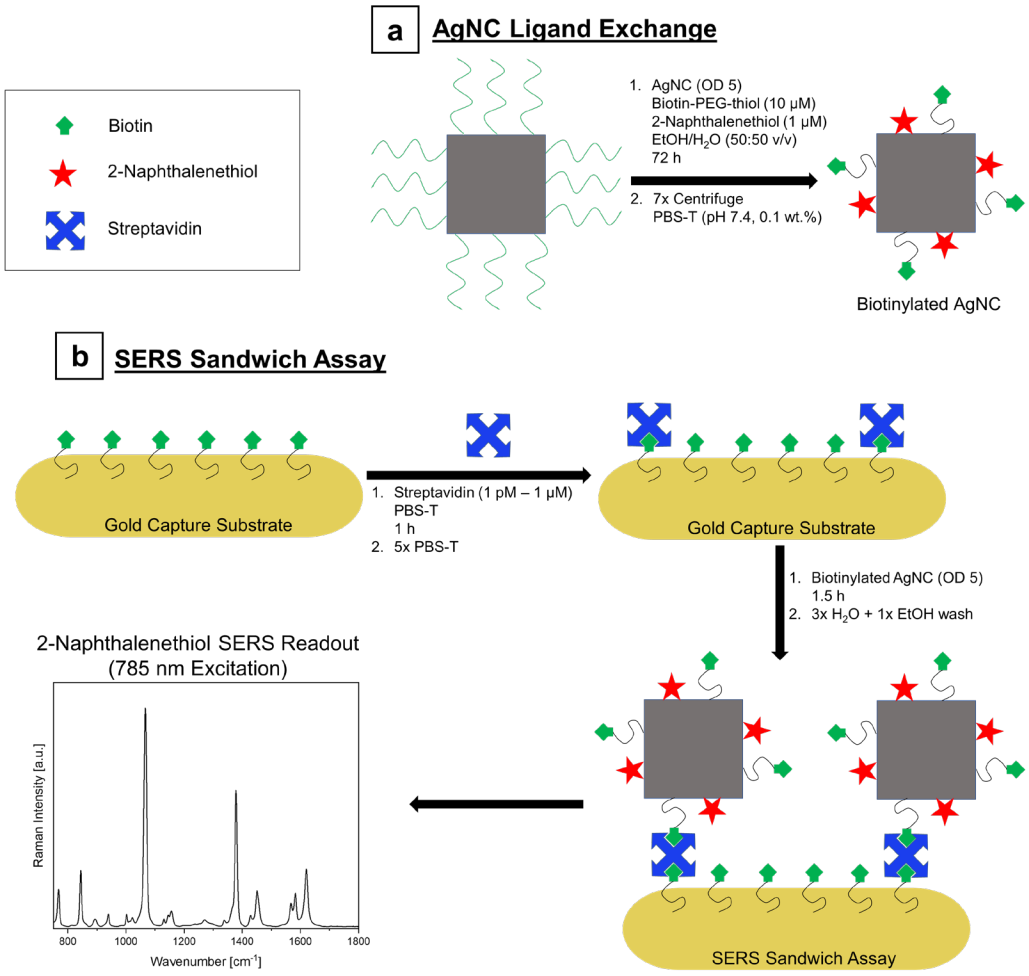

Figure 3.1: Fabrication process of surface-enhanced Raman scattering sandwich assay for detection of streptavidin. **(a)** PVP capped AgNCs are synthesized and undergo a ligand exchange with 10 µM 2-naphthalenethiol (Raman reporter) and 100 µM Biotin-PEG-thiol for 72 h. **(b)** Gold substrate is functionalized with Biotin-PEG-thiol and further incubated in varying concentrations of streptavidin in a PBS-Tween solution for 1 h. Then the substrates are incubated in a solution containing the biotinylated AgNCs for 1.5 h. Streptavidin specifically binds with the biotin headgroups of both the capture substrate and AgNCs forming a sandwich assay. The sandwich assay is then excited with a 785 nm laser and the 2-napthalenethiol Raman spectrum is obtained for further analysis. Schematic is not drawn to scale.

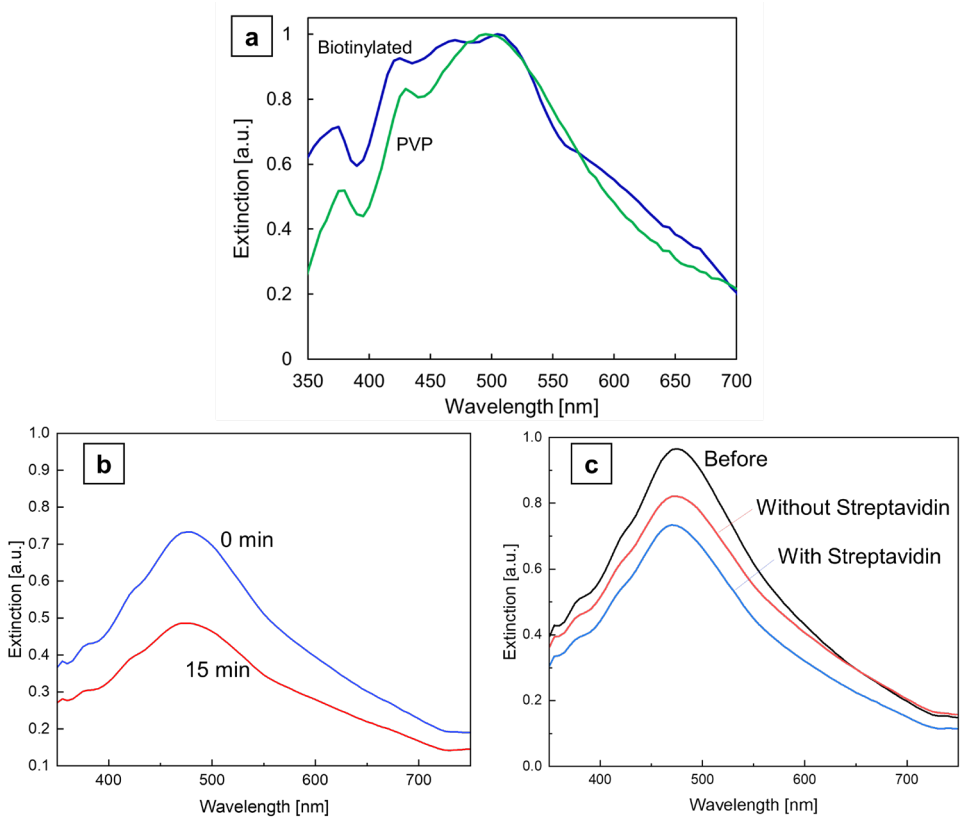

Figure 3.2: **(a)** UV-vis spectra of AgNCs in water before and after ligand exchange (biotinylation) displacing the PVP on the surface of the AgNCs with biotin-PEG-thiol and 2-naphthalenethiol. **(b)** UV-vis spectra of biotinylated AgNCs after being solvent exchanged from an aqueous solution into a PBS (pH 7.4) buffer solution. In 15 minutes, a sharp decrease in intensity is observed due to aggregation demonstrating the necessary addition of a surfactant, Tween20, for stabilization of the AgNCs. **(c)** UV-vis spectra of AgNC samples in PBS-Tween solutions. Streptavidin (10 nM) was introduced to one sample and compared to a control over a period of 5 days to observe aggregation expected to occur due to streptavidin specifically binding biotinylated AgNCs together.

The successful binding of streptavidin to the biotinylated AgNCs was confirmed by comparing the UV-vis spectra of biotinylated AgNCs with and without the presence of streptavidin over a period of 5 days, as shown in Figure 3.2c. Although both samples experience aggregation, the sample containing streptavidin shows a 9.4% greater decrease in AgNC dipole peak intensity suggesting additional streptavidin-induced aggregation. These data further demonstrate the successful biotinylation of AgNCs and the successful specific binding of streptavidin to the exposed biotin head groups on the AgNC surfaces.

3.4.2 SERS Sandwich Assay

3.4.2.1 AgNC Concentration Optimization

To determine the best concentration of biotinylated AgNCs needed during the fabrication of the SERS sandwich (Figure 3.1b), the concentration of the analyte, streptavidin, was fixed at 100 nM while the concentrations of the biotinylated AgNCs used were OD 0.1, 0.5, 1, and 5 (OD, Optical density refers to the dipole peak intensity during UV-vis spectroscopy). Figure 3.3a shows the SERS spectrum obtained of the sandwich assay with OD 5 AgNC, where there are noticeable peaks from the Raman reporter, 2-naphthalenethiol, most notably demonstrated by the dominant C-H bending peak located at 1066 cm^{-1} [124, 125]. SEM images taken reveal a substantial difference between the amount of AgNC binding that occurs on the capture substrate with OD 5 compared to OD 1 (Figure 3.3b). Moreover, Figure 3.3c reveals that the OD 5 sample outmatches the lower concentration samples by nearly two orders of magnitude with respect to the 1066 cm^{-1} peak intensities which is in agreement with the absence of nearly any AgNC binding seen with SEM. Processing the SEM images with ImageJ software, the surface coverage of bound AgNCs were quantified for further comparison of the OD 5 sample with its control that underwent the same conditions but without any streptavidin present, as shown in Figure 3.3d. The OD 5 sample outperforms its control nearly 5-fold in terms of both the 1066 cm^{-1} peak intensity and surface coverage which suggests that although there is substantial non-specific binding of AgNCs there may be additional specific binding caused by the streptavidin present.

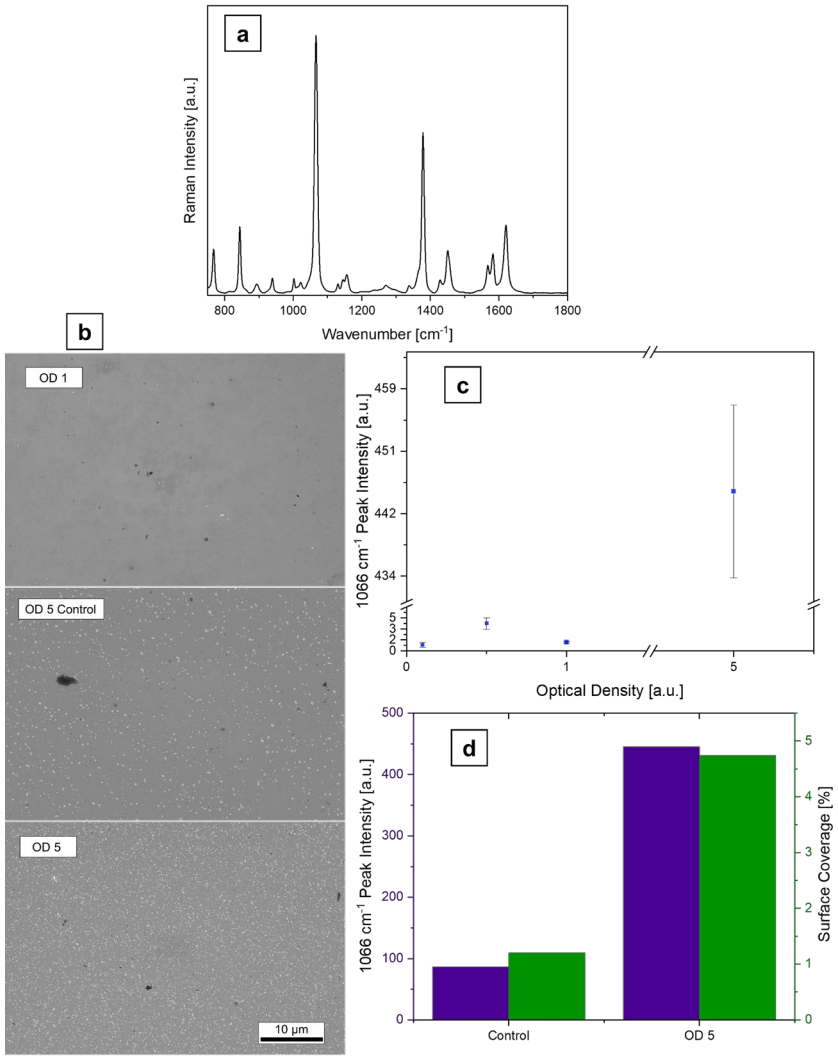

Figure 3.3: **(a)** SERS analysis on Ag nanocube sandwich assay (OD 5) showing a strong 2-naphthalenethiol 1066 cm^{-1} peak which corresponds to a C-H bend and is used to quantify further characterization of the biosensor. **(b)** SEM was also used to characterize sandwich assay fabricated by varying optical densities (OD 0.1, 0.5, 1, and 5) of AgNCs used during the incubation with functionalized capture substrates that were previously incubated with 100 nM streptavidin (control samples were not incubated with streptavidin). **(b)** Shows substantial difference in AgNC binding between OD 1, OD 5, and the control sample for OD 5 with nearly zero nanocubes present with samples OD 0.1, 0.5, and 1. **(c)** Further demonstrates the largest 1066 cm^{-1} signal with OD 5 due to more binding of AgNCs. Data points are the mean of N = 49 measurements taken at different points on the same sample with error bars representing ± standard error. **(d)** Compares the 1066 cm^{-1} signal of sample OD 5 with its control (no streptavidin) as well as the surface coverage quantified from SEM images processed with ImageJ software. The data show a clear increase in binding of nanocubes due to presence of streptavidin.

3.4.2.2 Streptavidin Detection:

The SERS sandwich assay was tested for its detection of streptavidin (10 fM – 1 μM) with biotinylated AgNCs at a fixed concentration of OD 5. Figure 3.4a shows a weak correlation between streptavidin concentration and SERS signal and the average SERS signal of the controls (grey dashed line) is surprisingly larger than all samples exposed to streptavidin except for the 1 μM sample. This suggests that the sensor is generally unable to distinguish between the specific binding caused by streptavidin and nonspecific binding of the AgNC to the capture substrate. The error bars represent the ± the standard error of SERS spectra taken from 49 different points spaced 20 μm apart in a given sample and suggest all samples have a homogenous surface coverage of AgNCs across a 140 x 140 μm area of the sample. This is further demonstrated in Figure 3.4b showing a SEM image of homogenous surface coverage of isolated AgNCs on the 1 μM streptavidin sample. Although the issue of nonspecific binding needs to clearly be addressed, the homogenous surface coverage of unaggregated AgNCs is desired for obtaining a quantitative biosensor. That is, if there are fluctuations in analyte and/or AgNC binding to the capture substrates, the reproducibility of the biosensor will suffer [99]. Furthermore, not having AgNCs aggregation is essential to maintain a linear relationship between surface coverage and SERS signal, shown in Figure 3.4c. Conversely, if there are aggregates, the charge transfer between AgNCs will quickly diminish the enhancement factor, leading to a similar surface coverage with a weaker SERS signal.

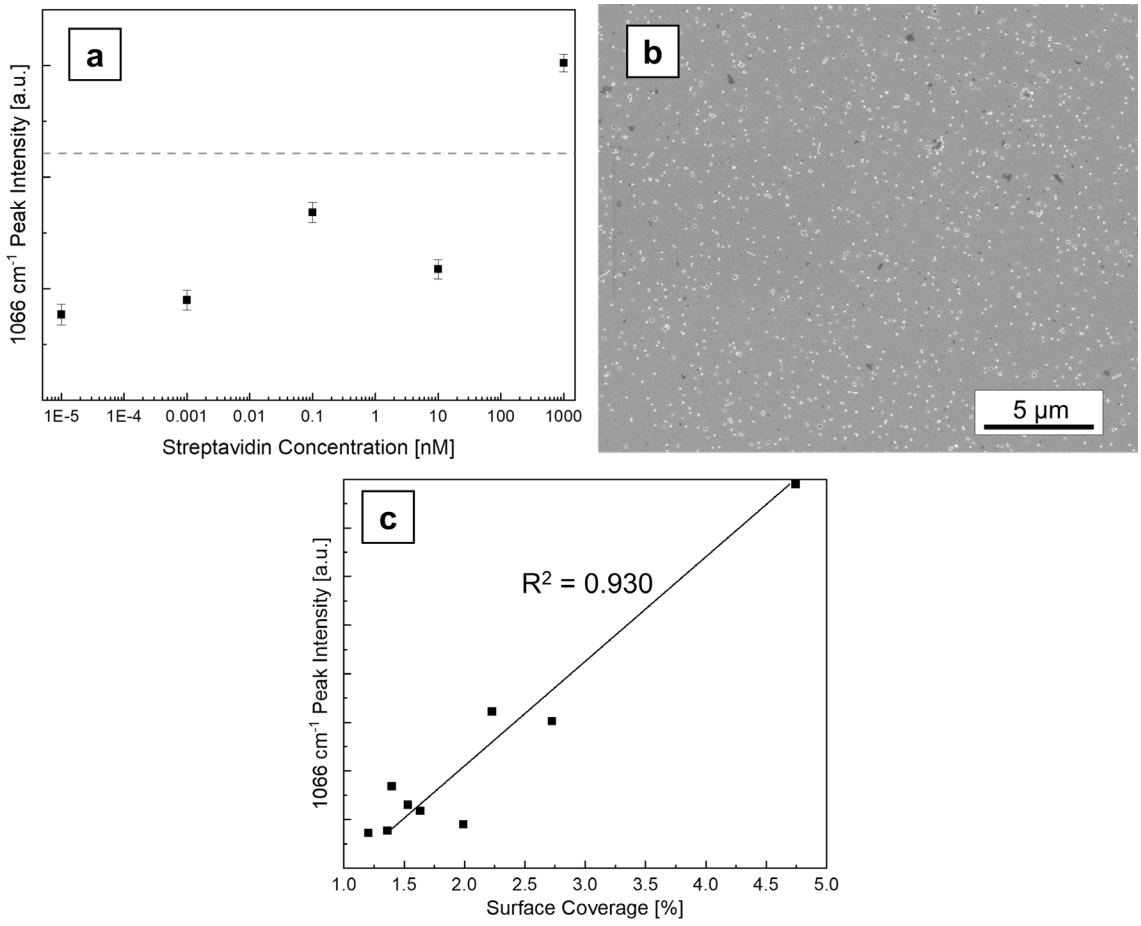

Figure 3.4: **(a)** Raman analysis of Ag nanocube sandwich assays with varying streptavidin concentrations (10 fM, 1 pM, 100 pM, 10 nM, and 1 µM) used during incubation of biotinylated capture substrates. Dotted line represents the average 1066 cm^{-1} signal of control samples (N = 4). Data points are the mean of N = 49 measurements taken at different points on the same sample with error bars representing ± standard error. **(b)** SEM of 1 µM streptavidin sample showing homogenous coverage of the capture substrate. **(c)** Surface coverage of Ag nanocubes on Au capture substrate measured with ImageJ software from SEM images plotted against Raman output. The data are cumulative from all OD 5 samples, including controls, and demonstrate a clear correlation between the amount of nanocubes binding to the capture substrates (i.e., surface coverage) and the SERS detection of the 2-naphthalenethiol.

Creating a quantitative SERS sensor relies on obtaining reproducible data that minimizes false conclusions regarding the presence or absence of the analyte (i.e., false-positives and false-negative, respectively). A quantitative SERS sensor is obtained by establishing a reproducible relationship between the spectral data and the analyte

concentration, either through a linear fit or with the Langmuir adsorption isotherm [126, 127]:

$$I = B - I_{max}\frac{Ac_s}{1 + Ac_s} \tag{3.1}$$

Where c_s is concentration of the analyte, I is the peak intensity from the chosen peak in the SERS data, I_{max} is the maximum peak intensity obtained, B is a constant obtained from the offset from the background, and A is the Langmuir constant. Using the Langmuir isotherm model, as opposed to a linear fit, is performed when the SERS sensor is operating in a large enough dynamic range where the linear region is in the center of a sigmoidal curve of a semi-log SERS signal vs. analyte concentration plot. Moreover, it has been demonstrated that using this non-linear Langmuir isotherm model also provides more accuracy compared to linear regression models [126]. Although this model accounts for the adsorption of the analyte (streptavidin) to the capture substrate, the binding of the AgNCs is unaccounted for and a SERS sandwich assay protocol would need to assume that AgNC binding is directly proportional to streptavidin concentration for the Langmuir isotherm model to be valid. Additionally, the model assumes the SERS signal is directly proportional to the surface concentration of streptavidin. Therefore, if there is AgNC aggregation on the capture substrate it would create a non-linear relationship between AgNC surface coverage and SERS signal. Consequently, this would nullify the assumption that the streptavidin concentration is directly proportional to the SERS signal and ultimately lead to poor fitting from linear regression or the Langmuir isotherm model.

To minimize non-specific binding of both streptavidin and AgNCs to the capture substrate, blocking steps (BSA 3 wt.% in PBS-T) before and after streptavidin incubation

were added into the SERS sandwich assay fabrication. Blocking steps are commonly done in enzyme-linked immunosorbent assays (ELISA) protocols, where minimizing non-specific binding while maintaining optimal specific binding is needed to improve biosensing capabilities [128]. Figure 3.5a reveals the SERS signals of the sandwich assays fabricated with blocking steps which were incubated with five concentrations of streptavidin (100 pM, 1 nM, 10 nM, 100 nM, and 1 μM). These results demonstrate a clear increase in SERS signal between samples with higher streptavidin concentration (10, 100, and 100 nM) and the samples with either lower streptavidin concentration (100 pM and 1 nM) or no streptavidin at all (denoted by dashed grey line representing average of signal of control samples, N = 5). These data suggest that including the blocking steps into the sandwich assay fabrication successfully decreased nonspecific binding and allowed for a larger dynamic range of streptavidin concentrations to be detected and differentiated from control samples. Figure 3.5b shows strong correlation (R^2 = 0.955) between the SERS signal and surface coverage of AgNCs for all samples expect the 1 μM streptavidin. The strong correlation is attributed to the homogenous surface coverage of unaggregated nanocubes, shown in Figure 3.5c, where the average enhancement factor provided by the AgNCs remains constant. However, the 1 μM sample shows a clear deviation from the linear trend which is explained by Figure 3.5d showing an SEM image of the aggregation that began to frequently occur, likely due to the larger surface coverage promoting more particle-particle interactions. When comparing these results to other SERS sensors detecting streptavidin the limit of detection (LOD) is unexpectedly high [129-131]. For example, Haes et al. and You et al. obtained streptavidin LODs 1 pM and 20 pM,

respectively, which are orders of magnitude lower than the lowest detected concentration of 10 nM. Including BSA blocking steps have demonstrated a method to decrease nonspecific binding but there may still be issues preventing a lower LOD of streptavidin. Possible issues include unlabeled contaminants in BSA sample causing streptavidin-biotin interactions [128, 132], BSA forming complexes with the PEGylated nanoparticles [133], and/or the abundance of negatively charged biotin head groups (pI ~ 5) on the capture substrate causing electrostatic repulsion with the streptavidin (pI ~ 6.3) in a PBS solution with pH 7.4 and significant concentration of counterions [134, 135]. Furthermore, the additional blocking and washing steps further increased the time needed to perform the assay which is undesirable for POC sensing applications [99] and led to us exploring other routes to increase the signal to noise of the SERS sandwich assay.

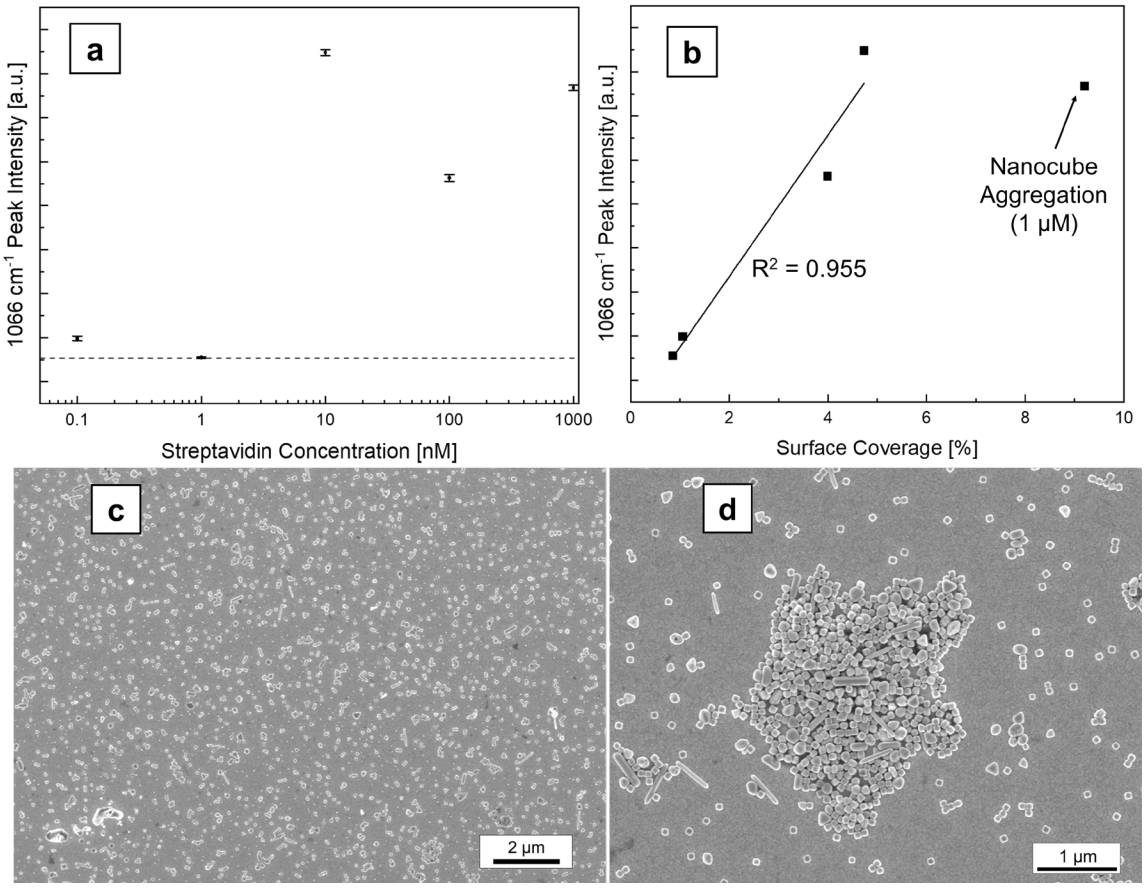

Figure 3.5: **(a)** Raman analysis of Ag nanocube sandwich assays with varying streptavidin concentrations (100 pM, 1 nM, 10 nM, 100 nM, and 1 µM) used during incubation after the biotinylation and blocking steps of capture substrates. Dotted line represents the average 1066 cm^{-1} signal of control samples (N = 5). Data points are the mean of N = 49 measurements taken at different points on the same sample with error bars representing ± standard error. **(b)** Surface coverage of Ag nanocubes measured with ImageJ software from SEM images plotted against the 1066 cm^{-1} Raman peak intensity. Positive correlation is demonstrated (R^2 = .955) which is attributed to homogenous coverage of all samples except for the 1 µM streptavidin sample. **(c)** is an SEM image that shows homogenous surface coverage of nanocubes on the 10 nM streptavidin sample and conversely **(d)** demonstrates the heterogeneity from the aggregates forming on the 1 µM streptavidin sample.

To address minimizing nonspecific binding without the use of extra blocking and washing steps, a mixed monolayer (MML) functionalization was performed for the biotinylation step of the gold capture substrates. The substrates were immersed in an ethanolic solution of 3:2 mol ratio of mPEG-thiol (800 Da) and biotin-PEG-thiol (1 kDa) at a total concentration of 1 mM. The methoxy head group replacing a fraction of the biotin

head groups serve to increase the hydrophobicity of the substrate to prevent protein-substrate contact between streptavidin and the gold capture substrate and potentially reduce the electrostatic repulsion occurring between biotin and streptavidin [134-136]. The mPEG-thiols were chosen to be a shorter chain length than biotin-PEG-thiol to ensure the methoxy head groups do not interfere with the specific binding of streptavidin. Figure 3.6a shows the results of the sandwich assay and demonstrate a sharp increase in sensitivity of streptavidin while also maintaining minimal nonspecific binding compared to the experiment using BSA blocking steps. The LOD (red line) is calculated using the following equation [127]:

$$I_{lim} = \bar{I}_c + 3\delta_c \tag{3.2}$$

Where $\bar{I}_c$ is the average SERS signal of the control samples, δ_c is the sample-to-sample standard deviation in the SERS signal of control samples, and I_{lim} is the LOD in terms of the SERS signal. To obtain the LOD in terms of analyte concentration I_{lim} is substituted into Equation 3.1 (solid black curve in Figure 3.6a) to obtain the associated the c_s value. The LOD obtained of streptavidin is 70 pM which is an improvement from BSA-blocking fabrication route but is still substantially higher than other SERS biosensor platforms. Moreover, the correlation ($R^2 = 0.811$) demonstrates a poor fit of the data which is attributed to the inconsistency of maintaining homogenous surface coverage of unaggregated AgNCs. Figure 3.6(b) shows an SEM image of the 10 nM sample and reveals a homogenous surface coverage of AgNCs. Conversely, aggregation is clearly demonstrated by the 1 and 100 nM samples shown in Figure 3.6(c and d), respectively.

This microscopic-scale aggregation is similar to previously observed drying-mediated assembly of nanoparticles on planar substrates [137]. These results corroborate the significant drop in SERS signal in Figure 3.6a for these samples and why there is a poor fit with the Langmuir isotherm model. Figure 3.6e shows the 10 pM sample with minimal AgNCs which is also representative of the samples below 10 pM streptavidin (including controls) which explain the lower SERS signal for these samples, as expected.

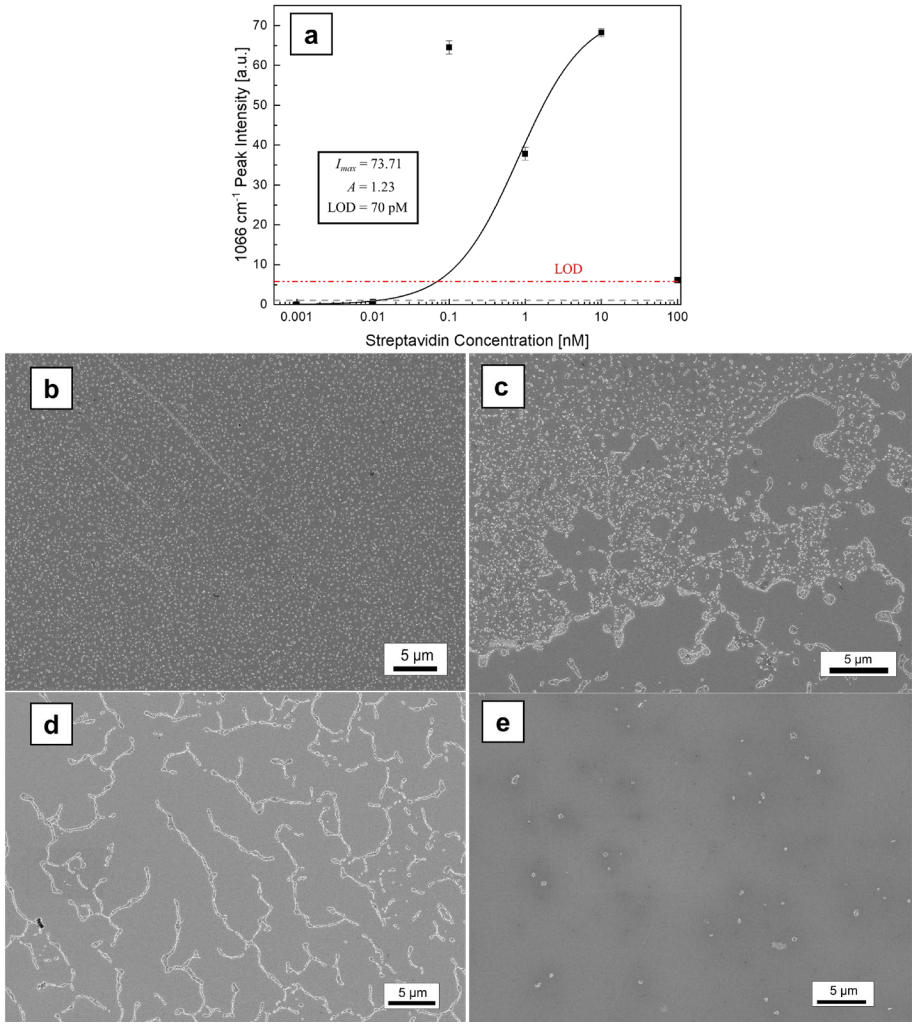

Figure 3.6: **(a)** SERS analysis of AgNC sandwich assays with varying streptavidin concentrations (1 pM, 10 pM, 100 pM, 1 nM, 10 nM and 100 nM) used during incubation after the surface functionalization of the gold capture substrates with methoxy-PEG-thiol and biotin-PEG-thiol (3:2 molar ratio ethanolic solution). Grey dashed line represents the average 1066 cm^{-1} signal of control samples (N = 4) and the red dash-dotted line represents the limit of detection (LOD) in units of cm^{-1} calculated from Equation 3.1. The black curve is the Langmuir isotherm fit from Equation 3.2 and gives the fit parameters I_{max} and A (R^2 = 0.811). The 1 µM sample was omitted from fit due to severe aggregation. Combining Equations 3.1 and 3.2 gives the LOD of 70 pM streptavidin. Data points are the mean of N = 49 measurements taken at different points on the same sample with error bars representing ± standard error. **(b)**, **(c)**, **(d)** and **(e)** are SEM images taken of the final sandwich assays with **(b)** showing the 10 nM streptavidin sample homogeneously with a mixture of isolated AgNCs and small AgNC aggregates formed. Conversely, **(c)** and **(d)** reveal aggregation occurring on the 1 and 100 nM samples. **(e)** shows the lack of AgNC surface coverage on the 10 pM sample.

The MML fabrication route improved the signal to noise for detection of streptavidin compared to BSA-blocking route, although it also introduced more AgNC aggregation. The SEM patterns of AgNC aggregation due to drying was unexpected, as the biotin-streptavidin-biotin bridge forming the sandwich assay was predicted to anchor the AgNCs in place due to strong non-covalent interactions. However, it has been previously demonstrated that drying can cause conformational change or denaturing of streptavidin [138-140]. This issue from drying may have not only affected the aggregation of surface bound AgNCs but may have also decreased the amount of streptavidin bound to the surface during the washing steps done directly after the streptavidin incubation. Each washing step was followed by a window of ~1 min of direct exposure to air and, due to the increased hydrophobicity of these substrates, may have been enough time for drying and denaturing of the bound streptavidin.

3.5 Conclusions

In this work, a novel SERS sandwich assay was developed for use as a highly sensitive POC biosensor. The biosensor is fabricated with a gold capture substrate and flat plasmonic nanoparticles labeled with a Raman reporter (2-naphthalenethiol) that bind to form a sandwich structure in the presence of the analyte (streptavidin). This platform makes use of specific chemistry, as traditionally done with ELISA protocols, but addresses the shortcomings of the traditionally colorimetric platform's sensitivity by utilizing the electric field enhancement of hotspots in the nanogap for a highly sensitive SERS readout of the Raman reporter. Experiments conducted explored the effect of AgNC concentration and two fabrication routes to optimize signal to noise ratio by minimizing non-specific binding

of either streptavidin or AgNCs. Results for the effect of AgNC concentration show spikes in AgNC binding and SERS signal between OD 5 and lower concentrations used (OD 0.1, 0.5, and 1). The reason for this non-linear relationship warrants further investigation as it does not follow non-competitive monolayer adsorption theories (e.g., Langmuir isotherm) and may potentially be due to competitive adsorption on the capture substrate between the Tween20 surfactant and the AgNCs.

The first route explored to decrease background SERS signal caused by nonspecific binding was to include two additional BSA blocking steps in the fabrication protocol, one before streptavidin incubation and another before AgNC incubation. The results successfully demonstrated a clear decrease in AgNC binding for low streptavidin concentration and controls but warranted further optimization as the minimum concentration of streptavidin distinguished from control samples (1 nM) was orders of magnitude higher than the LOD for other SERS biosensors (1 pM and 20 pM) [129, 130]. Therefore, a second route to minimize nonspecific binding was tested by fabricating a mixed monolayer on the capture substrates. The results of this route were more successful as demonstrated by the LOD of streptavidin decreasing to 70 pM although still higher than expected when compared against other SERS biosensors not utilizing a Raman reporters or high-surface area nanogaps with field enhancement > 100 afforded by the nanocube-based SERS sandwich assay [116, 119, 129, 130]. SEM characterization of these assays revealed AgNC monolayer aggregation, typically seen in drying-mediated self-assembly of nanoparticles on a surface [137], despite the biotin-streptavidin-biotin bridge theoretically anchoring the AgNCs to the substrate. Evidently, this aggregation is

hypothesized to be the denaturing of streptavidin caused by the drying steps which can be addressed by utilizing a commercial stabilizer typically used to preserve protein activity during drying [140] or by circumventing drying altogether by performing Raman spectroscopy in aqueous solution [141, 142]. The latter approach would also further reduce the time needed to perform the assay thereby simultaneously improving reproducibility and decreasing assay time. Overall, future studies on SERS sandwich assays will have broad impacts on advancing POC biosensors that require better sensitivity and multiplexing capabilities. However, to achieve these goals understanding the intermolecular and surface forces that govern nanoparticle functionalization/stability and the specific/nonspecific chemistry of the platform are precedent.

3.6 Acknowledgements

Chapter 3, in part is currently being prepared for submission for publications of the material. This work was coauthored by Garner, Sean N.; Bradshaw, Nathan; and Tao, Andrea. The dissertation author was the primary investigator and author of this material. The work presented in this chapter was supported by a National Science Foundation Grant (RAPID CBET-2032196).

3.7 References

[92] Michael A. Johansson; Talia M. Quandelacy; Sarah Kada; Pragati Venkata Prasad; Molly Steele; John T. Brooks; Rachel B. Slayton; Matthew Biggerstaff; Jay C. Butler, "SARS-CoV-2 Transmission From People Without COVID-19 Symptoms," *JAMA Network Open,* vol. 4, no. 1, p. e2035057, 2021-01-07 2021, doi: 10.1001/jamanetworkopen.2020.35057.

[93] Feng Ye, Shicai Xu, Zhihua Rong, Ronghua Xu, Xiaowei Liu, Pingfu Deng, Hai Liu, and Xuejun Xu, "Delivery of infection from asymptomatic carriers of COVID-19 in a familial cluster," *International Journal of Infectious Diseases,* vol. 94, pp. 133-138, 2020-05-01 2020, doi: 10.1016/j.ijid.2020.03.042.

[94] R. Sharma, M. Agarwal, M. Gupta, S. Somendra, and S. K. Saxena, "Clinical Characteristics and Differential Clinical Diagnosis of Novel Coronavirus Disease 2019 (COVID-19)," in *Medical Virology: From Pathogenesis to Disease Control*: Springer Singapore, 2020, pp. 55-70.

[95] S. K. Metkar and K. Girigoswami, "Diagnostic biosensors in medicine – A review," *Biocatalysis and Agricultural Biotechnology,* vol. 17, pp. 271-283, 2019-01-01 2019, doi: 10.1016/j.bcab.2018.11.029.

[96] S. Nayak, N. R. Blumenfeld, T. Laksanasopin, and S. K. Sia, "Point-of-Care Diagnostics: Recent Developments in a Connected Age," *Analytical Chemistry,* vol. 89, no. 1, pp. 102-123, 2017-01-03 2017, doi: 10.1021/acs.analchem.6b04630.

[97] Y. Hang, J. Boryczka, and N. Wu, "Visible-light and near-infrared fluorescence and surface-enhanced Raman scattering point-of-care sensing and bio-imaging: a review," *Chemical Society Reviews,* vol. 51, no. 1, pp. 329-375, 2022-01-01 2022, doi: 10.1039/c9cs00621d.

[98] P. Vohra, P. Strobbia, H. T. Ngo, W. T. Lee, and T. Vo-Dinh, "Rapid Nanophotonics Assay for Head and Neck Cancer Diagnosis," *Scientific Reports,* vol. 8, no. 1, 2018-12-01 2018, doi: 10.1038/s41598-018-29428-0.

[99] Judith Langer, Dorleta Jimenez de Aberasturi, Javier Aizpurua, Ramon A. Alvarez-Puebla, Baptiste Auguié, Jeremy J. Baumberg, Guillermo C. Bazan, Steven E. J. Bell, Anja Boisen, Alexandre G. Brolo, Jaebum Choo, Dana Cialla-May, Volker Deckert, Laura Fabris, Karen Faulds, F. Javier García de Abajo, Royston Goodacre, Duncan Graham, Amanda J. Haes, Christy L. Haynes, Christian Huck, Tamitake Itoh, Mikael Käll, Janina Kneipp, Nicholas A. Kotov, Hua Kuang, Eric C. Le Ru, Hiang Kwee Lee, Jian-Feng Li, Xing Yi Ling, Stefan A. Maier, Thomas Mayerhöfer, Martin Moskovits, Kei Murakoshi, Jwa-Min Nam, Shuming Nie, Yukihiro Ozaki, Isabel Pastoriza-Santos, Jorge Perez-Juste, Juergen Popp, Annemarie Pucci, Stephanie Reich, Bin Ren, George C. Schatz, Timur Shegai, Sebastian Schlücker, Li-Lin Tay, K. George Thomas, Zhong-Qun Tian, Richard P.

Van Duyne, Tuan Vo-Dinh, Yue Wang, Katherine A. Willets, Chuanlai Xu, Hongxing Xu, Yikai Xu, Yuko S. Yamamoto, Bing Zhao, and Luis M. Liz-Marzán, "Present and Future of Surface-Enhanced Raman Scattering," *ACS Nano,* vol. 14, no. 1, pp. 28-117, 2020-01-28 2020, doi: 10.1021/acsnano.9b04224.

[100] L. M. Almehmadi, S. M. Curley, N. A. Tokranova, S. A. Tenenbaum, and I. K. Lednev, "Surface Enhanced Raman Spectroscopy for Single Molecule Protein Detection," *Scientific Reports,* vol. 9, no. 1, 2019-12-01 2019, doi: 10.1038/s41598-019-48650-y.

[101] Liyan Bi 1, Jian Dong, Wei Xie, Wenbo Lu, Wei Tong, Lin Tao, and Weiping Qian, "Bimetallic gold–silver nanoplate array as a highly active SERS substrate for detection of streptavidin/biotin assemblies," *Analytica Chimica Acta,* vol. 805, pp. 95-100, 2013-12-01 2013, doi: 10.1016/j.aca.2013.10.045.

[102] P. A. Mercadal, E. R. Encina, and E. A. Coronado, "Colloidal SERS Substrate for the Ultrasensitive Detection of Biotinylated Antibodies Based on Near-Field Gradient within the Gap of Au Nanoparticle Dimers," *The Journal of Physical Chemistry C,* vol. 123, no. 38, pp. 23577-23585, 2019-09-26 2019, doi: 10.1021/acs.jpcc.9b02974.

[103] J.-H. Lee, M.-H. You, G.-H. Kim, and J.-M. Nam, "Plasmonic Nanosnowmen with a Conductive Junction as Highly Tunable Nanoantenna Structures and Sensitive, Quantitative and Multiplexable Surface-Enhanced Raman Scattering Probes," *Nano Letters,* vol. 14, no. 11, pp. 6217-6225, 2014-11-12 2014, doi: 10.1021/nl502541u.

[104] Hazem Karabeber, Ruimin Huang, Pasquale Iacono, Jason M Samii, Ken Pitter, Eric C Holland, and Moritz F Kircher, "Guiding Brain Tumor Resection Using Surface-Enhanced Raman Scattering Nanoparticles and a Hand-Held Raman Scanner," *ACS Nano,* vol. 8, no. 10, pp. 9755-9766, 2014-10-28 2014, doi: 10.1021/nn503948b.

[105] H. T. Ngo, N. Gandra, A. M. Fales, S. M. Taylor, and T. Vo-Dinh, "Sensitive DNA detection and SNP discrimination using ultrabright SERS nanorattles and magnetic beads for malaria diagnostics," *Biosensors and Bioelectronics,* vol. 81, pp. 8-14, 2016-07-01 2016, doi: 10.1016/j.bios.2016.01.073.

[106] D.-K. Lim, K.-S. Jeon, H. M. Kim, J.-M. Nam, and Y. D. Suh, "Nanogap-engineerable Raman-active nanodumbbells for single-molecule detection," *Nature Materials,* vol. 9, no. 1, pp. 60-67, 2010-01-01 2010, doi: 10.1038/nmat2596.

[107] S. Schlücker, "SERS Microscopy: Nanoparticle Probes and Biomedical Applications," *ChemPhysChem,* vol. 10, no. 9-10, pp. 1344-1354, 2009-07-13 2009, doi: 10.1002/cphc.200900119.

[108] Y. Wang, B. Yan, and L. Chen, "SERS Tags: Novel Optical Nanoprobes for Bioanalysis," *Chemical Reviews,* vol. 113, no. 3, pp. 1391-1428, 2013-03-13 2013, doi: 10.1021/cr300120g.

[109] L. Rodriguez-Lorenzo, L. Fabris, and R. A. Alvarez-Puebla, "Multiplex optical sensing with surface-enhanced Raman scattering: A critical review," *Analytica Chimica Acta,* vol. 745, pp. 10-23, 2012-10-01 2012, doi: 10.1016/j.aca.2012.08.003.

[110] N. Emmanuel, R. B. Nair, B. Abraham, and K. Yoosaf, "Fabricating a Low-Cost Raman Spectrometer to Introduce Students to Spectroscopy Basics and Applied Instrument Design," *Journal of Chemical Education,* vol. 98, no. 6, pp. 2109-2116, 2021-06-08 2021, doi: 10.1021/acs.jchemed.0c01028.

[111] D. Bury, C. Morais, K. Ashton, T. Dawson, and F. Martin, "Ex Vivo Raman Spectrochemical Analysis Using a Handheld Probe Demonstrates High Predictive Capability of Brain Tumour Status," *Biosensors,* vol. 9, no. 2, p. 49, 2019-03-30 2019, doi: 10.3390/bios9020049.

[112] Jonathan D Horsnell, Jenny A Smith, Martina Sattlecker, Alistair Sammon, Jonathan Christie-Brown, Catherine Kendall, and Nicholas Stone, "Raman spectroscopy—A new method for the intra-operative assessment of axillary lymph nodes," *The Analyst,* vol. 135, no. 12, p. 3042, 2010-01-01 2010, doi: 10.1039/c0an00527d.

[113] Abigail S Haka, Zoya Volynskaya, Joseph A Gardecki, Jon Nazemi, Robert Shenk, Nancy Wang, Ramachandra R Dasari, Maryann Fitzmaurice, and Michael S Feld, "Diagnosing breast cancer using Raman spectroscopy: prospective analysis," *Journal of Biomedical Optics,* vol. 14, no. 5, p. 054023, 2009-01-01 2009, doi: 10.1117/1.3247154.

[114] Abigail S. Haka, Zoya Volynskaya, Joseph A. Gardecki, Jon Nazemi, Joanne Lyons, David Hicks, Maryann Fitzmaurice, Ramachandra R. Dasari, Joseph P. Crowe, and Michael S. Feld, "In vivo Margin Assessment during Partial Mastectomy Breast Surgery Using Raman Spectroscopy," *Cancer Research,* vol. 66, no. 6, pp. 3317-3322, 2006-03-15 2006, doi: 10.1158/0008-5472.can-05-2815.

[115] Wen Chen, Shunping Zhang, Meng Kang, Weikang Liu, Zhenwei Ou, Yang Li, Yexin Zhang, Zhiqiang Guan, and Hongxing Xu, "Probing the limits of plasmonic enhancement using a two-dimensional atomic crystal probe," *Light: Science & Applications,* vol. 7, no. 1, 2018-12-01 2018, doi: 10.1038/s41377-018-0056-3.

[116] Y. Zeng, H. Qian, M. J. Rozin, Z. Liu, and A. R. Tao, "Enhanced Second Harmonic Generation in Double-Resonance Colloidal Metasurfaces," *Advanced Functional Materials,* vol. 30, no. 51, p. 2006826, 2020-12-01 2020, doi: 10.1002/adfm.202006826.

[117] J.-E. Park, Y. Lee, and J.-M. Nam, "Precisely Shaped, Uniformly Formed Gold Nanocubes with Ultrahigh Reproducibility in Single-Particle Scattering and Surface-Enhanced Raman Scattering," *Nano Letters,* vol. 18, no. 10, pp. 6475-6482, 2018-10-10 2018, doi: 10.1021/acs.nanolett.8b02973.

[118] J.-W. Oh, D.-K. Lim, G.-H. Kim, Y. D. Suh, and J.-M. Nam, "Thiolated DNA-Based Chemistry and Control in the Structure and Optical Properties of Plasmonic Nanoparticles with Ultrasmall Interior Nanogap," *Journal of the American Chemical Society,* vol. 136, no. 40, pp. 14052-14059, 2014-10-08 2014, doi: 10.1021/ja504270d.

[119] Daniela F. Cruz, Cassio M. Fontes, Daria Semeniak, Jiani Huang, Angus Hucknall, Ashutosh Chilkoti, and Maiken H. Mikkelsen, "Ultrabright Fluorescence Readout of an Inkjet-Printed Immunoassay Using Plasmonic Nanogap Cavities," *Nano Letters,* vol. 20, no. 6, pp. 4330-4336, 2020-06-10 2020, doi: 10.1021/acs.nanolett.0c01051.

[120] T. J. Dill, M. J. Rozin, S. Palani, and A. R. Tao, "Colloidal Nanoantennas for Hyperspectral Chemical Mapping," *ACS Nano,* vol. 10, no. 8, pp. 7523-7531, 2016-08-23 2016, doi: 10.1021/acsnano.6b02403.

[121] Y. Sun, "Shape-Controlled Synthesis of Gold and Silver Nanoparticles," *Science,* vol. 298, no. 5601, pp. 2176-2179, 2002-12-13 2002, doi: 10.1126/science.1077229.

[122] Y. Wang, K. Van Asdonk, and P. Zijlstra, "A Robust and General Approach to Quantitatively Conjugate Enzymes to Plasmonic Nanoparticles," *Langmuir,* vol. 35, no. 41, pp. 13356-13363, 2019-10-15 2019, doi: 10.1021/acs.langmuir.9b01879.

[123] M. V. Riquelme, H. Zhao, V. Srinivasaraghavan, A. Pruden, P. Vikesland, and M. Agah, "Optimizing blocking of nonspecific bacterial attachment to impedimetric biosensors," *Sensing and Bio-Sensing Research,* vol. 8, pp. 47-54, 2016-05-01 2016, doi: 10.1016/j.sbsr.2016.04.003.

[124] R. A. Alvarez-Puebla, D. S. Dos Santos Jr, and R. F. Aroca, "Surface-enhanced Raman scattering for ultrasensitive chemical analysis of 1 and 2-naphthalenethiols," *The Analyst,* vol. 129, no. 12, p. 1251, 2004-01-01 2004, doi: 10.1039/b410488a.

[125] N. R. Agarwal, A. Lucotti, M. Tommasini, F. Neri, S. Trusso, and P. M. Ossi, "SERS detection and DFT calculation of 2-naphthalene thiol adsorbed on Ag and Au probes," *Sensors and Actuators B: Chemical,* vol. 237, pp. 545-555, 2016-12-01 2016, doi: 10.1016/j.snb.2016.06.143.

[126] E. Massarini, P. Wästerby, L. Landström, C. Lejon, O. Beck, and P. O. Andersson, "Methodologies for assessment of limit of detection and limit of identification using surface-enhanced Raman spectroscopy," *Sensors and Actuators B: Chemical,* vol. 207, pp. 437-446, 2015-02-01 2015, doi: 10.1016/j.snb.2014.09.116.

[127] M. I. López, I. Ruisánchez, and M. P. Callao, "Figures of merit of a SERS method for Sudan I determination at traces levels," *Spectrochimica Acta Part A: Molecular and Biomolecular Spectroscopy,* vol. 111, pp. 237-241, 2013-07-01 2013, doi: 10.1016/j.saa.2013.04.031.

[128] Y. Xiao and S. N. Isaacs, "Enzyme-linked immunosorbent assay (ELISA) and blocking with bovine serum albumin (BSA)—not all BSAs are alike," *Journal of Immunological Methods,* vol. 384, no. 1-2, pp. 148-151, 2012-10-01 2012, doi: 10.1016/j.jim.2012.06.009.

[129] A. J. Haes and R. P. Van Duyne, "A Nanoscale Optical Biosensor: Sensitivity and Selectivity of an Approach Based on the Localized Surface Plasmon Resonance Spectroscopy of Triangular Silver Nanoparticles," *Journal of the American Chemical Society,* vol. 124, no. 35, pp. 10596-10604, 2002-09-01 2002, doi: 10.1021/ja020393x.

[130] Y. You, S. Lim, and S. Gunasekaran, "Streptavidin-Coated Au Nanoparticles Coupled with Biotinylated Antibody-Based Bifunctional Linkers as Plasmon-Enhanced Immunobiosensors," *ACS Applied Nano Materials,* vol. 3, no. 2, pp. 1900-1909, 2020-02-28 2020, doi: 10.1021/acsanm.9b02461.

[131] Monica Focsan, Andreea Campu, Ana-Maria Craciun, Monica Potara, Cosmin Leordean, Dana Maniu, Simion Astilean., "A simple and efficient design to improve the detection of biotin-streptavidin interaction with plasmonic nanobiosensors," *Biosensors & Bioelectronics,* vol. 86, pp. 728-735, Dec 2016, doi: 10.1016/j.bios.2016.07.054.

[132] Y. Cui and L. Ma, "Sequential use of milk and bovine serum albumin for streptavidin-probed western blot," *BioTechniques,* vol. 65, no. 3, pp. 125-126, 2018-09-01 2018, doi: 10.2144/btn-2018-0006.

[133] G. Wang, C. Yan, S. Gao, and Y. Liu, "Surface chemistry of gold nanoparticles determines interactions with bovine serum albumin," (in eng), *Mater Sci Eng C Mater Biol Appl,* vol. 103, p. 109856, Oct 2019, doi: 10.1016/j.msec.2019.109856.

[134] S. Sivasankar, S. Subramaniam, and D. Leckband, "Direct molecular level measurements of the electrostatic properties of a protein surface," *Proceedings of the National Academy of Sciences,* vol. 95, no. 22, pp. 12961-12966, 1998-10-27 1998, doi: 10.1073/pnas.95.22.12961.

[135] L. Almonte, E. Lopez-Elvira, and A. M. Baró, "Surface-Charge Differentiation of Streptavidin and Avidin by Atomic Force Microscopy-Force Spectroscopy," *ChemPhysChem,* vol. 15, no. 13, pp. 2768-2773, 2014-09-15 2014, doi: 10.1002/cphc.201402234.

[136] Bong Kuk Lee, Hea Yeon Lee, Pilnam Kim, Kahp Y. Suh, Jeong Hyun Seo, Hyung Joon Cha, and Tomoji Kawai, "Stepwise Self-Assembly of a Protein Nanoarray from a Nanoimprinted Poly(Ethylene Glycol) Hydrogel," *Small,* vol. 4, no. 3, pp. 342-348, 2008-03-03 2008, doi: 10.1002/smll.200700865.

[137] E. Rabani, D. R. Reichman, P. L. Geissler, and L. E. Brus, "Drying-mediated self-assembly of nanoparticles," (in eng), *Nature,* vol. 426, no. 6964, pp. 271-4, Nov 20 2003, doi: 10.1038/nature02087.

[138] N. Xia, J. S. Shumaker-Parry, M. H. Zareie, C. T. Campbell, and D. G. Castner, "A Streptavidin Linker Layer That Functions after Drying," *Langmuir,* vol. 20, no. 9, pp. 3710-3716, 2004-04-01 2004, doi: 10.1021/la035864n.

[139] L. M. Bonanno and L. A. Delouise, "Steric Crowding Effects on Target Detection in an Affinity Biosensor," *Langmuir,* vol. 23, no. 10, pp. 5817-5823, 2007-05-01 2007, doi: 10.1021/la063659c.

[140] A. M. Klose and B. L. Miller, "A Stable Biotin-Streptavidin Surface Enables Multiplex, Label-Free Protein Detection by Aptamer and Aptamer-Protein Arrays Using Arrayed Imaging Reflectometry," *Sensors,* vol. 20, no. 20, p. 5745, 2020-10-10 2020, doi: 10.3390/s20205745.

[141] Asia Sarycheva, Taron Makaryan, Kathleen Maleski, Elumalai Satheeshkumar, Armen Melikyan, Hayk Minassian, Masahiro Yoshimura, and Yury Gogotsi, "Two-Dimensional Titanium Carbide (MXene) as Surface-Enhanced Raman Scattering Substrate," *The Journal of Physical Chemistry C,* vol. 121, no. 36, pp. 19983-19988, 2017-09-14 2017, doi: 10.1021/acs.jpcc.7b08180.

[142] Y.-T. Li, L.-L. Qu, D.-W. Li, Q.-X. Song, F. Fathi, and Y.-T. Long, "Rapid and sensitive in-situ detection of polar antibiotics in water using a disposable Ag–graphene sensor based on electrophoretic preconcentration and surface-enhanced Raman spectroscopy," *Biosensors and Bioelectronics,* vol. 43, pp. 94-100, 2013-05-01 2013, doi: 10.1016/j.bios.2012.12.005.